nature nanotechnology

Double first for quantum dots

GRAPHENE
Three layers are different

RISK ANALYSIS
What can nanomedicine do?

NANOPARTICLE MIXTURES
Proteins show their potential

nature nanotechnology

EDITORIAL OFFICES

LONDON *www.nature.com/naturenanotechnology*
The Macmillan Building, 4 Crinan Street, London N1 9XW
T: +44 207 833 4000 F: +44 207 843 4563
Editor Peter Rodgers
Associate Editor Owain Vaughan
Copy Editor Melanie Hanvey
Production Editor Simon Gerrard
Art Editor Karen Moore
Editorial Assistant Hollie Cayzer

TOKYO *www.natureasia.com*
Chiyoda Building 2-37 Ichigayatamachi, Shinjuku-ku, Tokyo, 162-0843, Japan
T: +81 3 3267 8751 F: +81 3 3267 8746
Associate Editor Ai Lin Chun
Editorial Consultant Adarsh Sandhu

BOSTON
25 First Street, Suite 104, Cambridge, MA 02141, USA
T: +1 617 494 4900 F: +1 617 494 4960
Associate Editor Michael Segal

MANAGEMENT OFFICES

NPG LONDON *nature@nature.com*
The Macmillan Building, 4 Crinan Street, London N1 9XW
T: +44 207 833 4000 F: +44 207 843 4563
Managing Director Steven Inchcoombe
Publishing Director David Swinbanks
Publisher Jason Wilde
Associate Publisher Emma Green
Editor-in-Chief, Nature Publications Philip Campbell
Marketing Director Della Sar
Operations Director John Carroll
Director Of Web Publishing Timo Hannay
Associate Director, UK Production Jenny Henderson
Head Of Marketing, Physical Sciences Jane Macmillan
Marketing Manager, Physical Sciences Gurpreet Gill-Bains
Editorial Production Director James McQuat
Managing Production Editor Donald McDonald
Senior Production Editor Derna Simpson
Senior Copy Editor Jane Morris
Web Production Manager, UK Deborah Anthony
Production Director Yvonne Strong
Senior Production Controller Kelly Hopkins
Production Controller Emilia Orviss

NPG NEW YORK *nature@natureny.com*
75 Varick Street, 9th Floor, New York, NY 10013-1917
T: +1 212 726 9200 F: +1 212 696 9006
Chief Technology Officer Howard Ratner
Head Of Web Services Anthony Barrera
Executive Editor Linda Miller

NPG ASIA-PACIFIC *nature@natureasia.com*
Chiyoda Building 2-37 Ichigayatamachi, Shinjuku-Ku, Tokyo 162-0843 Japan
T: +81 3 3267 8751 F: +81 3 3267 8746
Associate Director Asia-Pacific Antoine E. Bocquet
Manager Koichi Nakamura
Operations Director Hiroshi Minemura
Asia-Pacific Sales Director Kate Yoneyama
Marketing Manager Masahiro Yamashita
Production Manager Takesh Murakami
Asia-Pacific Sales Manager Ken Mikami

NPG INDIA *npgindia@nature.com*
3a, 4th Floor, Dlf Corporate Park, GurGaon 122002, India
T: +91 12 4288 1054/55 F: +91 12 4288 1052
Head Of Business Development Debashish Brahmachari
Sales And Marketing Manager Harpal Singh Gill

DISPLAY ADVERTISING *physicalsciences@nature.com*
Global Head of Display Advertising Andrew Douglas T: +44 207 843 4975 F: +44 207 843 4996
Asia-Pacific Sales Director Kate Yoneyama T: +81 3 3267 8765 F: +81 3 3267 8746
Advertising Director George Lui T: +44 207 843 4966 F: +44 207 843 4749
Advertising Manager, Physical Sciences Simon Allardice T: +1 415 403 9034 F: +1 415 781 3805
Asia-Pacific Display Advertising Manager Ken Mikami T: +81 3 3267 8751 F: +81 3 3267 8746

NATUREJOBS *naturejobs@nature.com*

European Sales Manager Dan Churchward T: +44 207 843 4975 F: +44 207 843 4996
US Sales Manager Kenneth Finnegan T: +44 207 843 4975 F: +44 207 843 4996
Asia-Pacific Sales Manager Ayako Watanabe T: +81 3 3267 8765 F: +81 3 3267 8746

REPRINTS *reprint@nature.com*

For commercial reprint orders of 600 or more, please contact:
US/Canada: reprints@natureny.com **Northern Europe/UK/ROW:** reprints@nature.com
Southern Europe/Latin America: v.jurado@macmillanmedical.com
Asia-Pacific: m.kurosaki@natureasia.com **India:** d.brahmachari@nature.com

SITE LICENSE BUSINESS UNIT

Americas T: +1 888 331 6288 institutions@natureny.com
Asia/Pacific T: +81 3 3267 8751 institutions@natureasia.com
Australia/New Zealand T: +61 3 9825 1160 nature@macmillan.com.au
Europe/Row T: +44 207 843 4759 institutions@nature.com
India T: +91 124 2881054/55 npgindia@nature.com

CUSTOMER SERVICE

For all print and online assistance, please visit www.nature.com/help
Senior Global Customer Service Manager Gerald Coppin

ORIGINAL RESEARCH TYPESET BY Techset Composition Ltd, www.techset.co.uk
PRINTED BY Wyndeham Grange, www.wyndeham.co.uk

JUNE 2009 VOL 4 ISSUE 6

nature nanotechnology

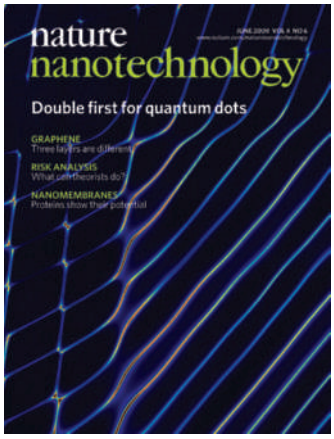

COVER IMAGE

Quantum dots defined in carbon nanotubes are attractive for exploring a wide range of phenomena in fundamental physics. For some of these experiments it is necessary to confine a single electron in a quantum dot, while controlling the height of the barriers on either side of the dot, but this has proved difficult. Now, Gary Steele, Georg Gotz and Leo Kouwenhoven have confined a single electron in a tunable double quantum dot in a nanotube for the first time, and also observed a novel type of tunnelling that is analogous to relativistic Klein tunnelling. This false-colour plot shows electric current as a function of the voltages applied to two of the gates in the system.

Letter p363; News & Views p347

ON THE COVER

Graphene
Three layers are different
Letter p383

Risk analysis
What can theorists do?
Commentary p332

Nanomembranes
Proteins show their potential
Letter p353; News & Views p345

EDITORIAL

COMMENTARY

THESIS

BOOKS & ARTS

RESEARCH HIGHLIGHTS

NEWS & VIEWS

LETTERS

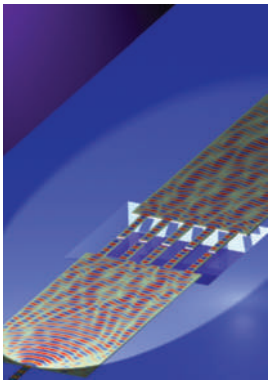

An all-optical chip-based method has been used to actuate and detect the motion of silicon nanocantilevers.
Letter p377;
News & Views p344

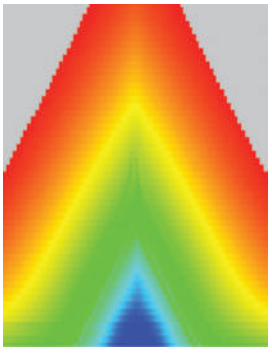

Assemblies of nanoparticles have been used to explore electron transport in the one-dimensional limit.
Letter p368

CLASSIFIEDS

See the back pages

nature publishing group

Nature Nanotechnology (ISSN 1748-3387) is published monthly by Nature Publishing Group (Porters South, 4 Crinan Street, London N1 9XW, UK). Editorial Office: Porters South, 4 Crinan Street, London N1 9XW, UK. Telephone: +44 (0)20 7833 4000. Fax: +44 (0)20 7843 4563. Email: naturenano@nature.com. North American Advertising: *Nature Nanotechnology*, 75 Varick Street, Fl 9, New York, NY, 10013-1917, US. Telephone: +1(212) 726-9200. Fax: +1(212) 696-9006. European Advertising: *Nature Nanotechnology*, Porters South, 4 Crinan Street, London N1 9XW, UK. Telephone: +44 (0)20 7833 4000. Fax: +44 (0)20 7843 4749. New subscriptions/renewals/changes of address/back issues and all other customer service questions should be addressed to - North America: *Nature Nanotechnology*, Subscription Dept, PO Box 5054, Brentwood, TN 37024-5054, USA. Outside North America: Subscriptions Department, Brunel Road, Basingstoke, Hants. RG21 6XS, UK. Telephone: +44 (0)1256 329242; Fax: +44 (0)1256 812358. Annual subscription rates: US/Canada US$3060, Canada add 5% GST (institutional/corporate), US$152, Canada add 5% GST (individual making personal payment); US$88, Canada add 5% GST (individual making Research Highlights newsletter payment); UK/Rest of World (excluding Europe and Japan) £1570 (institutional/corporate), £78 (individual making personal payment), £45 (individual making Research Highlights newsletter payment); Europe €2430 (institutional/corporate), €121 (individual making personal payment), €70 (individual making Research Highlights newsletter payment). Japan: contact Nature Asia-Pacific, Chiyoda Building, 2-37 Ichigayatamachi, Shinjuku-Ku, Tokyo, 162-0843, Japan. Telephone +81 3 3267 8751. Back issues: US/Canada $45 (Canada add 5% GST); Rest of World: surface US$43, air mail US$45. *Nature Nanotechnology* (ISSN 1748-3387) is published monthly by Nature Publishing Group, c/o Mercury Airfreight International Ltd, 365 Blair Road, Avenel, NJ 07001, USA. Periodicals postage is paid at Rahway NJ. Postmaster: send address changes to *Nature Nanotechnology*, c/o Mercury Airfreight International, 365 Blair Road, Avenel, NJ, USA. Reprints: *Nature Nanotechnology* Reprints Department, Porters South, 4 Crinan Street, London N1 9XW, UK. Subscription information is available at the *Nature Nanotechnology* homepage at http://www.nature.com/naturenanotechnology. Postmaster: send address changes to *Nature Nanotechnology* Subscriptions Department, Brunel Road, Basingstoke, Hants. RG21 6XS, UK or *Nature Nanotechnology* Subscriptions Department PO Box 5054, Brentwood, TN 37024-5054, USA.

The responsibilities of authors

Changes to our policies on authorship reflect the need for greater clarity about the contributions made by different authors to research papers.

The laws of physics, as far as we know, do not change with time, which makes them unique in many ways because most laws — legal, sporting or otherwise — are regularly revised or replaced, with new laws being introduced to reflect changes in public attitudes, developments in technology, new threats to society and countless other things. The same is true of science and scientific publishing, and there have recently been some changes in the laws — or policies as we like to call them — at Nature Publishing Group[1,2]. There are two main changes: the duties of senior authors within collaborations have been made explicit, and author-contribution statements will be mandatory for papers submitted after 30 April 2009. At the same time, *Nature Nanotechnology* is discontinuing the practice of accepting presubmission enquires about manuscripts.

Is getting the grant for the research enough for someone to be listed as an author?

As an increasing volume of research is carried out by collaborations, often from labs based in different countries or continents, it has become more important to be clear about who did what and who is responsible for different parts of the paper. Therefore, for papers from such collaborations, we are now asking that at least one senior member from each group in the collaboration takes responsibility for that group's contribution to the manuscript. At a minimum, this author should agree to: ensure that the original data is preserved and retrievable for re-analysis; ensure that the data reported in the paper are representative of the original data; and foresee and minimize obstacles to the sharing of data, materials, algorithms or reagents described in the paper. The corresponding author(s) will remain responsible for ensuring that enquiries about the paper are answered promptly on behalf of the coauthors, directing enquiries to the other authors as appropriate.

Related to this is the decision to make author-contribution statements compulsory. Many papers in *Nature Nanotechnology* already contain such statements[3], but a significant minority do not, and there seems to be no compelling arguments for papers not to include them. There is no prescribed format for these statements — it is equally acceptable to state that: "All authors contributed to all aspects of this work," or to detail who, for example, prepared the samples, did the characterization, performed the measurements, analysed the data, did the theory, wrote the manuscript, commented on it, directed the project and so forth. The only requirement is that each author is included in this statement — and if it seems difficult to summarize what someone did, maybe they should be mentioned in the acknowledgements instead.

This will inevitably raise the question — is getting the grant for the research enough for someone to be listed as an author? The answer to this question will vary from paper to paper; however, as 'getting the grant' generally also involves, among other things, writing a detailed proposal, recruiting new researchers to the project and providing ongoing intellectual input and internal review/quality control/supervision, the answer will often be yes.

While discussing the issue of author responsibility it is impossible not to think about famous cases of misconduct in science and to ask what, if any, changes in the policies of journals might have prevented them. Would either of the changes outlined above have prevented Jan Hendrik Schön from publishing a string of papers containing fabricated data between 2000 and 2002? Probably not, but they might have clarified some of the unusual circumstances surrounding his work — such as the fact that many of his experiments were 'performed' at Konstanz University, where he did his PhD, and not at Bell Labs, where he was employed — and might have made some of his colleagues more reluctant to be listed as coauthors on his papers. (A new book on the Schön affair, *Plastic Fantastic*, is reviewed on page 337 of this issue).

The official report[4] into the Schön affair also raised the issue of the responsibilities of coauthors, but it effectively ducked this "extremely difficult issue" because "no clear, widely accepted standards of behaviour exist". For the record, the report concluded that Schön's coauthors had, "in the main, met their responsibilities, but that in one case questions remain that the Committee felt unqualified to resolve, given the absence of a broader consensus on the nature of the responsibilities of participants in collaborative research endeavours."

The peer review process is not black and white, and differences of opinion are routine.

The new guidelines outlined above, and those introduced by other publishers, are intended to address some of these issues. It is now generally agreed that every author is not responsible for every aspect of the paper, and that some authors need to be more responsible than others. The American Physical Society[5] for instance, goes further than Nature Publishing Group by stating: "Authorship should be limited to those who have made a significant contribution to the concept, design, execution or interpretation of the research study … Some co-authors have responsibility for the entire paper as an accurate, verifiable, report of the research. These include, for example, coauthors who are accountable for the integrity of the critical data reported in the paper, carry out the analysis, write the manuscript, present major findings at conferences, or provide scientific leadership for junior colleagues."

Of course, the peer review process is not black and white, and differences of opinion between authors, referees and editors are routine, but it is in all our interests to adhere to the laws as they stand at present, and to improve them as and when we can. ❐

References

1. http://www.nature.com/authors/gta.pdf
2. *Nature* **458,** 1078 (2009).
3. *Nature Nanotech.* **3,** 179 (2008).
4. http://publish.aps.org/reports/lucentrep.pdf
5. http://www.aps.org/policy/statements/02_2.cfm

How can *ab initio* simulations address risks in nanotech?

Amanda S. Barnard

Discussions of the potential risks and hazards associated with nanomaterials and nanoparticles tend to focus on the need for further experiments. However, theoretical and computational nanoscientists could also contribute by making their calculations more relevant to research into this area.

Significant numbers of consumer products based on nanotechnology are entering the market, and large quantities of nanoparticles are now being produced annually. In producing these products, we are confronted with the vexatious reality that the very same physical features that provide the sensitivity and reactivity that are essential for many of these applications may also be a disadvantage when we consider the possible risks and hazards associated with these products[1,2]. Therefore, in parallel with the development of new nanotechnologies, the toxicology of nanomaterials is also under scrutiny[3–5], as is their impact on the environment[6–8] and issues related to workplace safety[9]. This article highlights areas in which *ab initio* computer simulations can help develop our understanding of these hazards, and suggests ways in which existing techniques can be made more applicable to this field of research.

At present, attention is focused on the interaction of nanomaterials with living organisms[10]. It has already been shown that some nanomaterials have the potential to damage skin, brain and lung tissue, and accumulate in the body[10], though consensus on some areas is still lacking. Reports on the toxicity of carbon nanotubes, for example, are delivering both good and bad news. An *in vitro* study measuring the impact of single-walled carbon nanotubes on mitochondria in human A549 lung cells found what appeared to be signs of cytotoxicity in approximately 50% of the cells when MTT (a salt that is not soluble in water) was used, but there were no signs of cytotoxicity when WST-1 (a salt that is soluble in water), was used. Moreover, no cytotoxicity was observed when the salt INT, the dye TMRE or the antibody Annexin-V was used[11]. (All these salts, dyes and antibodies are routinely used in cell viability and proliferation assays). However, exposure of the mesothelial lining of the body cavity in mice to long multiwalled carbon nanotubes has recently been shown to result in asbestos-like, length-dependent, pathogenic behaviour[12]. It has been found that the functionalization of carbon nanotubes can reduce toxicity[13], but stable chemisorption on nanotubes is intrinsically linked to the environmental factors such as pressure and temperature[14].

Numerous reports are available that summarize current knowledge and highlight areas requiring more focused attention[15–21], but most of the strategies suggested in these reports are based on inherently experimental approaches to the problem. Not surprisingly, discussions about risks can seem esoteric to theoretical and computational nanoscientists, and somewhat removed from their sphere of influence. However, we are still under scrutiny from our governments, companies, institutions, other nanoscientists, the wider scientific community and society as a whole, and the issue of the potential risks associated with nanotechnology cannot be avoided. So we are confronted with the

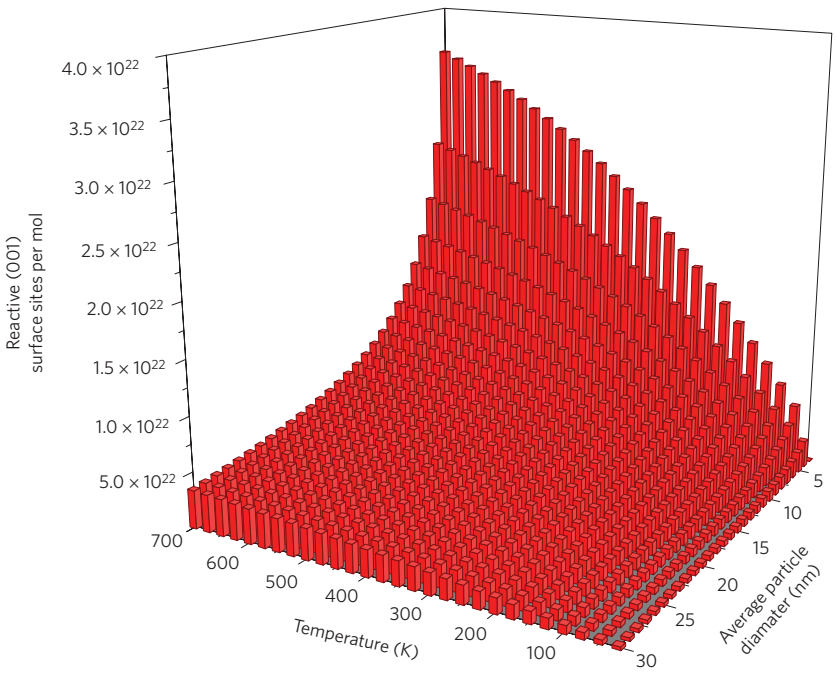

Figure 1 | Density functional theory can be used to predict the fraction of (001) surface facets on polyhedral anatase (a form of titania) nanoparticles as a function of temperature and nanoparticle size. Complementary DFT calculations can also predict the reactivity of these (001) surfaces making it possible to calculate the number of potentially reactive sites per mole of anatase in water[26].

inevitable question — what can *ab initio* modellers do to help?

The right tool for the job

Clearly we should start by focusing on the critical areas requiring the most immediate attention. We already know from experiments that the undesirable properties of nanomaterials depend on, and are moderated by, a wide range of physical parameters[15–20] such as size, shape, chemical composition or degree of agglomeration. We also know that many of these dependencies are intrinsically linked[2], and we must take this knowledge into account before we make predictions about possible risks.

Fortunately this is an area where computational nanoscientists have an advantage because, unlike our experimental colleagues, we can control each of these critical parameters independently, and identify underlying mechanisms responsible for instabilities. It is also possible to investigate nanostructures in highly non-equilibrium environments — such as extreme temperatures and pressures, or strong electric or magnetic fields — that cannot be probed experimentally. Using a systematic approach and accurate *ab initio* simulations it is possible to rapidly sample parameter space, and build much needed predictive capabilities with a high degree of confidence.

Recent examples of such work include the characterization of the surface reactivity of ferrihydrite nanoparticles assembled in ferritin (an iron storage protein) using molecular orbital/density functional theory (MO/DFT) calculations[22]; the characterization of the surface reactivity of gold nanoparticles using extended Hückel theory combined with DFT calculations[23]; and a DFT study of the nanotoxicological implications of oxygen adsorption at silver surfaces (including *ab initio* molecular dynamics)[24]. Among the computational methods used in materials physics, DFT (a quantum mechanical theory principally used to investigate the electronic structure) offers the greatest sensitivity to chemical reactions and is an extremely powerful method for calculating the ground-state properties of metals, semiconductors and insulators.

Another pertinent example is titanium dioxide. This mineral, also known as titania, occurs in three forms: rutile, anatase and brookite. Concern has focused on nanoparticles of the anatase form because photocatalytic activity on the surface of these nanoparticles can produce reactive oxygen species[1], which can be damaging to health. The (001) surface of the anatase form has been shown to be particularly reactive[25], though the relative fraction of this surface that is found in samples depends on the temperature and chemical environment[26]. However, DFT can be used to predict the number of reactive sites on the surface of polyhedral particles, as a function of temperature and nanoparticle size (Fig. 1).

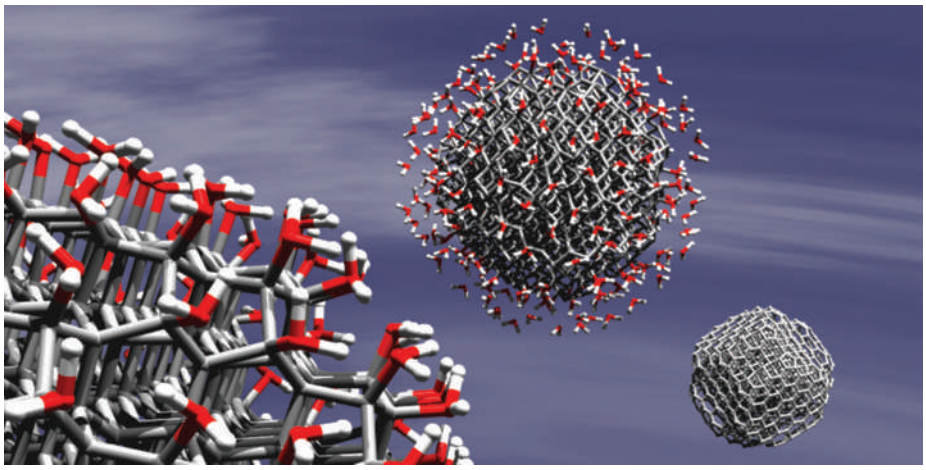

Figure 2 | Real nanoparticles interact with the gases, liquids and other nanoparticles surrounding them. These chemical and physical interactions can be included computer simulations to give insights into the structure and stability of nanoparticles in natural environments.

Although theory and simulation have a lot to offer, especially in the area of bio–nano interactions[1] — such as the recent computer simulations showing fullerene translocation through lipid membranes[27] — very few of us are funded to study these issues. However, when conducting the research that we are funded to do, there are a few computational and theoretical accommodations we can make that will allow our existing work to be more useful to those who are focused on nanohazards, as the following three examples illustrate.

The problem with zero temperature

To put it rather bluntly, the problem with zero temperature is that nothing actually takes place. Certainly the highly accurate *ab initio* calculations that can only be performed at zero temperature have allowed us to calculate details of electronic structure that could not be calculated any other way. Moreover, the information gained from such simulations about the structure of nanomaterials has improved our understanding of morphological stability and reactivity. However, it is clear that a nanoparticle inside our bodies, in contact with our skin or released into an ecosystem will not be at zero temperature.

One way that temperature effects may be included in *ab initio* simulations is to include the entropic contribution to the Gibbs free energy, as opposed to simply using the potential energy, as described by the second law of thermodynamics. There are various robust methods for calculating the free energies, beginning with traditional methodologies based on harmonic approximations, thermodynamic integration and lambda integration methods, complemented by more specialized approaches (see ref. 28 for a review).

Finite temperatures may also be included in computational studies by using *ab initio* versions of well-known classical methods such as molecular dynamics (for example, *ab initio* molecular dynamics or Car–Parrinello molecular dynamics) or Monte Carlo simulations to obtain the equilibrium geometry (at temperatures greater than zero), rather than optimization methods such as conjugate gradient or steepest decent approaches (which are temperature independent). A significant proportion of computational studies are performed to determine the low-energy (equilibrium) geometry of the system under consideration, and use this equilibrium geometry to model representative physical properties or interactions with other systems. If these geometries are obtained using molecular dynamics or Monte Carlo simulations at finite temperature, the results will be more relevant to real nanomaterials under realistic conditions.

Treating the full range of temperatures that may be experienced by nanomaterials throughout their life-cycle may be unrealistic for some of us, but in the first instance, it will certainly help if we adopt

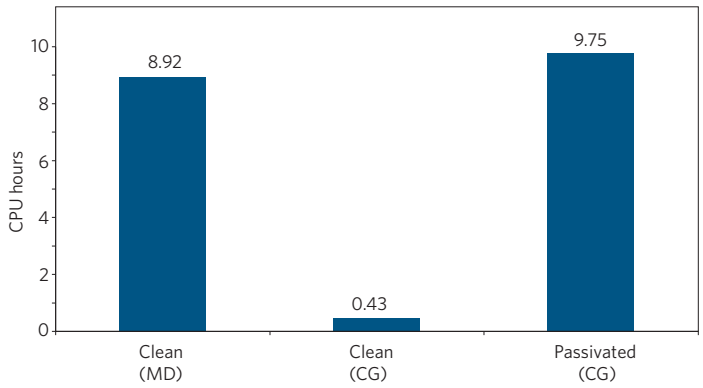

Figure 3 | Number of CPU hours needed to simulate a periodic 64 atom [100] oriented slab of platinum using three approaches: molecular dynamics (MD) at 300 K, conjugate gradient methods (CG), and a fully hydrogen passivated version of the same slab using CG. Although using a finite temperature or passivation increases the CPU time by a factor of about 20, the results are more relevant to the real world. CPU hours were calculated with VASP using DFT-PBE and PAW pseudopotentials on the Australian National Computational Infrastructure SGI Altix 3700 Bx2 cluster with 1928 1.6 GHz Itanium2 processors. The MD approach was equilibrated after 140 fs, based on analysis of thermodynamic properties and root-mean-square deviation of atomic positions.

room temperature (rather than zero temperature) as a new standard.

Simulating the right environment

This brings us to the relationship between the stability of nanomaterials and their chemical environment. Although a large number of nanostructures are produced under ultrahigh-vacuum conditions, very few of them are stored or intended for extended use under these conditions, and most will eventually be exposed to air and/or water (at least). This may seem unimportant but we are starting to appreciate that, just as nanoparticles can affect the environment, environmental changes (such as exposure to air or water) can also have an effect on nanomaterials. It has been shown, for example, that 3-nm zinc sulphide nanoparticles synthesized in methanol show a reversible structural transformation associated with methanol desorption, and subsequent binding of water to the nanoparticle surface, at room temperature[29].

As nanomaterials have a high surface area, maintaining stable surfaces both in devices and in storage media is of critical importance, and computer simulations are ideal for exploring the structure of surfaces and identifying even the smallest change in the position of atoms near edges, corners, surface steps and defects. Most reports in the literature involve conveniently 'clean' surfaces that are experimentally unrealistic (other than in ultrahigh-vacuum conditions). To make our calculations realistic we therefore need to passivate the surfaces of the nanostructures we are simulating by, for example, adding monolayers of small molecules. Depending on the chemical environment in question, this could mean chemisorption or physisorption (Fig. 2). Irrespective of the specific interaction, there is a considerable (and reliable) body of literature examining the adsorption of molecules on surfaces to guide the placement and configuration of these adsorbates, and more advanced solvation methodologies integrated into some software packages. Hence, it is suggested that our new default standard should be to passivate our structures with the most ubiquitous environmental components: water or the main reactive constituents of air.

Isolation and agglomeration

As mentioned above, common concerns raised in various reports[15–20] distinguish between isolated nanomaterials and those already integrated into products and devices. Individual nanoparticles are a source of concern, as studies have shown that they are capable of passing through cell membranes, moving through the body by means of the circulatory system, and potentially passing through the blood–brain barrier[21]. This forms the basis of many biomedical applications such as drug delivery and medical imaging, and illustrates that a detailed understanding of the properties of individual nanoparticles is imperative.

This is another area that can be tackled by *ab initio* simulation with relative ease, as we are used to looking at single, isolated nanostructures. However, in real specimens, nanoparticles tend to agglomerate and form larger superstructures that are easily perturbed by environmental factors such as changes in temperature, pressure and pH. Therefore, in addition to understanding the properties of individual nanoparticles, there is also a need to understand the interactions between nanoparticles. The precise nature of interparticle interactions, the structure of the interface, and the packing of arrays and superstructures can be difficult to probe experimentally, and again this represents another an opportunity for computational nanoscientists.

As one would expect, the best strategy is to include more than one nanoparticle in our simulations[30]. However, simulations with many nanoparticles can make individual calculations too computationally intensive and impractical for DFT. There is a simple way that we can address this issue without devoting additional resources or conducting supplementary simulations that are beyond the scope of our investigations. When examining the structure of free surfaces it is often customary to use a three-dimensional periodic supercell containing a two-dimensional 'slab' of material to represent a facet; it is also common to use three-dimensional supercells in simulations of one-dimensional structures. When performing these simulations we take great care to ensure that the structures are isolated from their mirror images by adding sufficient vacuum space to obtain convergence of, for example, binding energies, dipole interactions and charge distributions. But as we search for the ideal separation distance (to balance the computational load and the accuracy of the results) we are also gathering valuable information about the interactions between the surfaces of the structure and its surroundings. A more detailed analysis of this (existing) data could assist in understanding what drives agglomeration and self-assembly, and is worthy of inclusion in our publications.

Conclusions

So, can *ab initio* simulations help address potential hazards and risks in nanoscience and nanotechnology? The answer is a resounding yes. As our models become more sophisticated, and computational resources more accessible, we are well placed to engage these new challenges[28,31,32]. Although we are often more focused on other aspects of nanoscience and nanotechnology, we are studying the right materials and we have developed the right methods. There are, however, few ways that we can make our calculations more accessible to those

working specifically on nanohazards, as outlined here. I am not advocating that we place these accommodations ahead of our mandated research — only that we should consider them when it does not conflict with our existing objectives (Fig. 3), and of course, I include myself in this vision.

Sometimes, computer simulation is the right tool for the job, as shown by the increase in support for computational studies examining the interaction of nanoparticles with biological systems. Given the more specific, quantitative knowledge gained from theory and simulation we can build predictive models that will facilitate the design of more appropriate storage systems, protect nanomaterials from the environment as much as they protect the environment (and us) from them, and allow us to construct algorithms for assessing the likelihood of toxicity in a variety of natural environments. ❐

Amanda S. Barnard is in the Department of Materials Science & Engineering, CSIRO, Clayton, Victoria 3169, Australia.
e-mail: amanda.barnard@csiro.au

References

1. Nel, A., Xia, T., Mädler, L. & Li, N. *Science* **311,** 622–627 (2006).
2. Barnard, A. S. *Nature Mater.* **5,** 245–248 (2006).
3. Dumortier, H. *et al. Nano Lett.* **6,** 1522–1528 (2006).
4. Magrez, A. *et al. Nano Lett.* **6,** 1121–1125 (2006).
5. Pulskamp, K., Diabaté, S. & Krug, H. F. *Toxicol. Lett.* **168,** 58–74 (2007).
6. Donaldson, K., Stone, V., Tran, C. L., Kreyling, W. & Borm, P. J. A. *Occup. Environ. Med.* **61,** 727–728 (2004).
7. Lam, C. W., James, J. T., McCluskey, R., Arepalli, S. & Hunter, R. L. *Crit. Rev. Toxicol.* **36,** 189–217 (2006).
8. Hyung, H., Fortner, J. D., Hughes, J. B. & Kim, J.-H. *Environ. Sci. Technol.* **41,** 179–184 (2007).
9. Donaldson, K. *et al. Toxicol. Sci.* **92,** 5–22 (2006).
10. Hoet, P. H. M., Brüske-Hohlfeld, I. & Salata, O. V. *J. Nanobiotech.* **2,** 12 (2004).
11. Wörle-Knirsch, J. M., Pulskamp, K. & Krug, H. F. *Nano Lett.* **6,** 1261–1268 (2006).
12. Poland, C. A. *et al. Nature Nanotech.* **3,** 423–428 (2008).
13. Sayes, C. M. *et al. Toxicol. Lett.* **161,** 135–142 (2006).
14. Durgun, E. *et al. Phys. Rev. B* **67,** 201401 (2003).
15. National Science Foundation *Societal Implicatons of Nanoscience and Nanotechnology* (US Government, 2001); available at <http://tinyurl.com/qmf2fw>.
16. *Nanotechnologies: A Preliminary Risk Analysis* (European Commission, 2004); available at <http://tinyurl.com/p3pw6l>.
17. *Nanoscience and Nanotechnologies: Opportunities and Uncertainties* (The Royal Society, 2004); available at <http://www.nanotec.org.uk/finalReport.htm>.
18. *EuroNanoForum 2005: Nanotechnology and the Health of the Human Citizen in 2020* (European Commission, 2005); available at <http://tinyurl.com/oxoyp6>.
19. National Nanotechnology Strategy Taskforce *Options for a National Nanotechnology Strategy* (Australian Government, 2006); available at <http://tinyurl.com/re3leh >.
20. National Nanotechnology Innitiative *Environmental, Health, and Safety Research Needs for Engineered Nanoscale Materials* (US Government, 2006); available at <http://tinyurl.com/oqownf>.
21. Hunt, G. & Mehta, M. D. (eds) *Nanotechnology: Risks, Ethics and the Law* (Earthscan, 2006).
22. Liu, G. *et al. Langmuir* **22,** 9313–9321 (2006).
23. Phala, N. S. & Van Steen, E. *Gold Bull.* **40,** 150–153 (2007).
24. Akdim, B., Hussain S. & Pachter, R. in *Computational Science — ICCS 2008 Part II* (eds Bubak, M., van Albada, G. D., Dongarra, J. & Sloot, P. M. A.) 353–359 (Springer, 2008).
25. Vittadini, A., Casarin, M. & Selloni, A. *Theor. Chem. Acc.* **117,** 663–671 (2007).
26. Barnard, A. S. & Xu, H. *ACS Nano* **2,** 2237–2242 (2008).
27. Wong-Ekkabut, J. *et al. Nature Nanotech.* **3,** 363–368 (2008).
28. Rickman, J. M. & LeSar, R. *Annu. Rev. Mater. Res.* **32,** 195–217 (2002).
29. Zhang, H., Gilbert, B., Huang, F. & Banfield, J. F. *Nature* **424,** 1025–1029 (2003).
30. Barnard, A. S. *J. Mater. Chem.* **18,** 813–815 (2008).
31. Rieth, M. & Schommers, W. (eds) *Handbook of Theoretical and Computational Nanotechnology* (American Scientific, 2006).
32. Lakhtakia, A. *Handbook of Nanotechnology: Nanometer Structure Theory, Modeling, and Simulation* (American Society of Mechanical Engineers, 2004).

Acknowledgements

I acknowledge support from L'Oréal Australia and UNESCO, and thank George Smith for useful discussions.

Are you a responsible nanoscientist?

Various codes of conduct have been proposed for nanotechnology — **Richard Jones** examines what they mean for individual researchers.

What does it mean to be a responsible nanoscientist? Last year the European Commission published a recommendation on "a code of conduct for responsible nanosciences and nanotechnologies research"[1]. Unlike other codes, such as the Responsible NanoCode[2], which are focused more on business and commerce, the European Commission code is aimed at the academic research enterprise. It raises interesting questions about the degree to which individual scientists are answerable for consequences of their research, even if those consequences were ones that they did not, and possibly could not, foresee.

The general goals of the EC code are commendable — it aims to encourage dialogue between everybody involved in and affected by the research enterprise, from researchers in universities and industry, through to policy makers, non-government organizations and the general public, and it seeks to make sure that nanotechnology research leads to sustainable economic and social benefits. There are, though, questions about who is responsible for achieving this desirable state.

Some scientists, for example, might be alarmed at the statement in the code that "researchers and research organisations should remain accountable for the social, environmental and human health impacts that their N&N [nanosciences and nanotechnologies] research may impose on present and future generations." Many scientists believe in a division of moral labour – they do the basic research that, in the absence of direct application, remains free of moral implications; technologists and industrialists then take responsibility for the consequences of applying that science, whether those are positive or negative.

This division of responsibility has perhaps begun to blur, as the distinction between pure and applied science becomes harder to make. Some scientists are happy to embrace this because, after all, they are happy to take credit for the positive impact of past scientific advances, and to cite the potential big impacts that might hypothetically flow from their results.

But is the concept of accountability fair or meaningful when applied to the downstream implications of scientific research, when those implications are likely to be very difficult to predict at an early stage? The scientists who make an original discovery may have little influence in the way it is commercialized. If there are adverse environmental or health impacts of some discovery in nanoscience, the primary responsibility must surely lie with those directly responsible for creating conditions in which people or ecosystems were exposed to the hazard, rather than the original discoverers. Perhaps it would be more helpful to think about the responsibilities of researchers in terms of a moral obligation to be reflective about possible consequences, to consider different viewpoints, and to warn about possible concerns.

> Many would strongly disagree with the principle that what is legal is necessarily ethical.

A consideration of the potential consequences of one's own research is one possible ethical starting point. The uncertainty that necessarily surrounds any predictions about the way research may end up being applied in the future, and the lack of agency and influence on those applications that researchers often feel, can limit the usefulness of this approach. The Government Office for Science in the UK takes a different view in the 'Universal Ethical Code for Scientists'[3]. This code is based on one general principle — "ensure that your work is lawful and justified" — and one injunction to "minimise and justify any adverse effect your work may have on people, animals and the natural environment".

A reference to what is lawful has the benefit of clarity, and it provides some connection through the traditional mechanisms of democratic accountability with the will of society at large. But the law is always likely to be slow to catch up with the new possibilities suggested by new technology, and many would strongly disagree with the principle that what is legal is necessarily ethical. As far as the test of what is "justified" is concerned, one has to ask, who is to judge this?

One controversial research area that probably would pass the test of "lawful and justified" research is the application of nanotechnology to defence. However, developing a new nanotechnology-based weapons system would contravene the EC code, which states that researchers "should not harm or create a biological, physical or moral threat to people". Researchers working in a government research organization with this aim might reassure themselves with the thought that it was the job of the normal processes of democratic oversight to ensure that their work did pass the tests of lawfulness and justifiability. But this won't satisfy those people who are sceptical about the ability of institutions — public or private — to manage the inevitably uncertain consequences of new technology.

The question we return to, then, is how is responsibility divided between the individuals who do science, and the organizations, institutions and social structures in which science is done? There's a danger that codes of ethics focus too much on the individual scientist, at a time when many scientists often feel rather powerless, with research priorities increasingly being set from outside and with the development and application of their research out of their hands. In this environment, too much emphasis on individual accountability could prove alienating, and could divert us from efforts to make the institutions in which science and technology are developed more responsible.

Scientists, however, should not completely underestimate their importance and influence collectively, even if individually they feel impotent. Part of the responsibility of a scientist should be to reflect on how to justify one's work, and how people with different points of view might react to it, and such scientists will be in a good position to have a positive influence on the various institutions they interact with, such as funding agencies. But we still need to think more generally about how to make responsible institutions for developing science and technology, as well as responsible nanoscientists. ❐

Richard Jones is in the Department of Physics and Astronomy at the University of Sheffield, UK.
e-mail: r.a.l.jones@sheffield.ac.uk

References

1. ftp://ftp.cordis.europa.eu/pub/fp7/docs/nanocode-recommendation.pdf
2. http://www.responsiblenanocode.org/
3. http://www.berr.gov.uk/files/file41318.pdf

Notes on a scientific scandal

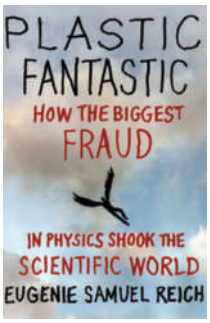

Plastic Fantastic: How the Biggest Fraud in Physics Shook the Scientific World

by Eugenie Samuel Reich

PALGRAVE MACMILLAN: 2009. 272 PP. £15.00; $26.95 HARDBACK

Sometime in 1999, when I was editor of *Physics World* magazine, I commissioned Bertram Batlogg, then based at the world-famous Bell Laboratories in Murray Hill, New Jersey, to write an article on cuprate superconductors. As I recall, a first draft arrived a few months later, and I replied with some queries and suggestions. I also recall that it took much longer than usual for the second draft to be delivered, but it must have arrived towards the end of 1999 because the article was published in the February 2000 issue of the magazine.

Flicking through the 13 January 2000 issue of *Nature*, as Batlogg's article would have been going to press, I saw a news story that seemed to explain the delay: patent judges had decided that Batlogg and co-workers at Bell Labs should be granted US patent rights for a widely used high-temperature superconductor discovered over a decade earlier. However, other possible explanations for the delay started to arrive thick and fast in high-profile journals: two weeks later *Nature* contained a paper by Batlogg and three others — Jan Hendrik Schön, Christian Kloc and Ernst Bucher — on organic photovoltaic diodes, quickly followed by a paper on organic field-effect transistors (by Schön, Steffen Berg, Kloc and Batlogg) in *Science*.

In 2000 alone, the Schön–Kloc–Batlogg juggernaut published a total of eight papers in *Nature* and *Science* on various devices made from organic crystals, on superconducting devices based on carbon-60 molecules, and on fundamental physics such as the fractional quantum Hall effect. I was tempted to ask Batlogg and his co-workers to write another feature article on all this work but decided they would be too busy. Instead I asked a freelance to write a news story about this explosion of creativity and productivity. This article focused mostly on Batlogg (then one of the five most-cited physicists in the world), who said that Kloc grew crystals of the "highest quality" and that Schön (a relatively unknown researcher at the time) had "an excellent background in semiconductor physics and photovoltaics" (*Physics World* **14,** 9; January 2001).

Batlogg moved to ETH Zurich in Switzerland around this time but Schön continued to pump out the papers with a variety of new co-workers until, in May 2002, the wheels came off. Bell Labs announced that it had set up a committee chaired by Malcolm Beasley of Stanford University to investigate if scientific misconduct had occurred. The committee's report, released on 25 September 2002, found Schön guilty on 16 out of 24 charges of misconduct, and he was fired on the same day. His offences included "manipulation and misrepresentation of data", notably "the substitutions of single curves or even parts of single curves, in multiple figures representing different materials or devices, and the use of mathematical functions to represent real data". It also emerged that "none of the most significant physical results was witnessed by any coauthor or other colleague", sometimes because they had been performed (if that is the right word) by Schön back in Konstanz, rather than at Bell Labs.

All of Schön's coauthors — including Batlogg and Kloc — were cleared of misconduct, and were also found to "have, in the main, met their responsibilities [as coauthors]". However, the committee mostly skirted around the issue of author responsibility, apart from rhetorically asking if Batlogg "took a sufficiently critical stance with regard to the research in question" — to which he replied, in an appendix to the report, that he had (see page 331 for more on author responsibility). Seven papers in *Nature* and eight in *Science* were later retracted.

The Beasley committee's report is one of the most remarkable documents I have ever read, and I am pleased to report that this book by the science journalist Eugenie Samuel Reich does a magnificent job of going behind the necessarily measured language of the official report and investigating what may well be the lowest point in the history of physics. This is not a given: a BBC television programme about the affair *The Dark Secret of Hendrik Schön* is one of the worst documentaries I have ever seen. (In the interests of transparency I should also point out that the publishers of *Nature Nanotechnology* and the publishers of the book under review are owned by the same company, MacMillan.)

Reich has interviewed more than 100 people involved in the story, and also seen a large number of e-mails from the time, including a number of referee reports on Schön's papers (although the journals involved did not hand over their files to the Beasley committee). And while it is a pity that she did not manage to interview Schön himself, the book does not suffer as a result. The picture of Schön that emerges is not of someone confident or arrogant, as one might expect, but of a harmless almost hapless character who seems unembarrassed by his inability to answer many of the questions put to him by colleagues and other people in the field, preferring instead to belatedly respond to criticisms and suggestions by conjuring up another ground-breaking paper a week or two later, often by working backwards from what he felt the result should be.

The book's real strength is the way it uses a journalistic approach to document what was happening on a week-by-week basis at Bell Labs (a legendary lab with a string of Nobel prizes, now presided over by an ever-changing cast of managers and owned by a company beset by the dot com crash and looking for the next big technological breakthrough to revive its fortunes), as well as the editorial offices of high-profile journals (for whom chapter 6 will make uncomfortable reading) and other laboratories (UC Berkeley, Minnesota, Delft and elsewhere) trying to produce the results. In doing so Reich uncovers a wealth of detail — especially early concerns about Schön's work raised by colleagues at Bell Labs, notably suspicions by Don Monroe (who was later a member of the Beasley committee) that Schön managed to rebut by fabricating even more data, and a complicated trail that started with Julia Hsu, Lynn Loo and Bob Willett at Bell Labs and, via Lydia Sohn at Princeton, ended with Paul McEuen of Cornell informing the management at Bell Labs and various journals, thus prompting the official investigation — that has not been published before. There are probably still more secrets under lock-and-key at Murray Hill and elsewhere, but for now Reich's engrossing book will be the last word on the matter. ❐

REVIEWED BY PETER RODGERS

Peter Rodgers is the Chief Editor of Nature Nanotechnology.

DNA ORIGAMI

Folded into three dimensions

Nano Lett. doi: 10.1021/nl901165f (2009); *Nature* **459,** 73–76 (2009)

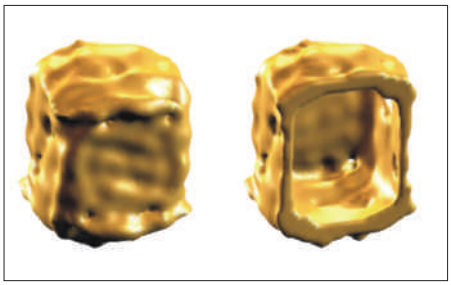

DNA is a natural polymer with nanoscale geometry. It is comprises a backbone of repeated sugar–phosphate units, with one of the four bases — adenine (A), cytosine (C), guanine (G) or thymine (T) — attached to each sugar. The base-pairing rules (A–T and C–G) that form the double helix can also be exploited to build self-assembled nanostructures. One promising approach to DNA nanotechnology, introduced by Paul Rothemund in 2006, uses a lengthy single strand of DNA that is folded into a shape using a number of shorter 'stapling' strands. Known as 'DNA origami', the method can produce large, two-dimensional nanostructures of intricate design. Now, two independent research groups have moved DNA origami into the world of three-dimensional designs.

Hao Yan and colleagues at Arizona State University and Aarhus University used a modified DNA origami approach to build a DNA tetrahedron in which the edge of each triangular face is around 54 nm in length. Alternatively, Kurt Gothelf, Jørgen Kjems and colleagues in Denmark and Germany have created a DNA origami box 42×36×36 nm^3 in size. The box also incorporates a controllable lid, which can be opened by supplying the appropriate DNA 'keys'.

Both groups envisage using their miniature containers to hold other species, such as enzymes or metallic nanoparticles, and the packages could be used for drug delivery or as sensors.

NEMS

To the max

Nature **458,** 1001–1004 (2009)

Nanoelectromechanical systems (NEMS) are used in applications as diverse as fundamental physics and biosensing. At the centre of any NEMS device is a small beam that vibrates with a natural frequency. A wide range of methods are used to make this beam start vibrating in the first instance, and to measure how the vibration frequency changes as, for example, molecules stick to it.

Existing actuation schemes for starting the vibrations can either be on-chip or external, but both approaches have disadvantages, such as high levels of dissipation for the former and problems at high frequencies for the latter. Physicists at the Ludwig Maximilians University in Munich have now demonstrated a new approach to this task that avoids many of these disadvantages.

Jörg Kotthaus and co-workers used gold electrodes to create an inhomogeneous electric field in the vicinity of their nanobeam, and then relied on the fact that any polarizable material — such as a nanobeam made of silicon nitride — will experience an attractive force that moves it towards the region of maximum field strength. If a second pair of electrodes is added, this dielectric gradient force can also be exploited to detect the motion of the nanobeams.

SERS

Trying to do it all

PLoS ONE doi:10.1371/journal.pone.0005206 (2009)

Antibodies labelled with fluorescent dyes are commonly used to detect antigens on the surface of cells, or to identify biochemical processes inside cells. However, the overlapping emission spectra of these dyes make it difficult to detect several events simultaneously. Researchers at Stanford University have now shown that surface-enhanced Raman scattering (SERS) of nanoparticles can be combined with Raman dyes to give a multicolour method that is able to detect antigens and multiple biochemical events in single cells.

Using a method developed at Intel, Garry Nolan and co-workers made 60-nm composite organic–inorganic nanoparticles (COINs): these are clusters of silver nanoparticles that contain highly active Raman dyes with specific 'fingerprints' for detection. A specific antibody that binds to the antigen of interest on the surface of the cell was attached to each COIN and delivered to the cells. The Raman spectrum of the cells was then analysed for the relevant fingerprint. In this way, the Stanford team could identify specific antigens on cells and detect two simultaneous biochemical signalling events in a single cell.

Although this COIN-based approach still lags behind those based on quantum dots, it is potentially capable of measuring many more simultaneous events in the cell because it is independent of fluorescence and has well-defined fingerprints. Furthermore, unlike traditional fluorophores, COINs can be excited by different wavelengths and so can be readily used on any equipment.

NANOCLUSTERS

Bouncing back

Phys. Rev. E **79,** 031309 (2009)

When two objects collide, one expects them to lose some or all of their speed owing to the dissipation of heat. Now it seems that this rule doesn't necessarily apply in the nanoworld. Researchers in Japan have shown that nanoscale clusters of atoms can collide and then bounce apart with more kinetic energy than they started with.

Hiroto Kuninaka at Chuo University in Tokyo and Hisao Hayawaka at Kyoto University ran computer simulations of head-on collisions between two clusters, each containing several hundred atoms. They found that clusters with low attractive forces and relatively high temperatures could rebound at speeds up to 1.05 times their speed before the collision.

The researchers explain that the atoms in the clusters vibrate more vigorously at high temperatures, and if enough of them happen to be vibrating in the right direction they give an extra push during the collision. This may seem to violate the second law of thermodynamics, but actually highlights the fact that thermal motions have a large effect on nanosize objects.

This phenomenon could have strong implications in the development of nanoscale devices. It could even apply to dust particle collisions in space — the first steps in forming planets.

DNA NANODEVICES

Orchestrating conductance

Nature Chem. **1,** 156–159 (2009)

As well as its many useful properties in genetics and, more recently, the design of functional nanomaterials, DNA can also conduct electricity. However, the conductivity of an individual strand of DNA strongly depends on the sequence

of the four bases — adenine, cytosine, guanine and thymine — in the strand. Now, Kiyohiko Kawai, Tetsuro Majima and co-workers at Osaka University have shown how a small modification to one of these bases can make the conductivity independent of the sequence of bases.

Generally, DNA conducts charge in the form of 'holes' created by the absence of an electron in the highest occupied molecular orbital of guanine bases. Unfortunately, this means that sequences with excess adenine–thymine pairs show much lower conductivity than sequences with excess guanine–cytosine pairs. To overcome this problem, Kawai, Majima and co-workers replaced one nitrogen atom in each adenine molecule with a carbon–hydrogen group to create 7-deazaadenine. This small change raises the highest occupied molecular orbital of each adenine–thymine pair to be closer to that of the guanine–cytosine pairs, without affecting the base-pairing process in the molecules.

The Osaka team tested the charge-transfer properties of several different DNA sequences, and found that all were improved by making this small change to adenine bases. The conductivity could be improved even further by modifying cytosine and thymine.

SURFACE PLASMONS

A new wave

Phys. Rev. Lett. **102,** 153903 (2009)

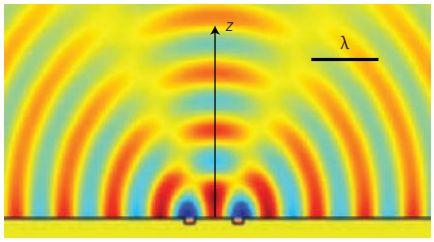

A surface plasmon is a collective excitation of electrons on a surface. As surface plasmons have much shorter wavelengths than the light that excites them, they have a key role in sub-wavelength optoelectronic devices. Recently, however, they have been joined by another type of surface excitation called a cylindrical wave, and researchers have been working to understand the interactions between these two types of excitations as part of efforts to explain the anomalously high transmission of light through nanohole arrays.

Now, Xiaoyan Yang, Haitao Liu and Philippe Lalanne from the University of Paris-South, Huazhong University and Nankai University have shown through simulations that cylindrical waves can scatter into plasmons and vice versa. The conversion process is expected to happen whenever there are subwavelength particles arrayed on a metal surface. Furthermore, the conversion efficiency is shown to have a simple inverse dependence on the permittivity of the metal surface involved.

The results show that nanostructure arrays on surfaces, which are regularly used to generate and control plasmons, also generate cylindrical waves, and that the scattering processes identified by Yang and co-workers may lead to pronounced interference effects for periodic nanoparticle ensembles.

NANOCRYSTALS

Blinking problem solved

Nature doi: 10.1038/nature08072 (2009)

Semiconductor nanocrystals are widely used in biological imaging, but they experience a problem known as blinking — photoluminescence from the nanocrystals switches off and on, seemingly at random, even when the laser exciting the luminescence is constantly turned on. Now Todd Krauss and co-workers at the University of Rochester, Eastman Kodak, Cornell University and the Naval Research Laboratory have made nanocrystals that do not blink.

When a nanocrystal is illuminated by a laser, an electron is excited to a higher energy level, leaving a hole behind. The electron and hole then recombine, emitting a photon with a wavelength that depends on the energy difference between the ground and excited states — which in turn depends on the radius of the nanocrystal. Previously, it was thought that a nanocrystal stops emitting light when it is charged. However, Krauss and co-workers have now shown that nanocrystals with a CdZnSe core and a ZnSe shell will continue to emit at their characteristic wavelengths, even when they are charged, although the broadness of the emission peaks will be a disadvantage for imaging applications.

Krauss and co-workers show that the properties of the nanocrystals can be explained by the recombination of a charged exciton — an exciton plus another charge — in a nanocrystal, where there is a gradual rather than abrupt transition between the core and the shell.

The definitive versions of these Research Highlights first appeared on the *Nature Nanotechnology* website, along with other articles that will not appear in print. If citing these articles, please refer to the web version.

Top down Bottom up

Blood ties

Magnetic nanoparticles are useful tools for tissue engineering and regeneration.

Melissa Krebs and Randall Erb are graduate students working on different subjects at different universities in different cities. They are also brother and sister — and recently their wish to work together sparked a collaboration on tissue engineering that means they are now co-authors as well (*Nano Lett.* **9,** 1812–1817; 2009).

Krebs is a student of Eben Alsberg, an expert on tissue engineering at Case Western Reserve University in Cleveland, Ohio, whereas Erb works on magnetic nanosystems in Benjamin Yellen's group at Duke University in Durham, North Carolina. Together with their advisers, the brother and sister devised a project that would draw on the expertise of each group: the use of a magnetic fluid to tie mammalian cells together.

The goal of the experiments, which also involved researchers from the University of Massachusetts, was to regenerate tissue by controlling the spatial arrangement of cells within a biomaterial matrix. Although a variety of approaches exist, they are often compromised by being slow, expensive or damaging to the cells.

Krebs, Erb and co-workers used inert, biocompatible ferrofluids to drive cells into linear structures under an applied magnetic field. The technique does not require special surfaces, the cells are not modified and no toxic chemicals are needed. The nanoparticles making up the ferrofluid can be removed after the assembly, allowing the structure to be transferred to a cell culture surface.

Such collaborations can be indispensable in some areas of medicine according to Alsberg. "It is often difficult to advance complex fields such as regenerative medicine without the contributions of researchers with often disparate backgrounds," he explains, adding that this particular multidisciplinary project had another advantage: "The collaboration arose through fortuitous circumstances since Mrs Krebs and Mr Erb are siblings. Dr Yellen was not aware of the work my lab was doing, and the opposite was true as well".

NANOMATERIALS

Viruses electrify battery research

A new approach to making battery electrodes with the help of genetically engineered viruses could reduce costs and improve environmental sustainability.

Jean-Marie Tarascon

Over the past two decades, the performance of rechargeable lithium-ion batteries has improved greatly[1], and these batteries now offer both high energy density (~200 W h kg^{-1}) and high specific power (~4.5 kW kg^{-1}). This performance makes them attractive for use in applications such as hybrid and electric cars, and solar and wind energy storage. Challenges to be overcome include lowering costs, improving safety and reducing environmental impact.

Lithium-ion batteries rely on the extraction of positive lithium ions from one electrode and their insertion into the other. Electrons flow at the same time in the external circuit. Research has focused on new electrode materials, and several cheap and abundant examples have been recently identified. These include iron-based phosphates and silicates, made from elements that are major constituents of the Earth's crust and are therefore practically unlimited in quantity.

There is, however, one important drawback to these otherwise attractive materials: their extremely low ionic and electronic conductivity. This can be partially addressed by using nanoscale materials to shorten the distances that the electrons and the lithium ions have to travel. Although the advantages of nanostructured electrodes are well understood, their rational design remains a key challenge for the chemistry and materials communities. In particular, a critical question for battery researchers today is whether nanostructured electrodes can be made by eco-efficient processes with a small carbon footprint.

Now in *Science*, Angela Belcher and colleagues at Massachusetts Institute of Technology (MIT) and the Korea Advanced Institute of Science and Technology (KAIST) report an elegant way of addressing some of these concerns[2]. Building on previous work in which they showed how a virus called M13 can be genetically engineered (Fig. 1, bottom) to provide a template for the growth of negative electrodes[3], Belcher and colleagues now apply the same biological principles in a new direction: the growth of a positive electrode based on amorphous iron phosphate (a-$FePO_4$). They find that engineering a single virus gene to nucleate iron phosphate results in electrodes that have acceptable capacity retention upon cycling but limited high-power performance. The common response of the battery community to such poor kinetics is to add an electronic conductor, generally a form of carbon, to the mix. Two of the most popular approaches are carbon nanopainting, which gives a thin coating of carbon to the electrodes, and the mechanical addition of carbon nanotubes. Although nanopainting produces a better interface than carbon nanotubes, it also requires high-temperature processing under a reducing environment, preventing its use for oxidizing materials such as ferric oxides .

It is here that the *coup de force* of the paper is found. Belcher and colleagues improve the performance of their iron phosphate electrodes with a new way of incorporating carbon nanotubes (Fig. 1, top). They engineer additional genes so that the M13 virus acquires an affinity for single-walled carbon nanotubes, in addition to its ability to nucleate amorphous iron phosphate. The resulting electrodes show much improved cycling properties, capacity retention and rate capability. Based on spectacular transmission electron microscopy images, the researchers argue that these improvements are the result of the high quality of the interface between the iron phosphate and the nanotubes. Moreover, the quality of the interface means that their electrodes can operate with a smaller amount of nanotubes (5% by weight), avoiding the incorporation of inactive nanotubes that serve only as dead weight, although this benefit is somewhat negated by the presence of inactive viruses.

Undoubtedly, the significance of this work lies in its demonstration of a new direction for the design of nanostructured electrodes, which is more likely to inspire

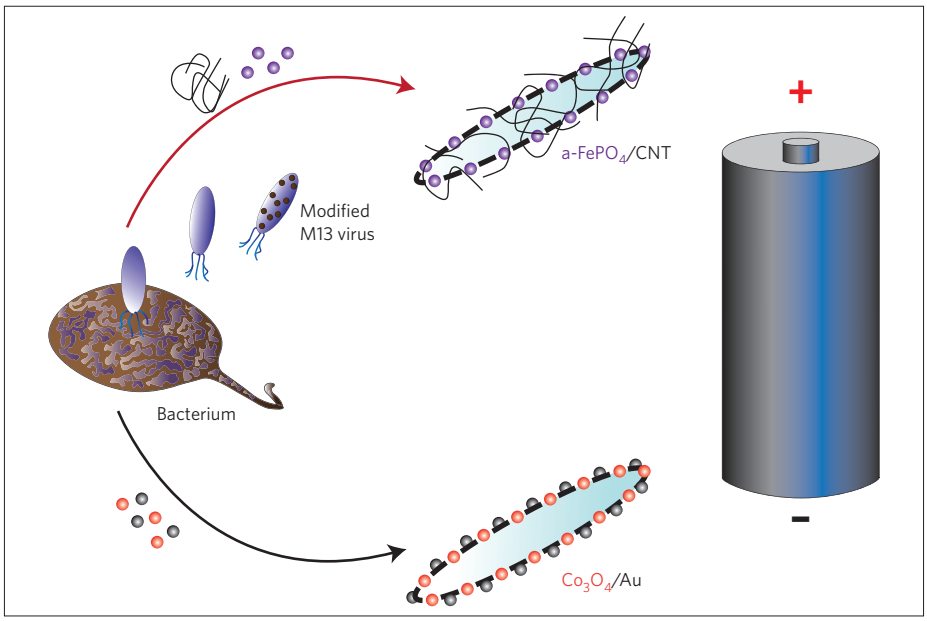

D. LARCHER & J.-M. TARASCON

Figure 1 | Biomimetic electrodes for lithium-ion batteries. Belcher and co-workers have shown that genetically modified M13 viruses can be used to make negative electrodes based on Co_3O_4 nanowires and gold nanoparticles[3] (bottom), and positive electrodes based on a-$FePO_4$ nanowires and carbon nanotubes (CNT, top)[2]. This particular pair of electrodes could not be used together because a Co_3O_4 negative electrode requires a lithium-based positive electrode.

future work, rather than lead directly to the design of new electrodes for lithium-ion batteries, as some press headlines have implied. Indeed, it is unlikely that iron phosphate/nanotube electrodes, which are lithium-free, will be used in commercial lithium-ion batteries because at least one of the electrodes in these batteries needs to contain lithium. Lithium metal cannot be used for the negative electrode for reasons of safety and cyclability, and lithium graphite (LiC_6) is too reactive. (LiC_6 is actually formed at the graphite negative electrodes in commercial lithium-ion batteries, but it is safe because it is sealed from air and moisture inside the battery). Belcher and co-workers are therefore planning to investigate the virus-based growth of lithium-containing positive electrode materials which have been previously disregarded because of their poor electronic conductivity.

One such material, $LiFePO_4$, is currently considered among the most attractive of electrode materials[4], and electrodes assembled from $LiFePO_4$ nanopowders have already reached the marketplace. Proposing a biological approach to making electrodes that are already on the market may result in some scepticism, which could have been allayed by a more candid discussion of the limitations and drawbacks of the virus-based approach in ref. 2. Nevertheless, battery research needs bold new approaches, and the work of Belcher and co-workers should drive the community to think out of the box, and raise awareness of the benefits of biotechnology approaches.

Can we, for instance, make such biological electrode wiring universal and trick Mother Nature, turning minerals that are abundant, but that are commonly recognized as electric insulators, into battery electrode materials? Nature already, for instance, handily manipulates phosphate species, breaking the strong phosphorus–oxygen bond (DNA and ATP); and mother-of-pearl is an extraordinary organic–inorganic composite made in billions of tonnes every year. Can these materials and processes serve as the inspiration for future bio-inspired electrode materials? Although these questions lack a clear answer today, it is a certainty that, for reasons of sustainability, the way we make electrode materials and electrodes will change in the coming decades. Whatever the solution will be, it remains that the work by Belcher and colleagues marks an advance in the design of electrode materials. The synthesis of the electroactive material and its implementation into a working electrode occur at room temperature, and this is surely a good thing. ❐

Jean-Marie Tarascon is at the Université de Picardie Jules Verne, 80039 Amiens Cedex, France.
e-mail: jean-marie.tarascon@sc.u-picardie.fr

References

1. Tarascon, J. M. & Armand, M. *Nature* **414,** 359–367 (2001).
2. Lee, Y. J. *et al. Science* doi: 10.1126/science.1171541 (2009).
3. Nam, K. T. *et al. Science* **312,** 885–888 (2006).
4. Padhi, A. K. *J. Electrochem. Soc.* **144,** 1188–1194 (1997).

TOXICOLOGY

Testing in the third dimension

Experiments with a new three-dimensional model of liver tissue find that the toxic effects of nanoparticles are reduced when compared with tests that use two-dimensional models.

Molly M. Stevens

Cells reside in a three-dimensional (3D) environment in the body and they are sensitive to nanoscale topographical and chemical alterations. The varied landscape of ridges, posts and grooves in the extracellular matrix influences whether a cell will grow or die[1]. Synthetic nanomaterials, which also present a nanoscale landscape, hold enormous promise in biomedical applications, but assessing and predicting their potential toxicity towards cells remains a challenge.

Now in *Small*, Nicholas Kotov and colleagues[2] of the University of Michigan and Nico Technologies report a new 3D model of liver tissue for assessing the toxicity of various nanoparticles. The new culture model aims to bridge the gap between *in vitro* and *in vivo* testing of nanoparticles, and to improve the predictive power of *in vitro* screening procedures.

In vitro tests of the toxicity of nanoparticles on 2D cell cultures have helped describe fundamental mechanisms of how cells interact with materials. This method involves growing the cells of interest on a flat substrate and measuring their response to the test material using various colorimetric, fluorescence, protein and gene expression assays. The problem with these cultures is that they do not reproduce many of the complex cell–cell and cell–matrix interactions found in the natural 3D environment of tissues and organs, and this limitation frequently means that the results from these studies cannot accurately predict outcomes in animal experiments.

Three-dimensional cell cultures in the form of tissue 'spheroids' are routinely used in cancer and pharmaceutical testing and are expected to be effective models for toxicity studies because they could potentially approximate the *in vivo* tissue structure and cell behaviour more closely than 2D cultures[3]. Liver tissue spheroid models are popular because the liver is the main organ where drugs are metabolized and nanoparticles accumulate. However, the development of simple and reproducible *in vitro* liver toxicity screening models has been hampered by the lack of control over the dimensions and organization of liver spheroids. Because the functional bioactivity of a spheroid is closely related to its diameter, reproducibility is necessary if they are to be used to screen for nanoparticle toxicity.

As a scaffold for growing the 3D liver spheroids, Kotov and co-workers prepared a cell-repulsive transparent polyacrylamide hydrogel[4,5] consisting of highly organized and uniformly sized spherical pores with small openings on the top side, and sub-cell-sized porosity throughout the walls of the scaffold (Fig. 1). Liver cells are delivered through the small openings and after a few days of culture the single cells grow into balls of cells called spheroids that are eventually trapped in the pores. Obtaining quantitative data from such 3D cultures remains challenging, but the well-confined spheroids in this case means that the total number of cells is kept constant and so the effects of different nanoparticles on liver tissue could potentially be characterized. By controlling the size of the pores, it is possible to reproducibly form spheroids that are 100 μm in diameter and still maintain good transport of gas and nutrients throughout the scaffold. Hypoxic conditions, which cause cell death, are a common problem in other poorly controlled spheroid models.

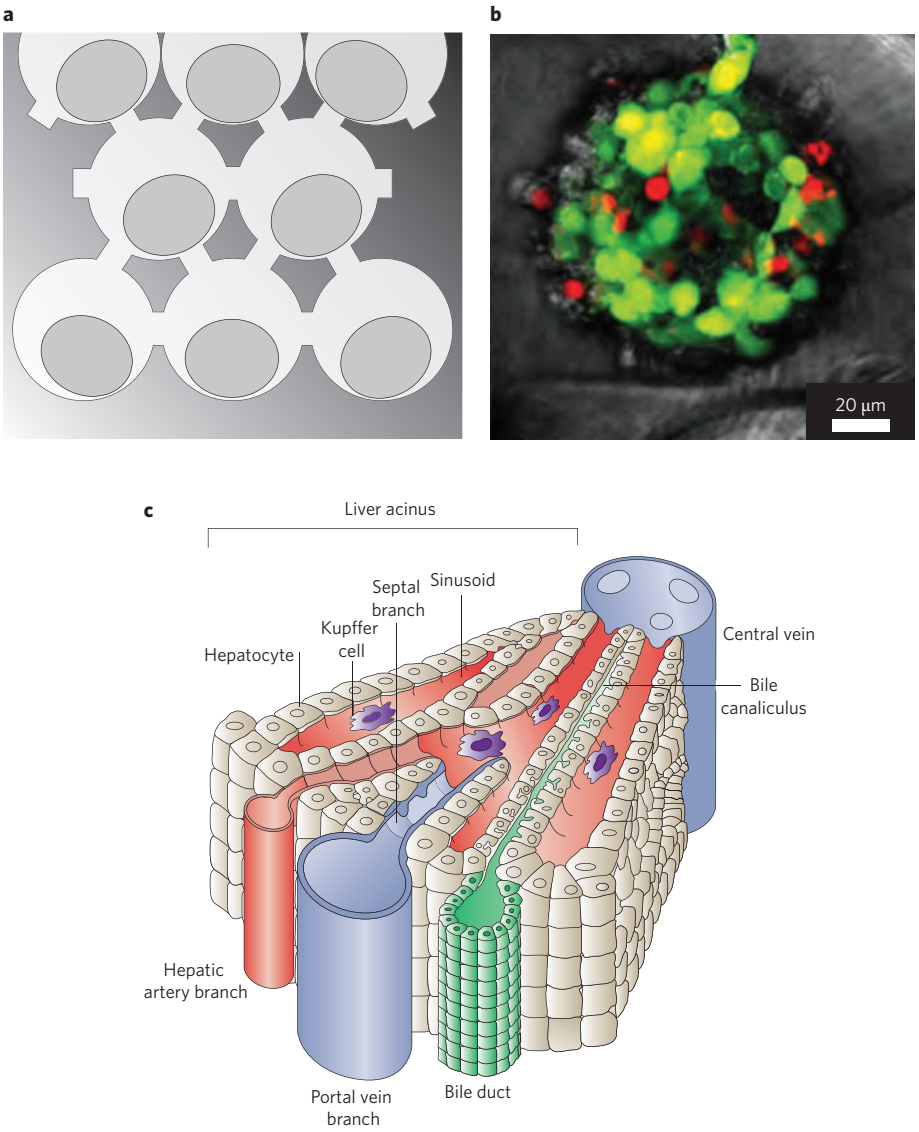

Figure 1 | Architectures of the liver tissue *in vitro* and *in vivo*. **a**, Schematic of the scaffold of the 3D spheroid model. Pores (light grey circles) in the hydrogel are made using a colloidal crystal template. Liver spheroids (dark grey circles), composed of liver cells, grow to 100 µm in diameter and are trapped in the pores. **b**, Confocal image of a 3D spheroid culture after 12 h of exposure to CdTe quantum dots. Live cells are green and dead cells are red. **c**, The liver tissue is complex with arteries (red) bringing blood in and veins (blue) taking it out, bile ducts (green) for the excretion of waste products, and various types of cells, such as Kupffer cells — specialist macrophage cells that remove foreign material. In the liver, nanoparticles are immediately taken up by Kupffer cells, so future 3D liver models should also include macrophage cells. Panels **a** and **b** reprinted with permission from ref. 2 (© 2007 Wiley); panel **c** reprinted from ref. 9 (© 2006 NPG).

At present there is no clear consensus on the toxicity profile of quantum dots and many other nanoparticles of biomedical interest because of the variability in test methods, materials and cellular systems[6]. The Michigan–Nico team evaluated the toxicity of cadmium telluride quantum dots and gold nanoparticles in the 3D liver spheroid and compared the results with a conventional 2D cell culture. Significantly lower cell death and fewer morphological alterations in cells were seen in the 3D spheroid cultures.

The results are similar to drug screening studies that show higher drug resistance to anti-cancer drugs in 3D tumour spheroids than 2D cultures and is probably due in part to the spheroids, like natural tissues, being covered with an outer layer of extracellular matrix that can reduce the penetration of certain toxic agents into the inner layers of the cells. The cellular proliferation rate and metabolic activity is also much lower inside the spheroid.

Nonetheless, the absence of cell death does not necessarily mean that the cells are not undergoing any changes in function or signalling, so it remains necessary to determine the biochemical, genomic and proteomic output of cells within this 3D spheroid model. Although such 3D models bring us yet another step closer to recreating the environment in our organs, we are still a long way from reproducing the complex vasculature systems, immune responses and nanoparticle clearance systems in our body. Concurrent advances in tissue engineering may, however, one day allow us to introduce engineered vasculature and bile ducts into larger organ-specific constructs *in vitro* to help mimic *in vivo* processes of clearance and bioaccumulation.

Reproducible 3D tissue models provide an important extension of current testing strategies. However, for widespread use, they should be standardized, simple and adaptable to high-throughput screening. Because of the enormous diversity of nanomaterials[7], such a precise and reproducible screening tool will be useful for quickly assessing structure–activity profiles of toxicity and for identifying coatings that will minimize toxicity. For example, in industries where workers are exposed to quartz, inhalation of small particles of quartz leads to progressive lung disease, yet the same particles with a thin coating of clay are less harmful[8].

Similarly, in cancer therapeutics, screening tools can help identify the necessary surface modifications for enhancing the specific toxicity of nanoparticles. These developments are an essential step forward for engineering safer nanoparticles and for producing physiologically relevant toxicological information. ❐

Molly M. Stevens is in the Department of Materials and the Institute of Biomedical Engineering at Imperial College London, London SW7 2AZ, UK.
e-mail: m.stevens@imperial.ac.uk

References

1. Stevens, M. M. & George, J. H. *Science* **310,** 1135–1138 (2005).
2. Lee, J., Lilly, G. D., Doty, C., Podsiadlo, P. & Kotov, N. A. *Small* **5,** 1213–1221 (2009).
3. Cukierman, E., Pankov, R., Stevens, D. R. & Yamada, K. M. *Science* **294,** 1708–1712 (2001).
4. Lee, J., Shanbhag, S. & Kotov, N. A. *J. Mater. Chem.* **16,** 3558–3564 (2006).
5. Kotov, N. A. *et al. Langmuir* **20,** 7887–7892 (2004).
6. Hardman, R. *Environ. Health Perspect.* **114,** 165–172 (2006).
7. Maynard, A. D. *et al. Nature* **444,** 267–269 (2006).
8. Donaldson, K. & Borm, P. J. A. *Ann. Occup. Hyg.* **42,** 287–294 (1998).
9. Adams, D. H. & Eksteen, B. *Nat. Rev. Immunol.* **6,** 244–251 (2006).

NANOPHOTONICS

Gradient force shows its potential

An all-optical chip-based method has been used to actuate and detect the motion of silicon nanocantilevers. Multiplexed read-out has also been demonstrated.

Mark Freeman and Wayne Hiebert

Improving the sensitivity of measurement techniques is a regular preoccupation of the experimental scientist, and as researchers gain experience with a new technique, they can often transfer it to new platforms and new areas of science. A case-in-point is the position or displacement sensor that is used to measure the deflection of the tiny cantilever carrying the tip in an atomic force microscope (AFM) as the cantilever bends in response to the forces acting on the tip. The first AFM[1] used a scanning tunnelling microscope (which was still very new at the time) as a position sensor, but much more convenient optical read-outs — based on fibre interferometers[2] or 'beam-bounce' and position-sensitive photodetectors[3] — were soon introduced.

The benchmark for state-of-the-art displacement sensitivity soon became tens of femtometres per root Hertz, which allows researchers to detect a deflection equivalent to about 10^{-4} of the diameter of an atom, after one second of signal averaging. On page 377 of this issue, Mo Li, Wolfram Pernice and Hong Tang of Yale University[4] report a significant step towards migrating this capability to semiconductor chips that might be suitable for mass production.

These optical measurement techniques have led to several breakthroughs, including the mechanical detection of magnetic resonance for single electrons[5], mechanical resonators made from graphene[6] and experiments that may soon be able to detect quantized mechanical motion[7]. In all these experiments a high displacement sensitivity allows small changes in the vibrational frequency of the cantilever to be measured, and these changes can be related to forces in the AFM, changes in the mass of the cantilever in nanomechanical mass sensors, and various other interactions between the cantilever and its environment. Cantilever structures (which are clamped at one end and free to vibrate at the other) are approximately two orders of magnitude more sensitive to force than an identical beam clamped at both ends.

The Yale team miniaturizes free-standing silicon waveguide structures that are widely used in optical microelectromechanical systems[8]. A small section of a suspended waveguide structure is cut in the middle to give two nanocantilevers facing each other end-to-end. The separation of the nanocantilevers is narrow enough (200 nm) such that an optical guided wave can happily traverse the gap with relatively minor loss. However, the transmission depends very sensitively on how well the two ends, and their optical modes, overlap (Fig. 1), and this makes it possible to read-out the position of both cantilevers with very high precision. The sensitivity is calibrated by measuring thermomechanical noise, and the Yale team reports a value of 40 fm $Hz^{-1/2}$, which is comparable to the sensitivity of a fibre-interferometric read-out.

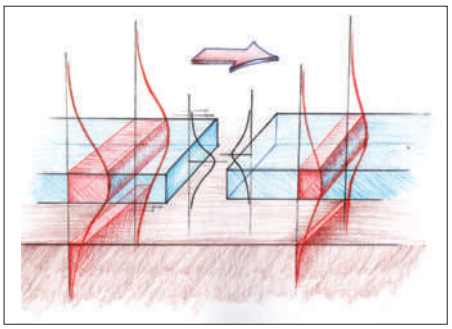

DAVID FORTIN

Figure 1 | Artist's impression of the transduction principle. Light (red) travels from left to right through the cantilevers (blue), with the transmission across the gap depending on the overlap of the optical profiles (black). An optical gradient force between the cantilevers and the substrate (brown) drives the cantilever oscillations when the optical power is modulated at the cantilever frequency; the optical power crossing the gap is modulated at the same frequency. A gradient force is established when the evanescent optical field from the cantilever reaches the substrate (which is about 350 nm below the cantilever). In practice, one wavelength of light is used to drive the oscillations of the cantilever, and a second wavelength is used to detect the displacement.

This miniaturization simultaneously brings into play several other features that combine to make an attractive platform for chip-scale integration: optical actuation, wavelength multiplexing and a read-out method that does not depend on wavelength. The actuation method, introduced by the same group in 2008, takes advantage of optical gradient forces[9] to make the cantilever oscillate: the evanescent field of an optical guided wave travelling along the cantilever also travels through the nearby substrate, and energy minimization gives rise to a gradient force between the cantilever and the substrate. Similar forces have been exploited in optical tweezers for decades[10]. Unlike other actuation techniques, the gradient-force method has the distinct advantage of having no inherent bandwidth limitation (other than how quickly the light power can be modulated).

This actuation method is related to light power in the waveguide, as is the method used to detect the position of the nanocantilever, which bodes well for integration with photonic platforms. Furthermore, the all-optical approach is inherently broadband[11], whereas most electronics approaches to transduction (that is, actuation or detection) are limited in bandwidth.

A bonus of the optical read-out is that it works without using interferometric effects, as demonstrated by the fact that the observed sensitivity is independent of wavelength over a 30 nm spectral range. This means that low-cost light sources could be used for both actuation and detection, making this approach very amenable to chip-scale integration. Integrated applications could benefit from this wavelength insensitivity and could also use different wavelengths to address selected cantilevers in the array.

The Yale team demonstrates multiplexing by focusing on a small array of cantilevers with suitable multimode interference input and output couplers. These couplers exploit the interference patterns that develop when light diffracting out of the end of a waveguide propagates into the wider cavity of the device.

Challenges remain before complex photonic circuits will be able to incorporate vast arrays of nanocantilever devices. Part

of the exquisite sensitivity comes from the relatively high optical powers used. With low-loss waveguides, the power could be routed and reused for multiple devices, but the 3 dB that is lost every time the gap is crossed needs to be improved. Also, the fact that the sensitivity depends on the initial alignment of opposing cantilevers will make device-to-device repeatability difficult to achieve. The detection method is also extremely sensitive to the local environment just outside the sensor (similar to evanescent field sensors[12]), as well as to the displacement of the cantilever, which could complicate sensing applications. It also remains to be seen how much this approach can be down-scaled in size, and if it will be competitive for single-molecule mass sensing and spectrometry[13,14].

The nanomechanics work of the Yale team is part of a broader research effort including like-minded efforts in nanophotonics and nanoelectronics that, if it can overcome these challenges, will provide the massive, established base of silicon technology with new optical functionality. ❐

Mark Freeman[1,2] and Wayne Hiebert[2] are in the [1]Department of Physics, University of Alberta, Edmonton T6G 2G7, Canada, and the [2]National Institute for Nanotechnology, Edmonton T6G 2M9, Canada.
e-mail: mark.freeman@ualberta.ca; wayne.hiebert@nrc-cnrc.gc.ca

References
1. Binnig, G., Quate, C. F. & Gerber, Ch. *Phys. Rev. Lett.* **56,** 930–933 (1986).
2. Rugar, D., Mamin, H. J., Erlandsson, R., Stern, J. E. & Terris, B. D. *Rev. Sci. Instrum.* **59,** 2337–2340 (1988).
3. Meyer, G. & Amer, N. M. *Appl. Phys. Lett.* **53,** 1045–1047 (1988).
4. Li, M., Pernice, W. H. P. & Tang, H. X. *Nature Nanotech.* **4,** 377–382 (2009).
5. Rugar, D., Budakian, R., Mamin, H. J. & Chui, B. W. *Nature* **430,** 329–332 (2004).
6. Bunch, J. S. *et al. Science* **315,** 490–493 (2007).
7. Kippenberg, T. J. & Vahala, K. J. *Science* **321,** 1172–1176 (2008).
8. Ollier, E. *IEEE J. Sel. Top. Quant.* **8,** 155–162 (2002).
9. Li, M. *et al. Nature* **456,** 480–484 (2008).
10. Ashkin, A. *Phys. Rev. Lett.* **24,** 156–159 (1970).
11. Liu, N. *et al. Nature Nanotech.* **3,** 715–719 (2008).
12. Armani, A. M., Kulkarni, R. P., Fraser, S. E., Flagan, R. C. & Vahala, K. J. *Science* **317,** 783–787 (2007).
13. Jensen, K., Kim, K. & Zettl, A. *Nature Nanotech.* **3,** 533–537 (2008).
14. Yang, Y. T. *et al. Nano Lett.* **6,** 583–586 (2006).

SEPARATION MATERIALS

Proteins make for finer filters

Protein-based membranes can cope with water fluxes much higher than those that can be handled by commercial membranes with similar rejection properties.

Olgica Bakajin and Aleksandr Noy

Membrane interfaces are unsung heroes of the modern world. They permeate its every aspect, yet they rarely get the spotlight. The basic concept is deceptively simple: a membrane barrier allows some molecules to pass through it while stopping others. Membranes provide one of the most energy-efficient ways to separate chemical species on the basis of size, charge or chemical properties. Modern industrial membrane technology, dominated by polymer membranes, is used in applications as diverse as dialysis for kidney patients and the supply of clean drinking water. The market for membranes is worth billions of dollars per year, but there is still plenty of scope for improvements in performance. On page 353 of this issue, Izumi Ichinose and colleagues at NIMS and CREST in Japan report an alternative to polymer membranes based on the self-assembly of biological building blocks[1].

It is no surprise that biology serves as inspiration for membrane development. Biological membranes enable living systems to function without rapidly descending into a state of entropically driven chaos. Cells use a dizzying array of sophisticated pores that range from passive channels called aquaporins in kidneys to sophisticated ion pumps and ion channels in heart tissue. The simplest example of a biological membrane, but also one of the most elegant, is the S-layer that some bacteria use to protect their outermost walls (Fig. 1a). This crystalline layer, composed of a single glycoprotein, provides a barrier with a defined porosity between the bacteria and the outside world. The 2–3-nm pores between the proteins provide ample room for nutrients and metabolites to pass back and forth, while protecting the bacteria from enzymes and phages.

In 1987, Margit Sára and Uwe Sleytr of the University of Natural Resources and Applied Life Sciences in Vienna separated the S-layer from some bacteria, placed it on a solid support and then crosslinked the proteins to create the first biologically derived ultrafiltration membrane[2]. These S-layer

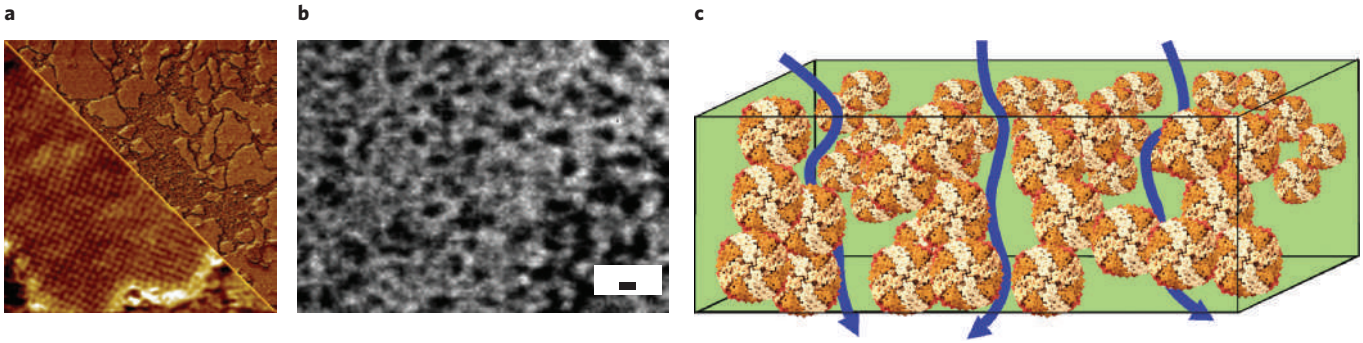

Figure 1 | Different types of filtration membranes. **a**, Atomic force microscope images of the S-layer proteins at low (right; image is 5 μm wide) and high (left; 500 nm) resolution. Data courtesy of Veeco Instruments Inc. **b**, Transmission electron micrograph of a polymer membrane; scale bar 2 nm. Figure reproduced with permission from ref. 5 (© 2004 ACS). **c**, Schematic diagram of a membrane made from crosslinked ferritin subunits[1]. The blue lines indicate liquid passing through the cross-linked membrane. The average diameter of a ferritin molecule is 12 nm.

membranes are stable over a wide range of pH values, and their size rejection curve is unusually steep compared with the rejection characteristics of polymer-based membranes.

Unfortunately, it was not possible to scale up the production of biologically derived membranes, so researchers and the membrane industry focused instead on the use of synthetic building blocks to make membranes with more uniform pores[3]. Some of the most successful of these synthetic strategies use self-assembly of block copolymer templates to generate a regular lamellar structure and then to convert it into a membrane by removing one of the polymer components. Takeji Hashimoto and colleagues at Kyoto University first demonstrated this process by synthesizing a microdomain-separated polystyrene–polyisoprene film and then degrading the polyisoprene component with ozonolysis to leave channels in the film[4]. Further refinements, such as the use of triblock copolymers, have increased the tunability and control over the system. Anne Mayes of the Massachusetts Institute of Technology and collaborators[5] used a similar polymer-based approach to make a membrane that could cope with water fluxes (or permeances) as high as 9 l h^{-1} m^{-2} bar^{-1}.

Ichinose and colleagues have combined these concepts in an experiment that uses self-assembly of globular proteins on sacrificial nanofilament templates to produce an extremely permeable and robust membrane (Fig. 1c) with rejection properties similar to ultrafiltration membranes with a low molecular mass cut-off. This fabrication technique is remarkably versatile and can use many different globular protein building blocks. The Japanese researchers chose ferritin because it produced membranes with very high permeances. They started by organizing ferritins on cadmium hydroxide nanostrands and then assembled them into a filter cake. After crosslinking the proteins they removed the metal hydroxide, leaving an extremely chemically resistant 60-nm-thick membrane that was stable in organic solvents and in a wide range of pH values (1.5 to 13). Remarkably, the pores were less than 2.2 nm across, and the water permeance could be as high as 9,000 l h^{-1} m^{-2} bar^{-1}.

Ichinose and colleagues also explored the rejection properties of their ferritin membranes using a wide range of analytes and solution conditions. Although more experiments will be needed to characterize the molecular mass cut-off completely, and to understand the rejection mechanisms in all their complexity, several trends are clear. First, it is evident that pH changes can modulate the pore size to some extent. Second, the shape of the molecule is important: TMPy, a square-planar porphyrin with a molecular mass of ~680 Da, was almost completely rejected, whereas PSS, a linear polyelectrolyte with a molecular mass of ~7,000 Da, passed through the membrane. It is possible that further engineering of ferritin or other protein building blocks could allow further fine-tuning of membrane cut-off and rejection properties.

Finally, the most remarkable and commercially attractive property of the ferritin-based membrane is its combination of high permeance and low molecular mass cut-off (courtesy of the small pore size). Indeed, the membranes have permeances comparable to commercial ultrafiltration membranes that have much higher cut-offs, whereas commercial membranes with cut-offs comparable to the ferritin membranes have permeances that are more than two orders of magnitude lower. Ichinose and colleagues attribute this to the short (less than 6 nm in length) nanopores formed between the ferritin molecules.

This new class of protein membranes could potentially be a very attractive replacement for some conventional ultrafiltration and nanofiltration membranes. Better chemical stability may also open new opportunities for separation in the chemical industry. But it remains to be seen whether these protein membranes will be easier to manufacture than their S-layer membrane predecessors, as only a cost-effective manufacturing process will allow them to achieve their full potential in the marketplace. ❐

Olgica Bakajin and Aleksandr Noy are at the Lawrence Livermore National Laboratory, 7000 East Avenue, Livermore, California 94550, USA.
e-mail: bakajin1@llnl.gov; noy1@llnl.gov

References

1. Peng, X., Jin, J., Nakamura, Y., Ohno, T. & Ichinose, I. *Nature Nanotech.* **4,** 353–357 (2009).
2. Sára, M. & Sleytr, U. *J. Membr. Sci* **33,** 27–49 (1987).
3. Ulbricht, M. *Polymer* **47,** 2217–2262 (2006).
4. Hashimoto, T., Tsutsumi, K. & Funaki, Y. *Langmuir* **13,** 6869–6872 (1997).
5. Akthakul, A., Salinaro, R. & Mayes, A. *Macromolecules* **37,** 7663–7668 (2004).

SUPERCONDUCTIVITY

Flat out

How thin can a film of lead be and still retain its ability to conduct electricity? Previous experiments have shown that films with just five layers of lead atoms become superconducting when they are cooled below about 6 K. Now Chih-Kang Shih and co-workers at the University of Texas at Austin have shown that just two layers of lead atoms — which contain just a single channel of quantum-well states — can act as a superconductor (*Science* doi: 10.1126/science.1170775; 2009).

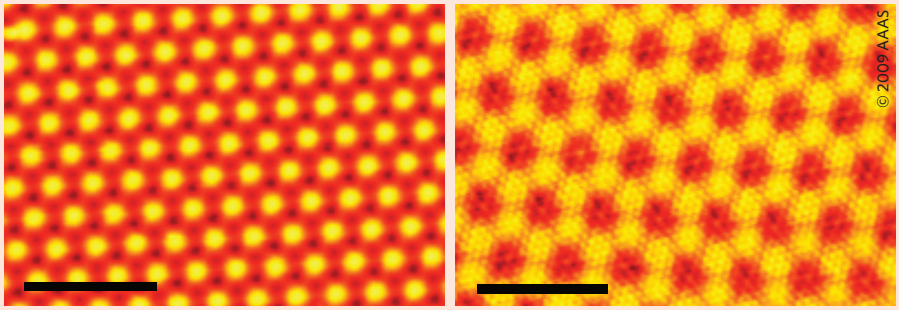

Shih and co-workers found that two layers of lead atoms on a silicon substrate can actually form two different types of lead film. As these scanning tunnelling micrographs show, type-I films have a 1×1 atomic structure and the same lattice parameter as bulk lead (left, scale bar is 10 nm), whereas type-II films have a $\sqrt{3}\times\sqrt{3}$ structure and a similar lattice constant to the silicon substrate (right). The films also have different transition temperatures — 4.9 K for type-I and 3.65 K for type-II — which the Texas team attribute to the type-II film experiencing tensile strain owing to its interaction with the substrate. Films containing three layers of lead atoms are not thermodynamically stable, whereas those containing four layers have a transition temperature of 6.7 K.

PETER RODGERS

QUANTUM DOTS

When a barrier is not an obstacle

Electrons in ultraclean carbon nanotubes can tunnel through barriers in a way not previously observed for particles with mass in condensed-matter physics experiments.

Mahn-Soo Choi

In the quantum world, particles are able to tunnel through the potential energy barriers that would reflect them in the classical world. In non-relativistic quantum theory the probability of tunnelling through such an energy barrier falls exponentially as the height or the width of the barrier increases, but 80 years ago Oskar Klein used Dirac's relativistic theory of the electron to show that relativistic particles can tunnel without any resistance through barriers that are higher than twice the rest-mass energy of the particles[1]. However, this Klein tunnelling is almost impossible to observe directly with electrons or other elementary particles because huge electric fields are needed to produce such high potential energy barriers. On page 363 of this issue, Gary Steele, Georg Gotz and Leo Kouwenhoven of the Delft University of Technology demonstrate[2] a new type of tunnelling in a table-top experiment with carbon nanotubes that is analogous to Klein tunnelling (Fig. 1a). Their work may also pave the way towards spin-based quantum information processing in solid-state devices[3].

Klein tunnelling can be understood in terms of the relationship between the energy and momentum of the particle. In Dirac's theory, energy and momentum are related through two hyperbolic curves that have a gap $\Delta = 2mc^2$ between them, where m is the mass of the particle and c is the speed of light in a vacuum (Fig. 1b). At low energies the relationship between the energy and the momentum is not linear, but for energies much higher than the gap energy, the energy–momentum relation is approximately linear. Similarly, when a Dirac particle encounters a potential energy barrier with a height that is larger than Δ, the energy–momentum relation becomes linear, with the slope inside the barrier being equal to the slope outside the barrier. The particle does not, therefore, recognize the barrier and passes straight through it without any reflection.

One way to overcome the difficulty of making energy barriers with heights greater than $2mc^2$ is to use particles that do not have any mass. Such particles have a linear energy–momentum relation at all energies and can pass freely through barriers of

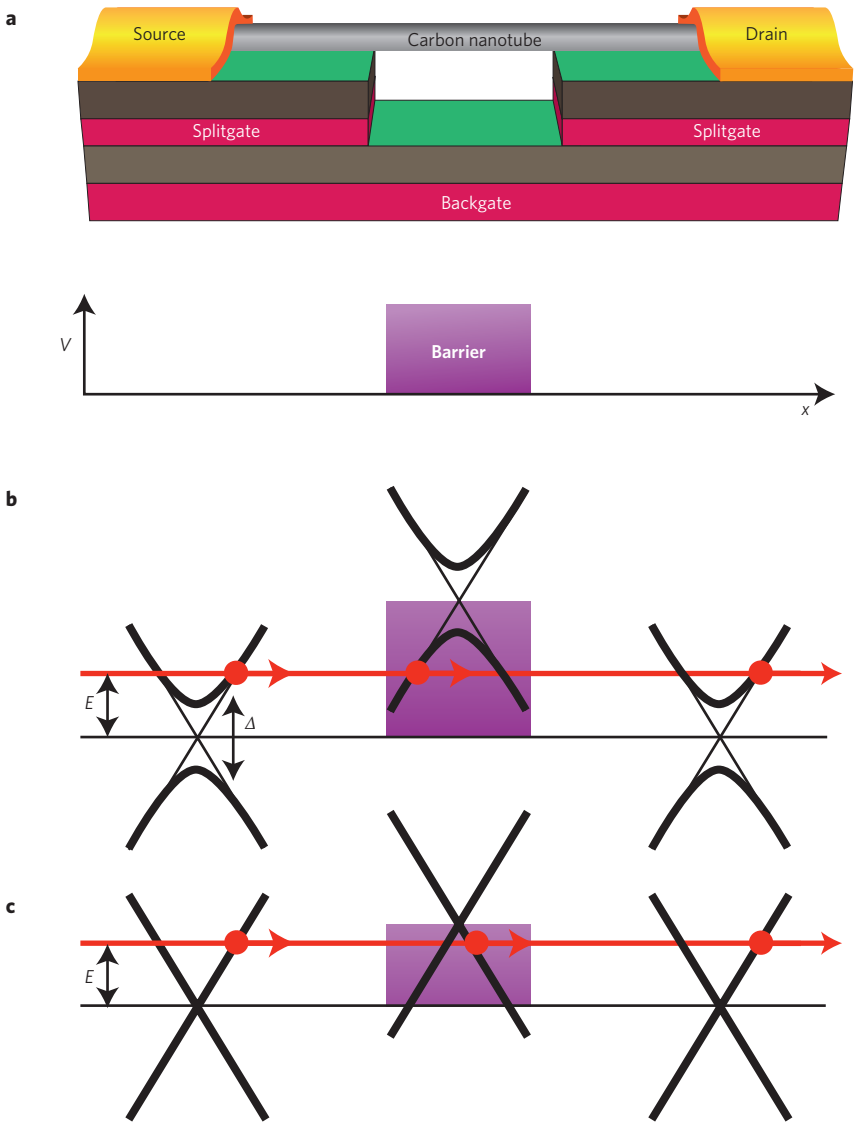

Figure 1 | Klein tunnelling in carbon nanotubes. **a**, A carbon nanotube suspended between source and drain electrodes. The local backgate together with two splitgates can define two quantum dots in the nanotube, and the backgate can be used to control the height of the potential energy (V) barrier (bottom) between these dots. **b**, The relationship between energy (y axis) and momentum (x axis) for a massive Dirac particle in regions with (centre) and without (left and right) a potential energy barrier. The positive energy curve is for particles (such as electrons) and the negative energy curve is for antiparticles (such as positrons). The red circle shows a particle with energy E Klein tunnelling through the barrier. Klein tunnelling is only possible when the height of the barrier is much higher than the gap Δ between the positive and negative energy curves. **c**, The energy–momentum relations of a Dirac particle without mass in regions with and without a potential barrier. A massless particle can tunnel through a barrier of any height.

any height, as has been demonstrated in experiments with graphene[4–6]. Due to its unique lattice structure, quasiparticles in graphene behave like massless Dirac particles over a wide range (a few electron volts) of energy, with a linear relationship between their energy and momentum (Fig. 1c).

Steele and co-workers adopt a different approach, using the energy gap between the valence and conduction bands in semiconducting carbon nanotubes as a proxy for the energy gap between the two solutions to the Dirac equation[2]. They select nanotubes with small bandgaps (25 or 60 meV) so that it is possible to form a potential energy barrier that is much larger than the energy gap with a relatively low electric field.

However, the experimental observation of Klein tunnelling in carbon nanotubes is not straightforward because it requires an extremely clean sample as well as the ability to define and control the potential energy barrier. Placing gate electrodes on top of the nanotubes, the approach taken in many previous experiments, does not work because of the disorder introduced by the deposition process. Recently, very clean devices were made by suspending carbon nanotubes between source and drain electrodes[7], but it was difficult to add the local gates needed to define the quantum dots and control the height of the barrier in these experiments. Steele and co-workers developed a new fabrication method to integrate three independently tunable gate electrodes (one local backgate and two splitgates) with suspended nanotubes. In one device with good contacts between the nanotube and the source and drain electrodes, they were able to construct a potential energy barrier by tuning all three gates, and they went on to observe Klein tunnelling through the barrier.

Furthermore, in another device with less transparent contacts, they constructed double quantum dots, and were able to tune the coupling between them with the backgate. As the gate voltage was varied, they observed both normal tunnelling and Klein tunnelling between the dots. This demonstration is significant because it shows that such a double-quantum-dot device might offer enough tunability to make practical spin-based quantum bits[3], limited only by the effects of Klein tunnelling.

There are, however, still a few issues that need to be clarified. For example, perfect Klein tunnelling (that is, 100% transmission) was not achieved, and an effect called the spin blockade (in which the presence of an electron with, say, spin 'up' on a quantum dot blocks other spin 'up' electrons, while spin 'down' electrons can pass through the dot) was not observed either, so there is still plenty of scope for further breakthroughs. ❐

Mahn-Soo Choi is in the Department of Physics, Korea University, Seoul 136-713, Korea.
e-mail: choims@korea.ac.kr

References

1. Klein, O. *Z. Physik* **53,** 157–165 (1929).
2. Steele, G. A., Gotz, G. & Kouwenhoven, L. P. *Nature Nanotech.* **4,** 363–367 (2009).
3. Loss, D. & DiVincenzo, D. P. *Phys. Rev. A* **57,** 120–126 (1998).
4. Young, A. F. & Kim, P. *Nature Phys.* **5,** 222–226 (2009).
5. Stander, N., Huard, B. & Goldhaber-Gordon, D. *Phys. Rev. Lett.* **102,** 026807 (2009).
6. Katsnelson, M. I., Novoselov, K. S. & Geim, A. K. *Nature Phys.* **2,** 620–625 (2006).
7. Cao, J., Wang, Q. & Dai, H. *Nature Mater.* **4,** 745–749 (2005).

nature nanotechnology

LETTERS

PUBLISHED ONLINE: 12 APRIL 2009 | DOI: 10.1038/NNANO.2009.72

Modular construction of DNA nanotubes of tunable geometry and single- or double-stranded character

Faisal A. Aldaye, Pik Kwan Lo, Pierre Karam, Christopher K. McLaughlin, Gonzalo Cosa and Hanadi F. Sleiman*

DNA nanotubes can template the growth of nanowires[1], orient transmembrane proteins for nuclear magnetic resonance determination[2], and can potentially act as stiff interconnects, tracks for molecular motors and nanoscale drug carriers[3]. Current methods for the construction of DNA nanotubes result in symmetrical and cylindrical assemblies that are entirely double-stranded[2,4–11]. Here, we report a modular approach to DNA nanotube synthesis that provides access to geometrically well-defined triangular and square-shaped DNA nanotubes. We also construct the first nanotube assemblies that can exist in double- and single-stranded forms with significantly different stiffness. This approach allows for parameters such as geometry, stiffness, and single- or double-stranded character to be fine-tuned, and could enable the creation of designer nanotubes for a range of applications, including the growth of nanowires of controlled shape, the loading and release of cargo, and the real-time modulation of stiffness and persistence length within DNA interconnects.

At present, DNA nanotubes are synthesized by vertically aligning DNA duplexes into a curved motif, followed by its closure[4–11], or by rolling and cyclizing a two-dimensional DNA origami array[2]. The method described here involves the initial construction of geometrically well-defined single-stranded and cyclic DNA building-blocks with rigid organic vertices, such as the DNA triangle **3** and square **4** in Fig. 1. These units are then longitudinally assembled via linking strands to form 'rungs', producing nanotubes of predesigned architectures (Fig. 2). The structure of these rungs is what ultimately dictates the final geometry of the nanotubes being constructed, so creating an opportunity to control and modulate the shape and size of each nanotube, one rung at a time. Our group recently developed a class of cyclic and single-stranded DNA building-blocks that are ideal candidates for structural scaffolding[12–14]. These building-blocks contain well-defined synthetic molecules as their corner units. They have been used in DNA nanotechnology to generate nanoparticle assemblies that are structurally addressable in real time, and discrete three-dimensional DNA cages capable of oscillating between several predefined dimensions. Here, we use single-stranded and cyclic triangle **3** and square **4** (Fig. 1) to generate geometrically well-defined triangular and square DNA nanotubes.

To construct a triangular DNA nanotube **3nt**, for example, a single-stranded triangular template **3** is used as a scaffold to first generate a well-defined triangular building-block **3′** (Fig. 2a). This is achieved by hybridizing **3** to three complementary DNA strands (**CS**) that contain sticky-end overhang cohesions to form **3–3**, followed by the addition of three rigidifying strands (**RS**) to spatially orient each of these sticky-end overhangs above and below the plane of triangle **3′**. Three double-stranded linking strands (**LS**) of appropriate sequence then assemble the set of building-blocks **3′** into the well-defined triangular DNA nanotubes **3nt** (Fig. 2b). Considering the ease with which geometrically unique cyclic and single-stranded DNA templates—such as triangles, squares, pentagons and hexagons—have been previously synthesized in our laboratory[15], this approach can be used to generate nanotubes of any arbitrary shape and size. This method enabled the synthesis of square DNA nanotubes **4nt** from the cyclic and single-stranded square template **4** (Fig. 1), using the well-defined square rung **4′** and the double-stranded linking strands **dsLS′** (Fig. 2).

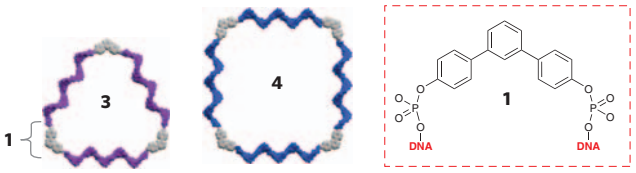

Figure 1 | Single-stranded and cyclic DNA templates 3 and 4.

Initial efforts to make use of this new method focused on constructing **3′** and **4′** from triangle **3** and square **4**, respectively. Accessing the DNA building-blocks **3** and **4** first involves synthesizing a single continuous DNA strand, embedded with the appropriate number of vertex **1** molecules (that is, three for **3** and four for **4**). This is followed by its subsequent cyclization using a template strand of DNA, and its chemical ligation using cyanogen bromide (see Supplementary Fig. S3). Digestion assays using ExoVII confirm the cyclic and single-stranded nature of **3** and **4** (see Supplementary Fig. S4). The assembly of the triangular rung **3′** from one unit of template **3**, three complementary strands with sticky-end overhangs, and from three rigidifying strands, is monitored sequentially using native polyacrylamide gel electrophoresis (PAGE). This process is found to occur quantitatively at every step leading to and including **3′** (see Supplementary Fig. S5). Square scaffold unit **4′** is assembled similarly from template **4** (see Supplementary Fig. S5).

With units **3′** and **4′** in hand, we proceeded to examine their potential to generate well-defined triangular **3nt** and square **4nt** DNA nanotubes. A hierarchical approach was deemed necessary here to ensure the overall fidelity of the assembly process. In the case of **3′**, for example, one of the sides is programmed to contain sticky-end overhangs that are seven bases long, and the remaining two sides contain overhangs that are only five bases long. Therefore, as the mixture slowly cools, the longer sticky-ends cohere first to generate linear assemblies of **3′** molecules, followed by the favourable cohesion of the remaining pre-organized,

Department of Chemistry, McGill University, 801 Sherbrooke Street West, Montreal, Quebec H3A 2K6, Canada. *e-mail: hanadi.sleiman@mcgill.ca

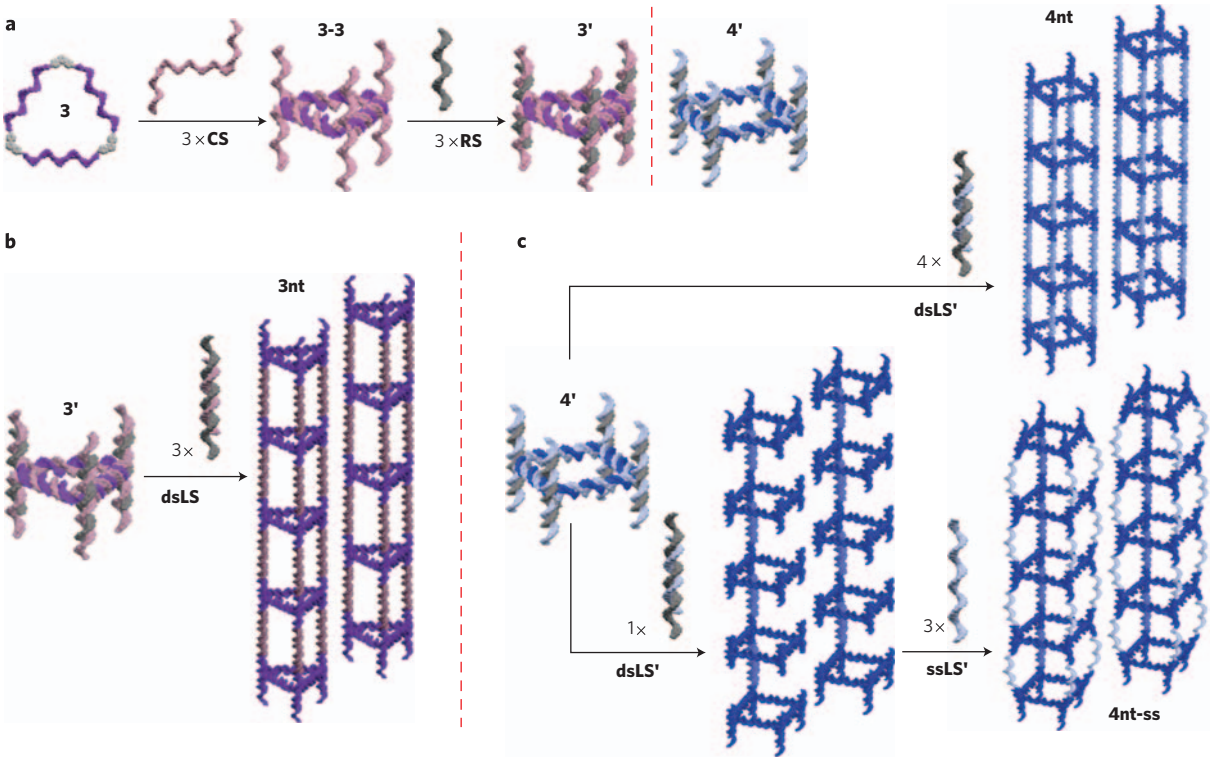

Figure 2 | Construction of DNA nanotubes. a–c, Construction of triangular and square rungs **3′** and **4′** (**a**), triangular nanotubes **3nt** (**b**), square nanotubes **4nt** and single-stranded square DNA nanotube **4nt–ss** (**c**).

shorter sides. This design feature allows a high synthetic yield for constructing the final triangular DNA nanotubes **3nt**. An analysis of the resulting assemblies using atomic force microscopy (AFM) and confocal fluorescence microscopy reveals the formation of well-defined DNA nanotubes extending over several micrometres (Fig. 3; see also Supplementary Information).

Lateral cross-sectional analysis conducted on the triangular nanotubes **3nt** show them all to be of the same height (see Fig. 3a; see also Supplementary Fig. S6b). This is consistent with a well-defined DNA nanotube assembly of a single size. Longitudinal analysis was conducted on the rungs within each nanotube. To do so, we modified each rung with protruding hairpins to provide a visual probe detectable using AFM. Hairpins were introduced into each corner unit of **3′**, to generate **3′–hp,** so that upon assembly, a triangular nanotube **3nt–hp** with hairpins radially protruding from each of its rungs was generated (Fig. 3b). The distance between each rung is estimated to be ~15 nm. A uniform one-dimensional array of hairpins with a periodicity of 45 nm (exactly three times the inter-rung distance of 15 nm) is observed, as confirmed by Fourier analysis of the height trace (see Fig. 3b; see also Supplementary Fig. S10). This is consistent with a 40° rotation of each triangular rung with respect to the next one, and a realignment of the hairpins at every fourth rung (Fig. 3c). Thus, the triangular nanotube assembly **3nt–hp** probably possesses a helical screw axis, with nine rungs for each full turn (see Supplementary Fig. S11). Our approach to constructing DNA nanotubes therefore generates geometrically well-defined DNA nanotubes of excellent uniformity laterally and longitudinally.

DNA nanotubes that are laterally constructed one rung at a time can be easily modulated with respect to size and shape. Thus, in addition to triangular DNA nanotubes **3nt**, geometrically well-defined square DNA nanotubes can be readily achieved by starting with the square DNA template **4** (Fig. 1). Assembly of **4** into **4′** (as with **3′** above) equips this template with cohesive DNA strands above and below its plane (Fig. 2). Addition of double-stranded linking strands **dsLS′** generates square DNA nanotubes **4nt** (Fig. 4a). AFM analysis confirms the construction of highly uniform nanotubes with extension over several micrometres, and shows them to be of uniform size (see Supplementary Figs S7 and S8). In principle, this approach can be seamlessly adapted to construct a new class of designer DNA nanotubes with rungs of different sizes and shapes, with unique sets of structural and functional properties.

DNA nanotubes that can either be completely double-stranded and rigid, or single-stranded and more flexible, can also be constructed using our approach. If the linking strands that join the square rungs **4′** are double-stranded, then fully double-stranded well-defined DNA nanotubes **4nt** are obtained, as described above. However, if three of the four linking strands used within this system are single-stranded, then DNA nanotubes **4nt–ss** with single-stranded regions are generated (Fig. 2). These nanotubes now possess one double-stranded side and three single-stranded sides, and are thus expected to be less stiff. When characterized by AFM analysis, **4nt–ss** nanotube assemblies are found to be significantly more flexible, with relatively shorter distances between regions of bending, when compared with their fully double-stranded analogues **4nt** (see Supplementary Fig. S12). To our knowledge, this is the first example of a DNA single-stranded nanotube. This approach thus allows deliberate control of stiffness and persistence length. It also opens the door to the possibility of using these nanotubes in their more accessible single-stranded form to allow loading of materials such as biomolecules or drugs, and subsequently closing them to their fully double-stranded form to ensure encapsulation.

In summary, we have shown a modular approach to DNA nanotube construction that offers new elements of structural control in the assembly process of these materials. Geometry, size, stiffness, and double- or single-stranded character can all be tuned and modified, thus providing ready access to deliberately designed nanotube architectures. The method uses single-stranded and cyclic DNA templates

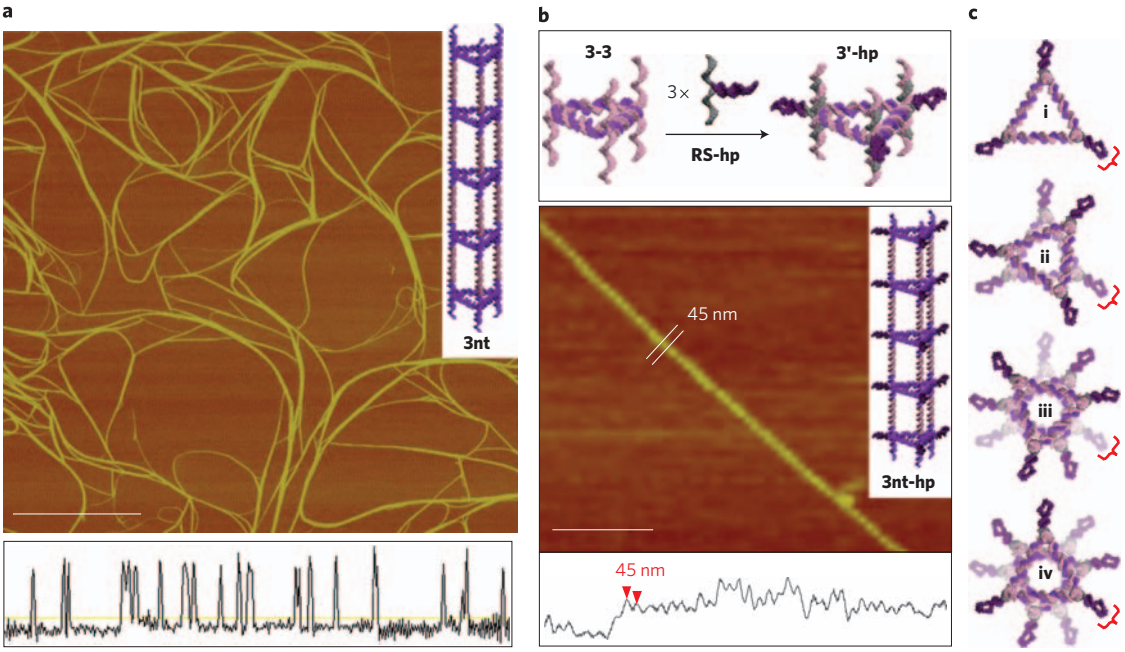

Figure 3 | AFM characterization of triangular DNA nanotubes. a, The construction of DNA nanotubes **3nt** from triangle **3′** results in well-defined one-dimensional DNA assemblies that extend over several micrometres, which from cross-sectional analysis (lower half of figure) are shown to be of the same diameter. Scale bar, 2.5 μm. **b**, Hairpins incorporated into the corner units of each triangular rung **3′–hp** using rigidifying strands **RS–hp** assemble into triangular DNA nanotubes **3nt–hp** with radially protruding hairpins from each of the corner units. Cross-sectional analysis (lower half of figure) reveals a spacing between each consecutive hairpin of 45 nm (exactly three times the distance between two consecutive rungs) in which each rung is rotated by an angle of 40°. Scale bar, 1 μm. **c**, To better illustrate the helicity within **3nt–hp**, a top-view sectional analysis is shown. (i) A single hypothetical hairpin is selected within rung 1. (ii) Superimposition of rung 2, separated from rung 1 by a distance of 15 nm and rotated by an angle of 40°, does not result in the alignment of any of its hairpins onto any of those within rung 1. (iii) Rung 3, now separated from rung 1 by a distance of 30 nm and rotated with respect to rung 1 by an angle of 80°, still does not align. (iv) Rung 4, however, which is now separated from rung 1 by a distance of 45 nm and is rotated with respect to rung 1 by an angle of 120°, is superimposed onto the hairpins being monitored within rung 1, and thus results in the experimentally observed periodicity of 45 nm.

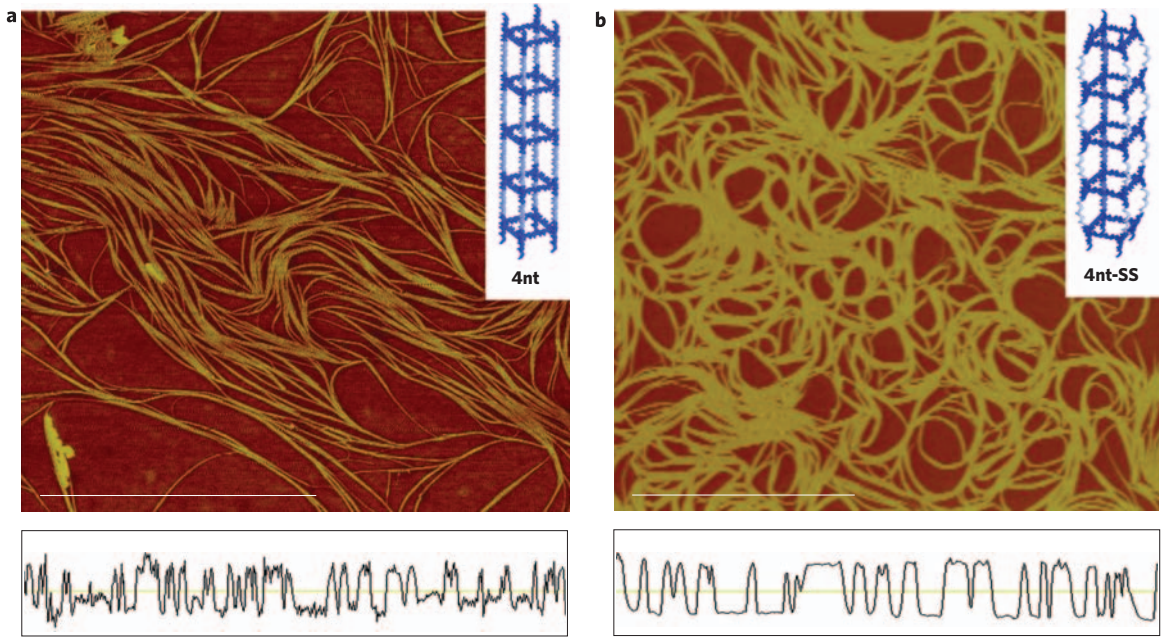

Figure 4 | AFM characterization of square DNA nanotubes that can be double- or single-stranded. a,**b**, The same well-defined square rung **4′** is used to generate fully double-stranded square DNA nanotube **4nt** assemblies using four double-stranded linking strands (**a**) and partially single-stranded DNA nanotube **4nt–ss** assemblies using one double-stranded linking strand and three single-stranded linking strands, which cross-sectional analysis (lower half of figure) shows to be of a uniform size (**b**). Scale bar, 2.5 μm.

to generate 'rungs' of well-defined geometries, and assembles these units longitudinally to produce nanotubes with pre-designed structures. Triangular and square DNA nanotubes can be readily accessed in their single-stranded and double-stranded forms. These assemblies are highly uniform, both longitudinally and laterally. Numerous applications for these nanostructures can be envisaged, such as the growth of metallic or semiconductor nanowires of tunable size and geometry, encapsulation of proteins or nanoparticles in their double-stranded form and possible release in their single-stranded form, and as interconnects with switchable persistence lengths.

Received 4 November 2008; accepted 5 March 2009; published online 12 April 2009

References

1. Yan, H., Park, S. H., Finkelstein, G., Reif, J. H. & LaBean, T. H. DNA-templated self-assembly of protein arrays and highly conductive nanowires. *Science* **301,** 1882–1884 (2003).
2. Douglas, S. M., Chou, J. J. & Shih, W. M. DNA-nanotube-induced alignment of membrane proteins for NMR structure determination. *Proc. Natl Acad. Sci. USA* **104,** 6644–6648 (2007).
3. Geng, Y. *et al.* Shape effects of filaments versus spherical particles in flow and drug delivery. *Nature Nanotech.* **2,** 249–255 (2007).
4. Rothemund, P. W. K. *et al.* Design and characterization of programmable DNA nanotubes. *J. Am. Chem. Soc.* **126,** 16344–16352 (2004).
5. Mitchell, J. C., Harris, J. R., Malo, J., Bath, J. & Turberfield, A. J. Self-assembly of chiral DNA nanotubes. *J. Am. Chem. Soc.* **126,** 16342–16343 (2004).
6. Sherman, W. B. & Seeman, N. C. Design of minimally strained nucleic acid nanotubes. *Biophys. J.* **90,** 4546–4557 (2006).
7. Endo, M., Seeman, C. & Majima, T. DNA tube structures controlled by a four-way-branched DNA connector. *Angew. Chem. Int. Ed.* **44,** 6074–6077 (2005).
8. Park, S. H. *et al.* Three-helix bundle DNA tiles self-assemble into 2D lattice or 1D templates for silver nanowires. *Nano Lett.* **5,** 693–696 (2005)
9. Liu, D., Park, S. H., Reif, J. H. & LaBean, T. H. DNA nanotubes self-assembled from triple-crossover tiles as templates for conductive nanowires. *Proc. Natl Acad. Sci. USA* **101,** 717–722 (2004).
10. Mathieu, F. *et al.* Six-helix bundles designed from DNA. *Nano Lett.* **5,** 661–665 (2005).
11. Kuzuya, A., Wang, R., Sha, R. & Seeman, N. C. Six-helix and eight-helix DNA nanotubes assembled from half-tubes. *Nano Lett.* **7,** 1757–1763 (2007).
12. Aldaye, F. A. & Sleiman, H. F. Sequential self-assembly of a DNA hexagon as a template for the organization of gold nanoparticles. *Angew. Chem. Int. Ed.* **118,** 2204–2209 (2006).
13. Aldaye, F. A. & Sleiman, H. F. Dynamic DNA templates for discrete gold nanoparticle assemblies: Control of geometry, modularity, write/erase and structural switching. *J. Am. Chem. Soc.* **129,** 4130–4131 (2007).
14. Aldaye, F. A. & Sleiman, H. F. Modular access to structurally switchable 3D discrete DNA assemblies. *J. Am. Chem. Soc.* **129,** 13376–13377 (2007).
15. Aldaye, F. A., Palmer, A. L. & Sleiman, H. F. Assembling materials with DNA as the guide. *Science* **321,** 1795–1799 (2008).

Acknowledgements

The authors would like to thank the Natural Sciences and Engineering Research Council of Canada, the Canada Foundation for Innovation, the Centre for Self-Assembled Chemical Structures, and the Canadian Institute for Advanced Research for financial support, A.L. Palmer for help in manuscript preparation, and J. Hedberg for help in preparing the graphical illustrations. F.A.A is a McGill University Principal's Prize Fellow. P.K.L. and P.K. thank CIHR for a Chemical Biology Scholarship. H.F.S is a Cottrell Scholar of the Research Corporation.

Author contributions

All authors discussed the results and commented on the manuscript. H.F.S. conceived and designed the project, analysed the data and co-wrote the paper. F.A.A conceived and designed the project, performed the experiments, analysed the data and co-wrote the paper. P.K.L performed the experiments and analysed the data. P.K. and G.C. performed the confocal fluorescence microscopy measurements. C.K.M. assisted in project design.

Additional information

Supplementary information accompanies this paper at www.nature.com/naturenanotechnology. Reprints and permission information is available online at http://npg.nature.com/reprintsandpermissions/. Correspondence and requests for materials should be addressed to H.F.S.

nature nanotechnology

LETTERS

PUBLISHED ONLINE: 26 APRIL 2009 | DOI: 10.1038/NNANO.2009.90

Ultrafast permeation of water through protein-based membranes

Xinsheng Peng[1], Jian Jin[1], Yoshimichi Nakamura[2], Takahisa Ohno[2,3] and Izumi Ichinose[1,3]*

Pressure-driven filtration by porous membranes is widely used in the production of drinking water from ground and surface water[1–3]. Permeation theory predicts that filtration rate is proportional to the pressure difference across the filtration membrane and inversely proportional to the thickness of the membrane[4]. However, these membranes need to be able to withstand high water fluxes and pressures, which means that the active separation layers in commercial filtration systems typically have a thickness of a few tens to several hundreds of nanometres[5]. Filtration performance might be improved by the use of ultrathin porous silicon membranes[6] or carbon nanotubes immobilized in silicon nitride[7] or polymer films[8,9], but these structures are difficult to fabricate. Here, we report a new type of filtration membrane made of crosslinked proteins that are mechanically robust and contain channels with diameters of less than 2.2 nm. We find that a 60-nm-thick membrane can concentrate aqueous dyes from fluxes up to 9,000 l h^{-1} m^{-2} bar^{-1}, which is ~1,000 times higher than the fluxes that can be withstood by commercial filtration membranes with similar rejection properties[1,10,11]. Based on these results and molecular dynamics simulations, we propose that protein-surrounded channels with effective lengths of less than 5.8 nm can separate dye molecules while allowing the ultrafast permeation of water at applied pressures of less than 1 bar.

Ultrafiltration membranes that reject particles and macromolecules of 2–100 nm in size are used for water purification, blood dialysis and food processing. They are generally made by phase inversion of polymer solutions or through the phase separation of polymer blends[1,2]. Reverse osmosis membranes are used for the production of drinking water from seawater and to concentrate milk, sugars, fruit juice and other products in the food industry. They are usually prepared by interfacial polymerization and often used in combination with ultrafiltration membranes[2,4]. Nanofiltration membranes have similarities with both ultrafiltration membranes and reverse osmosis membranes in that they can block multivalent ions and small organics, which is useful for water softening, the removal of micropollutants, and the recovery of dyes from waste water. Nanofiltration membranes are usually prepared either by interfacial polymerization or phase inversion[12].

Our membranes are based on proteins (usually ferritin), and are made using a process that relies on the properties of metal hydroxide nanostrands (Fig. 1). These nanostrands—which are ~2 nm wide and have surfaces that are highly positively charged[13–17]—spontaneously form in an aqueous solution of cadmium (or copper or zinc) nitrate and can assemble proteins into nanofibres. The nanofibres are then filtered off, leaving behind an ultrathin protein membrane on a porous substrate. This membrane is then converted into a robust free-standing separation membrane (Fig. 1b) by crosslinking with glutaraldehyde (see Methods and Supplementary Information).

Ferritin is a globular protein with a diameter of 12 nm, and our ferritin-based membranes typically have a thickness of 30–100 nm. Moreover, the membranes are uniform enough to be used for molecular filtration. Fourier transform infrared (FT-IR) and magnetic susceptibility analyses confirmed that the membranes were composed of undeformed crosslinked proteins and contained large numbers of nanoscale voids between the proteins. The membranes were stable in water in the pH range 1.5–13.0 and also in organic solvents such as chloroform, and had a hardness of 320 MPa and Young's modulus of 4.4 GPa according to nanoindentation measurements (see Supplementary Information).

A porous alumina filter with a 60-nm protein membrane was placed in a filtration cell (Fig. 1a) and protoporphyrin solution was suction filtered. When the pressure difference was 90 kPa, 35 ml of water permeated in 10 min and the feed volume decreased from 40 to ~5 ml. Ultraviolet–visible absorption measurements showed that the absorbance at 375 nm increased quasi-linearly with filtration time (Fig. 2a), and that the dye concentration increased by a factor of ~9–10 compared with the original solution, the protoporphyrin not being detected in the permeate. This indicates that water passed through the membrane and that the dye was completely rejected.

Protoporphyrin has a molecular width of 1.5 nm, which suggests that the diameters of the pores in the membrane are less than 1.5 nm. However, the isoelectric point of ferritin is in the range pH 4.5–4.8, so the electrostatic repulsion between the protoporphyrin and the protein membrane (both are negatively charged) may play a partial role in the rejection. To explore this further we examined the pore size by using neutral molecules (mono-tosylated cyclodextrins). When a 1 mM solution was filtered with a 60-nm-thick membrane, 4% of the α-cyclodextrin derivative, 23% of the β-cyclodextrin derivative and 51% of the γ-cyclodextrin derivative were rejected. When estimating the pore size we also need to consider conformational effects, which can reduce the size of the molecules, and hydration effects, which can increase their size. We can explore the conformational effects—which can reduce the size of the γ-cyclodextrin molecules from ~1.7 nm to less than 1.2 nm (see Supplementary Information and refs 18, 19)—by measuring the permeability in the presence of 1-adamantanol, which is known to form stable host–guest complexes with cyclodextrins. This caused the rejection of β- and γ-derivatives to increase to 85 and 89%, respectively. After considering the thickness of the possible hydration layer of 0.5 nm, we estimate that the average pore size is ~1.7 nm, with an upper limit of ~2.2 nm.

The flux in these experiments (as calculated from the valid area of the substrate) was surprisingly high: 5,400 l h^{-1} m^{-2} for the protoporphyrin solution at a pressure difference of 90 kPa, and 8,100 ± 50 l h^{-1} m^{-2} for pure water at the same pressure difference (which is equivalent to a pressure-normalized flux of 9,000 l h^{-1} m^{-2} bar^{-1}). The water flux was inversely proportional

[1]Organic Nanomaterials Center, National Institute for Materials Science, 1-1 Namiki, Tsukuba 305-0044, Japan, [2]Computational Materials Science Center, National Institute for Materials Science, 1-2-1 Sengen, Tsukuba 305-0047, Japan, [3]JST, CREST, 5 Sanbancho, Chiyoda-ku, Tokyo 102-0075, Japan.
*e-mail: ICHINOSE.Izumi@nims.go.jp

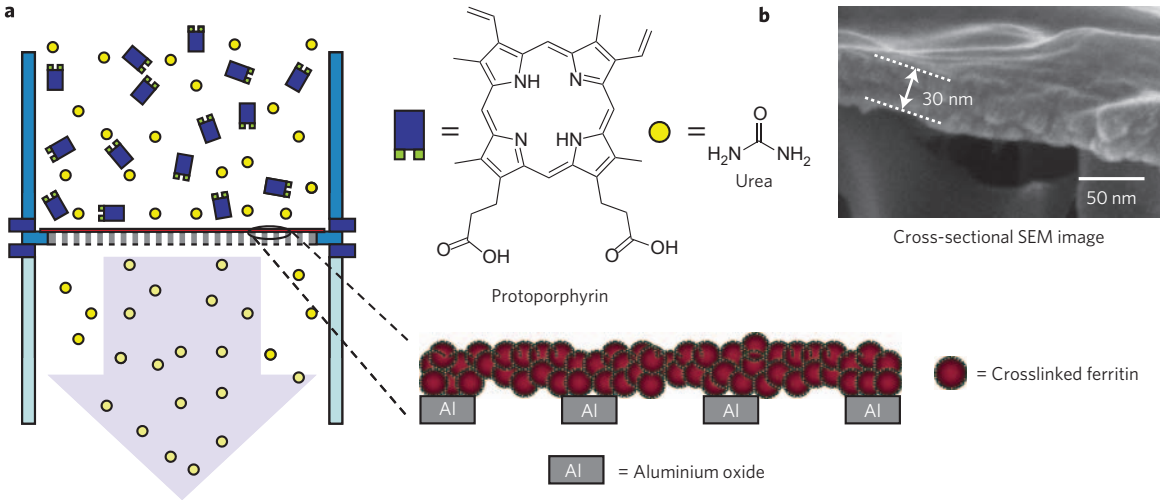

Figure 1 | Filtration of protoporphyrin by protein-based membrane. a, Schematic showing how a ferritin-based membrane on a porous alumina filter can reject large protoporphyrin molecules, while allowing small urea molecules to pass through. **b**, Cross-sectional scanning electron micrograph (SEM) showing that the membrane is ~30 nm thick. A 2-nm layer of platinum is included to prevent electric charging.

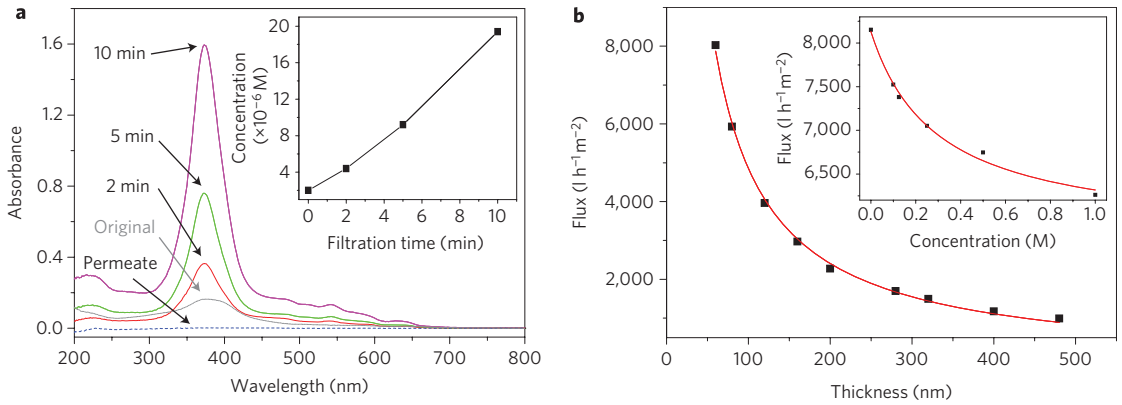

Figure 2 | Rejection of protoporphyrin and thickness-dependent water permeability. a, Ultraviolet–visible absorption changes of an aqueous solution of protoporphyrin (M_W, 562.7) showing complete rejection by a 60-nm-thick protein membrane. The original concentration was 2×10^{-6} M, and the valid area of the porous alumina support was 0.39 cm^2 (porosity, 50%). The filtration rate was calculated to be 5,400 l h^{-1} m^{-2} from the filtration volume (35 ml) and time (10 min). The pressure difference was 90 kPa. The inset shows the change in concentration (calculated from the increases in absorbance) of the protoporphyrin with filtration time. **b**, Thickness-dependent changes in permeability of pure water. Flux was determined by using polycarbonate membranes with a valid area of 0.22[7] cm^2 (porosity, 10%) at 90 kPa. The inset shows how the permeability of water changes with concentration of NaCl. These data were obtained using 60-nm-thick membranes.

to the thickness of the protein membranes (Fig. 2b) and increased linearly with pressure in the range 20–90 kPa. These results are consistent with the theoretical models of liquid/gas permeation through porous membranes. As shown in the inset of Fig. 2b, water flux decreased with increasing concentration of sodium chloride. When a 1 M solution was used, the flux dropped to 6,260 l h^{-1} m^{-2}. The hydrated diameters of these ions (0.72 nm for Na^+ and 0.66 nm for Cl^-) are much smaller than the hydrodynamic pore size of the membrane[20]. The viscosity of the water barely changes with salt concentration. It appears, then, that the flux is decreased by a constriction of pore size due to electrostatic shielding of the negatively charged amino residues of ferritin by sodium chloride.

Why do protein membranes allow ultrafast permeation of water? Water flowing through pores wider than 2 nm is often treated as a continuous fluid[21]. However, the estimated pore size (1.7–2.2 nm) in our membranes means that we need to confirm that the water in our experiments can indeed be treated as a continuous fluid. First, we used molecular dynamics simulations to model water molecules in an open pore with a diameter of 1.76 nm and a length of 1.84 nm: these simulations gave a density of 0.86 ± 0.03 g cm^{-3} and a self-diffusion constant very close to that of bulk water at 300 K and at 1 atm. It has been reported that water confined in a carbon nanotube of 1.36 nm diameter tends to form ordered structures[22]. In contrast, water viscosity μ in an open pore with a diameter of a few nanometres should be very close to the bulk value (8.9×10^{-4} Pa s). Based on the simulation results, we analysed the flux of water by using the Hagen–Poiseuille equation ($J = \varepsilon \pi r_p^2 \Delta p / 8\ \mu L$) (ref. 4). In this equation, the flux J is described as a function of the surface porosity ε, the pore radius r_p (1.1 nm), the pressure drop Δp (90 kPa), and the total distance L travelled by the water as it passes through the membrane. When globular ferritin units are two-dimensionally arranged in a closely packed fashion, the surface porosity is estimated to be 9.4%. The surface porosity should be no more than the water content of the hydrated membrane (27%, determined by the differential scanning calorimetry (DSC) method: see Methods). When the ε value was assumed to be 27% and L was assumed to be equal to the thickness of the protein membrane, the flux predicted for a 60-nm-thick

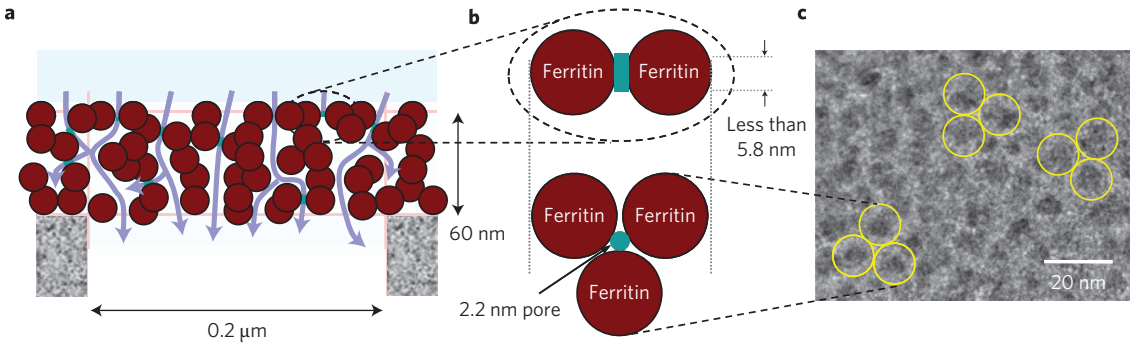

Figure 3 | Water permeation through protein-surrounded channels. a, A cross-sectional representation of a protein membrane on a porous alumina support. The scale of the ferritin is 1.5 times larger than that of the rest of the drawing. **b**, Side and top views of a protein-surrounded channel. Ultrafast water permeation is made possible by the presence of a large number of channels with effective lengths of less than 5.8 nm. **c**, A TEM image of a thin protein membrane. Some ferritin units are marked with yellow circles (which have diameters of 12 nm).

Table 1 | Separation performance of 60-nm-thick protein membranes for neutral and ionic compounds.

	MW (size/nm)	Concentration	pH	Membrane charge	Analyte charge	Flux (l h^{-1} m^{-2})	Rejection (%)
α-CD-Ts	1,127.0 (dia. 1.4)	1.0 mM	6.8	−	N	6,850	4
β-CD-Ts	1,289.2 (dia. 1.5)	Saturated	6.7	−	N	6,660	23
γ-CD-Ts	1,451.3 (dia. 1.7)	1.0 mM	6.6	−	N	6,580	51
β-CD-Ts/Ad	1,289.2 (dia. 1.5)	0.74/0.9 mM	6.7	−	N	6,250	85
γ-CD-Ts/Ad	1,451.3 (dia. 1.7)	0.67/3.3 mM	6.6	−	N	6,100	89
$[Fe(CN)_6]^{3-}$	212.0 (0.9 × 0.9)	1.0 mM	6.3	−	−	7,610	0.4
ANTS	381.4 (1.0 × 1.3)	40 μM	1.5	+	−	7,390	1.2
			6.3	−	−	7,690	0.1
			13.3	−	−	9,230	0.3
DY	864.9 (1.2 × 3.1)	10 μM	1.7	+	−	5,390	99.4
			2.7	+	−	5,400	99.2
			3.2	+	−	5,380	98.9
			3.8	+	−	5,420	74.9
			4.3	N	−	6,140	74.6
			6.2	−	−	6,230	66.5
			7.1	−	−	7,280	0.7
			9.5	−	−	7,290	0.5
			12.1	−	−	8,120	0.9
			13.0	−	−	8,860	0.1
PC/Cu	892.3 (1.7 × 1.7)	2.0 μM	1.4	+	+	6,400	99.9
			6.7	−	+	7,020	99.8
			13.0	−	+	8,390	99.9
DY/(PC/Cu)	864.9/892.3	10/2.0 μM	6.4	−	− / −	6,300	56.5/99.5
			13.1	−	− / −	8,070	0.5/99.9
TMPyP	678.8 (1.7 × 1.7)	1.5 μM	6.3	−	+	6,400	99.8
Cyt.c	12,400	2.0 mg ml^{-1}	11.0	−	−	6,590	99.9
PSS	70,000	0.1 mg ml^{-1}	6.7	−	−	1,540	2.9

α-CD-Ts, mono-6-O-(toluenesulphonyl)-α-cyclodextrin. β-CD-Ts, mono-2-O-(toluenesulphonyl)-β-cyclodextrin. γ-CD-Ts, mono-6-O-(toluenesulphonyl)-γ-cyclodextrin. Ad, 1-adamantanol. The sizes of cyclodextrin derivatives represent the outer diameter of cyclodextrin moieties in their expanded conformation[19]. The solubility of β-CD-Ts is ~0.8 mM. ANTS, 8-aminonaphthalene-1,3,6-trisulphonate. DY, Direct Yellow 50. PC/Cu, copper (II) phthalocyanine-tetrasulphonate. TMPyP, 5,10,15,20-tetrakis(*N*-methyl-pyridinium-4-yl)porphyrin. Molecular weights of ferricyanide and dyes do not contain their counter ions (potassium and sodium ions, p-toluenesulphonate). Cyt.c, cytochrome *c* (size: 2.5 × 2.5 × 3.7 nm^3). PSS, poly(styrenesulphonate) sodium salt. N, neutral charge. Filtration experiments were conducted on a porous alumina support at 90 kPa. pH was adjusted with HCl and NaOH. Molecular sizes of ferricyanide ion and dyes were calculated by using Spartan'04.

membrane was calculated to be 778 l h^{-1} m^{-2}, which is about 10 times smaller than the experimental value of the flux (8,100 l h^{-1} m^{-2}). Such a high value of the flux suggests that the water in these experiments has extremely low viscosity, but we see no evidence for this in our simulations.

We propose a very short protein-surrounded channel (Fig. 3) as the most plausible model to solely determine the overall flow rate of the water. The membrane had an irregular but closely packed structure of ferritin, as confirmed by cross-sectional scanning electron microscopy (SEM) observation of a freeze-fractured specimen (see Supplementary Information). Figure 3c presents a top-view transmission electron microscopy (TEM) image of the membrane, which shows that the ferritin cores were quasi-hexagonally packed at a certain distance from one another (Fig. 3c). When a round pore exists in a space surrounded by three globular proteins of diameter 12 nm, the diameter of the pore is geometrically calculated to be 1.8 nm (Fig. 3b). The pore also probably expands by a small amount to leave a hydrodynamic flow path of no more than 2.2 nm in diameter and of no more than 5.8 nm in length (as calculated from the observed flux of 8,100 l h^{-1} m^{-2}). It might seem strange that this tiny pore allows an extremely fast flow of water, because water is thought to strongly interact with the hydrophilic surfaces of protein. Whereas our experiments indicate that the water molecules very close to the protein surface behave like bulk water, we should not deny the possibility of there being extremely low friction resistance in the short channel to the permeation of water.

The separation performance of ionic compounds is summarized in Table 1. Small ions such as ferricyanide ($[Fe(CN)_6]^{3-}$) and

sulphonated naphthalene (ANTS) could freely pass through the channel. The flux of ANTS solutions increased to 9,230 l h^{-1} m^{-2} at pH 13.3, indicating that the pore size is enlarged at high pH. Direct Yellow, an elongated dye molecule, could not pass through the channel constricted at low pH, but it could freely permeate the channel at high pH. At pH 3.8 or lower, this molecule probably weakly adsorbs to the membrane, because the flux considerably decreased. The low rejection at high pH is due to the channel being enlarged. The membrane is negatively charged at both pH 6.2 and 13.0, but the flux increased at high pH. The constriction and expansion of the protein-surrounded channel were separately verified by using acid and base solutions free from these dyes. The size increased by 5% at pH 13.0 and decreased by 5% at pH 2.0 from the size at pH 7.0, as calculated from the changes of flux, assuming no change in the channel length. PC/Cu, a square-planar dye, was completely rejected at any pH, even though the molecular weight was close to that of Direct Yellow. TMPyP, a positively charged square-planar dye, was also rejected completely. At the concentrations of dyes examined (1.5–40 μM), the Debye length must be much longer than the diameter of the protein-surrounded channel. Although we could not observe a significant effect of membrane charge on the rejection, the effect remains to be seen.

From the data listed in Table 1, it is clear that rejection is very sensitive to the shape of molecules. This can be extended to the conformation of macromolecules. For example, an aqueous solution of poly(styrenesulphonate) (PSS), a linear polyelectrolyte, could permeate the membrane at a flow rate of 1,540 l h^{-1} m^{-2}, giving a rejection of 3%. The molecular weight of this polymer (M_W, 70,000) is more than a hundred times higher than that of protoporphyrin. The fast transmission of polyelectrolytes resembles RNA transport through a nuclear envelope[23]. Recently, it was reported that supercoiled plasmid DNA could pass through ultrafiltration membranes with pores of ~10 nm diameter when water flux increased to a certain threshold[24]. Transmission of PSS through protein membranes must be as a result of the fast permeation of water. Protein-based membranes could be obtained by using other proteins such as cytochrome *c*, myoglobin, glucose oxidase and apoferritin. However, water permeability of these membranes was not as high as ferritin-based membranes.

Ultrafiltration membranes of S-layer proteins were reported by Sára and Sleytr more than 20 years ago[25]. However, the water flux was in the range 85–200 l h^{-1} m^{-2} bar^{-1}, even though the molecular weight cut-off was rather high (30–45 kDa). The water flux through our protein membranes (9,000 l h^{-1} m^{-2} bar^{-1}) is much faster than this and is two to three orders of magnitude faster than those of commercial nano- or ultrafiltration membranes with molecular weight cut-offs of 1–3 kDa. Moreover, it should be possible to make further improvements in performance by designing the structure of the separation layer at the nanoscale, which could lead to applications in water purification and other areas of science and technology.

Methods

Preparation of protein-based membranes. The following are typical preparation procedures. An aqueous solution of 0.8 mM 2-aminoethanol was mixed with an equivolume of 4 mM cadmium nitrate and allowed to stand for 10 min to give cadmium hydroxide nanostrands. Then, 1 ml of ferritin solution (horse spleen, 3.8 mg ml^{-1}) was mixed to the above nanostrand solution (20 ml) and stirred for 30 min. The resultant brown-coloured transparent solution was filtered on a polycarbonate membrane filter with pores of 0.2 μm. The thickness of the filter cake could be tuned in the range 25–4,000 nm by choosing the volume of the solution to be filtered. Subsequently, the membrane filter was immersed in an aqueous solution of glutaraldehyde (10 wt%) for 1 h. The crosslinked ferritin layer was readily peeled off by immersing the membrane filter in ethanol. The protein membrane was then immersed in an aqueous solution of hydrogen chloride (10 mM) for a few hours to remove cadmium hydroxide nanostrands and rinsed in water. Pinhole-free protein-based membranes were obtainable by this flux-driven production process.

Characterization of the membrane. SEM and TEM images were obtained using a Hitachi S-4800 and a JEOL JEM-2100F units, respectively. TEM observations were conducted at an acceleration voltage of 200 kV. Details for the preparation and characterization of protein-based membranes are described in Supplementary Figs S1, S2 and S7, which also include EDX and FT-IR analyses. The mechanical properties were analysed using a Hysitron TriboIndenter and a Berkovich diamond indenter (see Supplementary Fig. S3). The water content of the hydrated membrane was estimated using a DSC method. In brief, a wet protein membrane was quickly wiped with tissue, sealed in a silver container, and subjected to the measurements. The thermograms were obtained on a SII Nanotechnology EXSTAR 6000 with a measurement range of ±100 mW. The enthalpy change observed near 0 °C was used for the calculation of water content. DSC thermogram and water permeability data at different pressures are shown in Supplementary Fig. S4. The structure and sizes of the dye molecules and the rejection of cyclodextrin derivatives are also explained in Supplementary Fig. S5.

Molecular dynamics simulation. For the geometric model of a short protein-surrounded channel, a 416-carbon (13,13) nanotube (carbon–carbon bond length of 1.4 Å) was used (see Supplementary Fig. S6). A model pore 1.84 nm in length and 1.76 nm in diameter was solvated with 2170 TIP5P water molecules in a periodic box[26]. Molecular dynamics simulations were performed using AMBER 9.0 (ref. 27) (University of California at San Francisco). The water and the model pore were assumed to interact with each other only through the 6–12 Lennard–Jones potential between the oxygen atom and the sp^2 carbon atom. The values of the two potential parameters, the cross-section $\sigma_{CO} = 3.260$ Å and the depth of the potential well $\varepsilon_{CO} = 0.117$ kcal mol^{-1}, were obtained by the Lorentz–Berthelot combining rules. Long-range electrostatic Coulomb interaction between the water molecules was calculated by the particle-mesh Ewald method[28]. The molecular dynamics time step was set to 2 fs. In the first runs of 2.5×10^5 steps (0.5 ns), a combination of constant volume equilibration and constant pressure equilibration was performed to ensure the system was in equilibration with the water density of 1.0 g cm^{-3} at 300 K. The subsequent 1×10^6 steps (2 ns) in the NVT-ensemble were used for statistical analysis. Snapshots were saved every 0.1 ps for analysis. (A movie showing the motion of the water molecules in a model pore is available in the Supplementary Information.)

Received 6 February 2009; accepted 23 March 2009; published online 26 April 2009

References

1. Vankelecom, I. F. J., De Smet, K., Gevers, L. E. M. & Jacobs, P. A. Nanofiltration membrane materials and preparation, in *Nanofiltration: Principles and Applications* (eds Schäfer, A. I., Fane, A. G. & Waite, T. D.) ch. 3 (Elsevier, 2005).
2. Petersen, R. J. Composite reverse osmosis and nanofiltration membranes. *J. Membrane Sci.* **83,** 81–150 (1993).
3. Shannon, M. A. *et al.* Science and technology for water purification in the coming decades. *Nature* **452,** 301–310 (2008).
4. Baker, R. W. *Membrane Technology and Applications* 2nd edn (Wiley, 2004).
5. Vandezande, P., Gevers, L. E. M. & Vankelecom, I. F. J. Solvent resistant nanofiltration: separating on a molecular level. *Chem. Soc. Rev.* **37,** 365–405 (2008).
6. Striemer, C. C., Gaborski, T. R., McGrath, J. L. & Fauchet, P. M. Charge- and size-based separation of macromolecules using ultrathin silicon membranes. *Nature* **445,** 749–753 (2007).
7. Holt, J. K., Noy, A., Huser, T., Eaglesham, D. & Bakajin, O. Fabrication of a carbon nanotube-embedded silicon nitride membrane for studies of nanometer-scale mass transport. *Nano Lett.* **4,** 2245–2250 (2004).
8. Hinds, B. J. *et al.* Aligned multiwalled carbon nanotube membranes. *Science* **303,** 62–65 (2004).
9. Holt, J. K. *et al.* Fast mass transport through sub-2-nanometer carbon nanotubes. *Science* **312,** 1034–1037 (2006).
10. Lu, Y., Suzuki, T., Zhang, W., Moore, J. S. & Mariñas, B. J. Nanofiltration membranes based on rigid star amphiphiles. *Chem. Mater.* **19,** 3194–3204 (2007).
11. Braeken, L., Van der Bruggen, B. & Vandecasteele, C. Flux decline in nanofiltration due to adsorption of dissolved organic compounds: model prediction of time dependency. *J. Phys. Chem. B* **110,** 2957–2962 (2006).
12. Khulbe, K. C., Feng, C. Y. & Matsuura, T. *Synthetic Polymeric Membranes: Characterization by Atomic Force Microscopy* (Springer, 2008).
13. Peng, X., Jin, J., Ericsson, E. M. & Ichinose, I. General method for ultrathin free-standing films of nanofibrous composite materials. *J. Am. Chem. Soc.* **129,** 8625–8633 (2007).
14. Ichinose, I., Kurashima, K. & Kunitake, T. Spontaneous formation of cadmium hydroxide nanostrands in water. *J. Am. Chem. Soc.* **126,** 7162–7163 (2004).
15. Luo, Y. *et al.* Formation of positively charged copper hydroxide nanostrands and their structural characterization. *Chem. Mater.* **18,** 1795–1802 (2006).
16. Peng, X., Jin, J., Kobayashi, N., Schmitt, W. & Ichinose, I. Time-dependent growth of zinc hydroxide nanostrands and their crystal structure. *Chem. Commun.* 1904–1906 (2008).
17. Peng, X., Jin, J. & Ichinose, I. Mesoporous separation membranes of polymer-coated copper hydroxide nanostrands. *Adv. Funct. Mater.* **17,** 1849–1855 (2007).

18. Connors, K. A. The stability of cyclodextrin complexes in solution. *Chem. Rev.* **97,** 1325–1357 (1997).
19. Szejtli, J. Introduction and general overview of cyclodextrin chemistry. *Chem. Rev.* **98,** 1743–1753 (1998).
20. Conway, B. E. *Ionic Hydration in Chemistry and Biophysics* (Elsevier, 1981).
21. Verweij, H., Schillo, M. C. & Li, J. Fast mass transport through carbon nanotube membranes. *Small* **3,** 1996–2004 (2007).
22. Liu, Y., Wang, Q., Wu, T. & Zhang, L. Fluid structure and transport properties of water inside carbon nanotubes. *J. Phys. Chem.* **123,** 234701 (2005).
23. Rodriguez, M. S., Dargemont, C. & Stutz, F. Nuclear export of RNA. *Biol. Cell.* **96,** 639–655 (2004).
24. Latulippe, D. R., Ager, K. & Zydney, A. L. Flux-dependent transmission of supercoiled plasmid DNA through ultrafiltration membranes. *J. Membrane Sci.* **294,** 169–177 (2007).
25. Sára, M. & Sleytr, U. B. Production and characteristics of ultrafiltration membranes with uniform pores from two-dimensional arrays of proteins. *J. Membrane Sci.* **33,** 27–49 (1987).
26. Mahoney, M. W. & Jorgensen, W. L. A five-site model for liquid water and the reproduction of the density anomaly by rigid, nonpolarizable potential functions. *J. Chem. Phys.* **112,** 8910–8922 (2000).
27. Case, D. A. *et al. AMBER 9* (Univ. California, 2006).
28. Darden, T., York, D. & Pedersen, L. Particle mesh Ewald: An *N*·log (*N*) method for Ewald sums in large systems. *J. Chem. Phys.* **98,** 10089–10092 (1993).

Acknowledgements

The authors thank S. Nakao (Tokyo University) for many helpful discussions.

Author contributions

X.P. was responsible for the preparation and characterization of protein-based membranes, evaluation of filtration properties of dyes and other water-soluble compounds, and analysis of water permeability. Y.N. and T.O. were responsible for molecular dynamics simulations. J.J. contributed to the crosslinking of proteins. X.P. and I.I. were responsible for experimental design and manuscript preparation. I.I. was responsible for project planning.

Additional information

Supplementary information accompanies this paper at www.nature.com/naturenanotechnology. Reprints and permission information is available online at http://npg.nature.com/reprintsandpermissions/. Correspondence and requests for materials should be addressed to I.I.

nature nanotechnology

LETTERS

PUBLISHED ONLINE: 26 APRIL 2009 | DOI: 10.1038/NNANO.2009.91

Alternating patterns on single-walled carbon nanotubes

Bing Li, Lingyu Li, Bingbing Wang and Christopher Y. Li*

Scientific and technological interest in one-dimensional nanomaterials, in particular carbon nanotubes[1,2], is a result of their fascinating properties and their ability to serve as templates for directed assembly. For applications in nanoelectronics it is necessary to create ordered arrays of nanotubes for large-scale integrated circuits, an area in which there has been significant progress[3–7], and to produce controllable patterns on individual nanotubes so that multiple transistors can be fabricated on them, an area where progress has been slower[8–14]. Here, we show that judiciously selected crystalline block copolymers can be periodically decorated along carbon nanotubes, leading to amphiphilic, alternating patterns with a period of ~12 nm. In addition, end-functionalization of the block copolymers allowed gold nanoparticles to be periodically attached to the nanotubes. This approach provides a facile technique for the periodic patterning of one-dimensional nanomaterials.

The functionalization of carbon nanotubes is of great interest from both scientific and technological viewpoints[15]. Periodically functionalized carbon nanotubes can directly lead to the creation of controlled two- or three-dimensional carbon nanotube suprastructures, which is an essential step towards building future carbon nanotube-based nanodevices. Very few reports have addressed periodic functionalization/patterning on carbon nanotubes[10–13]. Regarding the patterning on the carbon nanotube surface, all the reported periodic patterns to date have suffered from limitations such as the locality of the pattern or poor periodicity. Here, we report the use of low-molecular-weight polyethylene-*b*-poly(ethylene oxide) (PE-*b*-PEO) block copolymer to obtain uniform, periodic patterns on carbon nanotubes. This unique hybrid structure holds promise for a variety of nanoelectronic and biomedical applications[16].

A single-walled carbon nanotube (SWNT)/dichlorobenzene solution was dropcast on a carbon-coated nickel grid and dried at ambient temperature. The fractionated PE-*b*-PEO (molecular weight 1,700 g mol^{-1}; 50 wt% PE) was dissolved in chloroform and the solution was then spincoated onto the SWNT-loaded grid. The sample was stained with ruthenium tetroxide (RuO_4) to enhance the contrast. Figure 1a shows a transmission electron microscopy (TEM) image of the resultant block copolymer/SWNT hybrid. Numerous elongated 'worm-like' structures with dark and bright stripes are clearly visible. Their average length is ~1 μm and their width ~50 nm. The stripes are phase-separated block copolymers; the dark stripes are PEO and the bright ones PE blocks. The inset of Fig. 1a shows an enlarged area. Because of their small size and the coverage of block copolymers, no carbon nanotubes can be clearly identified in the image. However, the consistent orientations of the adjacent stripes and the aspect ratio of this unique worm-like morphology indicate that the axes of the underlying SWNTs are perpendicular to the stripes, as shown in Fig. 1b. This can also be supported by our control experiment, in which block copolymer alone was spincoated on the carbon-coated grid. In such a case, random alternating stripes and/or lozenge-shaped single crystals were formed (see Supplementary Fig. S1).

Observing this regular pattern on carbon nanotubes at a scale of ~12 nm is intriguing and the formation of this structure is related to the interplay between block copolymer phase separation and carbon nanotube-induced polymer crystallization. Block copolymers are known to be able to phase separate into ordered microstructures at a scale of ~10–100 nm (refs 17–19). As they are dissolved in solvents, block copolymers can be considered as macromolecular surfactants[20,21]. In a carbon nanotube/block copolymer system, if one segment of the block copolymer is crystalline and is able to form single crystals on carbon nanotubes, the block copolymer phase separation and the carbon nanotube-induced crystallization should affect each other. Depending on the block copolymer/nanotube/solvent interaction parameters, a few scenarios are possible: (i) the block copolymers form micelles (or other aggregates), which separate from the carbon nanotubes; (ii) the block copolymers form micelles that wrap around the carbon nanotubes; and (iii) one segment of the block copolymer crystallizes on the carbon nanotubes, leading to nanotube-induced block copolymer phase separation. The morphology of the block copolymer/SWNT hybrid in Fig. 1 clearly indicates that the phase separation of PE-*b*-PEO is directed by the underlying SWNTs, suggesting that scenario (iii) is the dominant physical process in the present system. Note that there are some other possible mechanisms that might lead to the formation of similar structures. For instance, if both blocks of a block copolymer are neutral to the surface of a carbon nanotube, a similar phase-separated structure could be formed along the nanotube. Other researchers have also shown that topological pre-patterned lines could guide a block copolymer-containing hybrid material to form an orthogonally aligned lamellar phase[22]. To demonstrate the role of PE crystallization in the formation of the present hybrid structures, we further conducted two control experiments. In the first control experiment, PE-*b*-PEO was replaced by polybutadiene(1,4 rich)-*b*-poly(ethylene oxide) (PB-*b*-PEO). In the second, a thin layer of amorphous carbon was deposited onto the SWNTs before spincoating. In both cases, alternating block copolymer patterns were not observed on the SWNTs (see Supplementary Fig. S2). These control experiments clearly demonstrate that nanotube-induced PE crystallization is critical to the formation of the alternating patterns on the carbon nanotubes. Note also that solvent selectivity is critical to solution crystallization of crystalline block copolymers[20]. Our preliminary work showed that as the solvent was switched from chloroform to dimethylformamide (DMF) or water, uniform and dense stripes were not observed. DMF and water are more selective for PEO, so micelles become more stable in the solution. As a result, crystalline stripes are not formed upon solidification. Recently, our laboratory reported that

A. J. Drexel Nanotechnology Institute and Department of Materials Science and Engineering, Drexel University, Philadelphia, Pennsylvania 19104, USA.
*e-mail: chrisli@drexel.edu

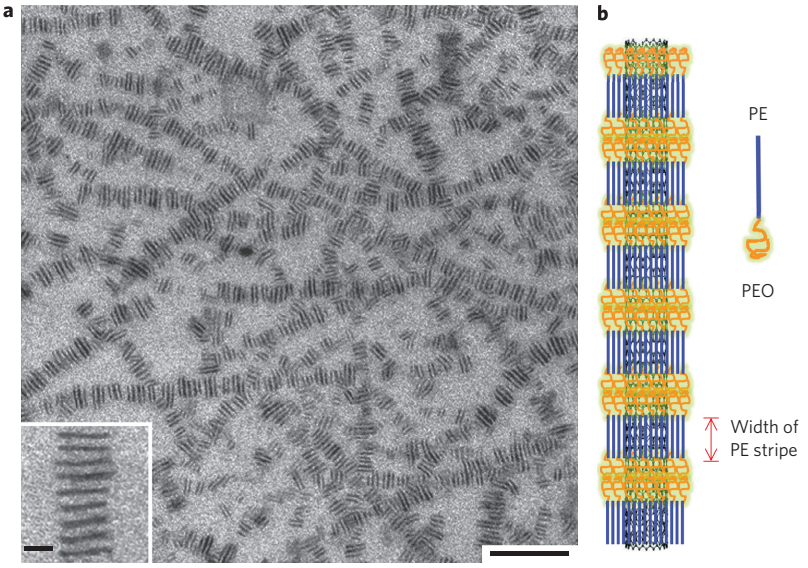

Figure 1 | The alternating pattern of PE-*b*-PEO block copolymers formed on SWNTs. a, TEM image of the PE-*b*-PEO decorated SWNTs. The dark and bright stripes are the PEO and PE domains, respectively. The formation of this unique structure is attributed to the subtle interplay between carbon nanotube-induced polymer crystallization and block copolymer phase separation (scale bar, 200 nm). The inset shows an enlarged area (scale bar, 20 nm). **b**, Schematic representation of the arrangement of the PE-*b*-PEO molecules along a SWNT.

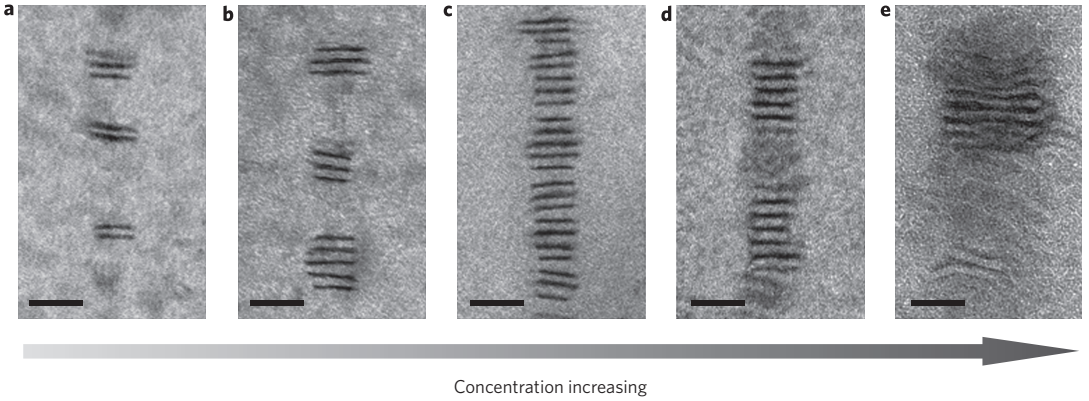

Figure 2 | TEM images of the five different morphologies of the block copolymer/SWNT hybrid at various block copolymer concentrations. **a**–**e**, TEM images for concentrations of the block copolymer solution of 0.001 wt% (**a**), 0.002 wt% (**b**), 0.005 wt% (**c**), 0.020 wt% (**d**), 0.050 wt% (**e**). Scale bars, 50 nm.

carbon nanotubes were able to induce polymer crystallization[23–25]. PE single crystals have been controlled to grow on carbon nanotubes, and the growth mechanism is size-dependent soft epitaxy. In the present block copolymer/SWNT hybrids, upon crystallization, PE chains aligned parallel to the SWNT axis, forming the bright stripes. The observed alternating stripes are thus perpendicular to the SWNT axes. Compared with the crystal patterns formed in carbon nanotube-induced homopolymer crystallization, the present alternating pattern formed by the block copolymer is far more uniform. In Fig. 1a, the period of the alternating pattern is 11.9 ± 0.9 nm. The width of the bright stripes along the carbon nanotube axes is 5.9 ± 0.7 nm. Comparing this number with the extended chain length of the PE block suggests that each PE domain is made of one layer of interdigitated extended PE chains. Note that sodium dodecyl sulphate (SDS)-wrapped carbon nanotubes have also been reported to have periodic patterns[12]. The formation mechanism in the SDS/carbon nanotube case was first attributed to the hemisphere micelles formed along the carbon nanotube. Molecular simulation conducted by others have shown, however, that the hydrophobic tail of SDS aligned parallel to the tube axis, forming multiple layers on the carbon nanotube surface[26]. The parallel packing of the SDS tails may resemble the crystallization of the PE segments in PE-*b*-PEO.

The block copolymer concentration around the SWNT has an important role in the formation of the alternating pattern. Figure 2 shows five different morphologies of block copolymer/SWNT hybrids formed at various block copolymer concentrations. At a relatively low block copolymer concentration, the SWNTs are decorated by discrete patches of stripes (Fig. 2a). There is no block copolymer present in the intervals between the adjacent patches. As the block copolymer concentration rises, the number of stripes in each patch increases (Fig. 2b). When the block copolymer concentration reaches a certain value, the intervals between patches are completely filled with stripes, and uniform, alternating stripes are found along the entire SWNTs (Fig. 2c). As the block copolymer concentration increases further, new 'intervals' seemingly appear along the tubes (Fig. 2d). These new intervals are made of block copolymers. The area looks greyish because the orientation of the phase-separated block copolymer is not uniform. As the concentration increases further, the lateral dimension of the patches increases dramatically (Fig. 2e).

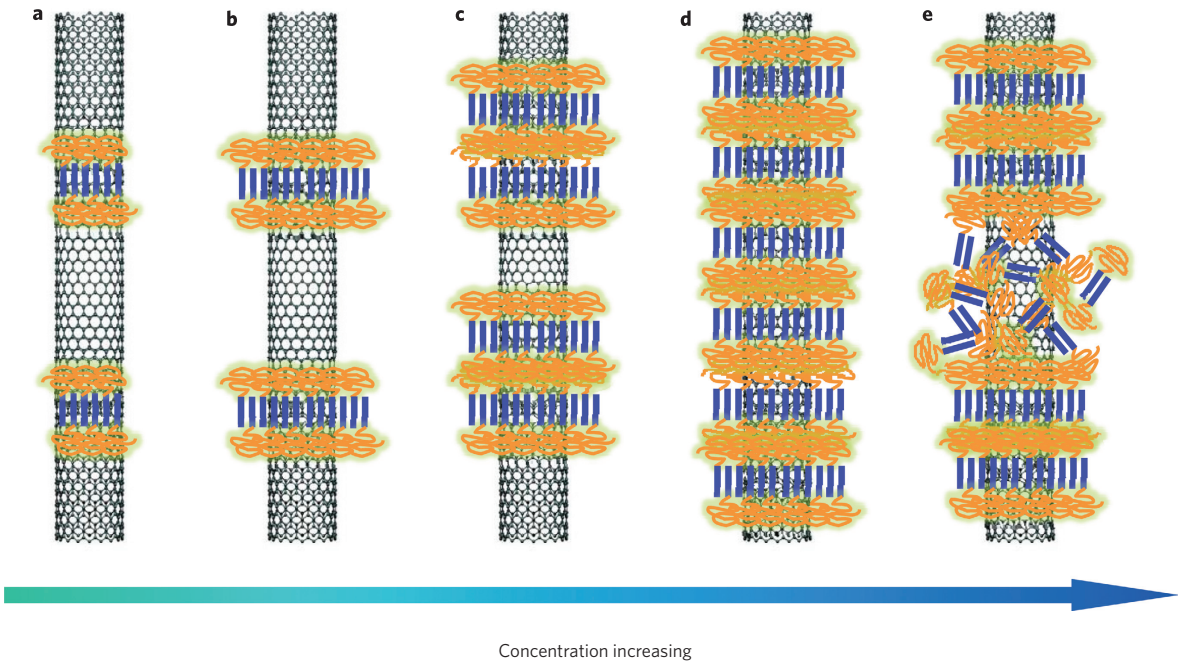

Figure 3 | Growth mechanism of the alternating stripes on a SWNT. a, Heterogeneous nucleation of the PE segments on a SWNT. **b**–**e**, The growth patterns of the stripes at various block copolymer concentrations, where concentration increases from **b** to **e**.

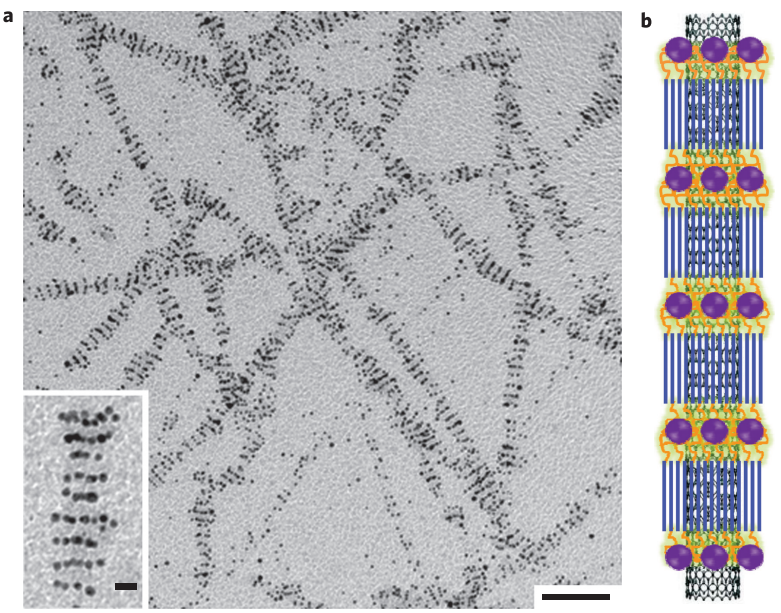

Figure 4 | Periodic immobilization of 5-nm gold nanoparticles on the block copolymer/SWNT hybrid. a, TEM image of the gold nanoparticle-decorated block copolymer/SWNT hybrid. The block copolymer is end-functionalized with a thiol group (scale bar, 100 nm). The inset shows an enlarged area (scale bar, 10 nm). **b**, Schematic representation of the arrangement of the gold nanoparticles and the block copolymer chains along an SWNT.

Based on the above observations, we propose a growth mechanism for the formation of the alternating stripes on SWNTs (Fig. 3). During spincoating, the block copolymer molecules randomly adsorb onto the SWNT surface due to the favourable interaction between the PE segments and the SWNTs, leading to heterogeneous nucleation (Fig. 3a). After the formation of a stable nucleus, the PE crystal starts to grow, following the soft epitaxy mechanism[23]. At an extremely low block copolymer concentration, the block copolymer molecules crystallize only to the initially formed nuclei. Because of the local concentration gradient generated at the crystal growth front, the stripes grow laterally on the carbon film with a perpendicular orientation to the tube axis (Fig. 3b). The above process is driven by carbon nanotube-induced PE crystallization. As the block copolymer concentration increases, more crystals start to appear. The tethered PEO chains at the crystal edges, dangling in the solution, attract PEO segments of the free block copolymer molecules to the adjacent region, and facilitate crystallization of the block copolymer at a certain distance away from the initially formed nuclei on the SWNT, where the distance depends on the length of the PEO block. This process is governed by the phase separation of the block copolymer. Repetition of the process leads to the formation of patches of alternating block

copolymer stripes along the SWNT (Fig. 3c). As the block copolymer concentration reaches a critical point, the patches are long enough to connect with each other, leading to continuous, alternating stripes spanning the entire SWNT (Fig. 3d). As the concentration further increases, there are so many block copolymer molecules depositing on the SWNTs that they do not have enough time and space to align themselves into a well-defined structure. As a result, the block copolymer molecules accumulated at the intervals do not show a clearly phase-separated pattern (Fig. 3e).

This uniformly patterned hybrid structure represents a unique nanoscale complex architecture that has not been achieved previously. Because PE is hydrophobic and PEO is hydrophilic, this system features a hybrid structure on individual carbon nanotubes that has alternating amphiphilicity with a ~12-nm period. The domain size can be controlled by changing the block copolymer molecular weight. Our preliminary data show that as the PE molecular weight decreased from 850 to 730 g mol^{-1} (the molecular weight of the PEO block ranging from 850 to 970 g mol^{-1}, respectively), the width of the bright stripes dropped from 5.9 ± 0.7 nm to 4.6 ± 0.7 nm. This structure is also similar to multicompartmental block copolymer structures, which can be used as a drug delivery system with the capability to deliver multiple drugs[27,28]. Furthermore, the PEO domains can be modified with various functional groups so that periodic functionalization of carbon nanotubes may be achieved. As a proof of concept, we synthesized thiol-terminated PE-*b*-PEO (see Supplementary Fig. S3). Following the same experimental procedure, SWNTs were periodically decorated by the block copolymer with thiol groups present in the PEO stripes (see Supplementary Fig. S4). The resultant product was then incubated with a gold colloid (5 nm in diameter). Figure 4a is a TEM image of the gold nanoparticle-decorated block copolymer/SWNT hybrid. The gold nanoparticles were patterned periodically along the SWNTs, with a period the same as that of the block copolymer/SWNT hybrid. This is because the thiol-terminated PEO stripes immobilized gold nanoparticles on their surface by means of sulphur–gold bonds, as shown in Fig. 4b (ref. 29). Note that the number of gold nanoparticles on each PEO stripe can be tuned by controlling the lateral dimension of the block copolymer stripes on the carbon nanotube surface. This periodic gold nanoparticle/SWNT hybrid is of great interest in various areas of nanoelectronics and single-electron devices.

In summary, we have produced nanoscale alternating patterns of block copolymer along SWNTs. The period of the patterns was ~12 nm along the SWNT axis. The mechanism of formation was attributed to the interplay of carbon nanotube-induced PE crystallization and the block copolymer phase separation. By end-functionalizing the block copolymer with a thiol group, gold nanoparticles were immobilized along the SWNTs, replicating the ordered block copolymer structure. This work therefore demonstrates a facile method to achieve periodic patterning on SWNTs, a key step towards using one-dimensional nanomaterials in nanodevice applications.

Methods

Materials. Purified HiPco SWNTs were purchased from Carbon Nanotechnologies. Dichlorobenzene (DCB), tetraoctylammonium bromide (TOAB), pentyl acetate, thioglycolic acid, sulphuric acid (98%), isopropyl ether, dichloromethane, 5-nm gold/water colloid, toluene and chloroform were purchased from Sigma-Aldrich and used as received. Polyethylene-*b*-poly(ethylene oxide) (PE-*b*-PEO) (molecular weight 1,400 g mol^{-1}, 50 wt% PE) was purchased from Sigma-Aldrich and was fractionated before usage. Polybutadiene(1,4 rich)-*b*-poly (ethylene oxide) (PB-*b*-PEO) (molecular weight 930–1,020 g mol^{-1}) was purchased from Polymer Source and used as received.

Instruments. The Branso Ultrasonic Cleaner was used for sonication. Spincoating was performed on the Specialty Coating Systems Spin Coater—G3P12. The Fisher Scientific Centrifuge Marathon 21000 was used as the centrifuge. TEM experiments were conducted on a JEOL 2000FX TEM with an accelerating voltage of 120 kV. The polydispersity index of PE-*b*-PEO was characterized by gel permeation chromatography (GPC) at 40 °C using tetrahydrofuran as the eluent at a flow rate of 1.0 ml min^{-1}. Data were collected by the Refractive Index Detector 2414 and analysed using the software provided by Waters. The calibration curve was constructed with narrowly distributed PEO standards. Proton nuclear magnetic resonance (^{1}H NMR) was measured on a Unityinova 500 MHz NMR spectrometer. The Fourier transform infrared (FTIR) spectra were obtained on a Varian Excalibur FTS-3000. Vacuum evaporation of carbon was conducted on a Polaron Range E6300 Vacuum Evaporator.

Fractionation of PE-*b*-PEO. PE-*b*-PEO (10 g) was dissolved in 50 ml dichloromethane and 100 ml isopropyl ether was added to the solution subsequently. The mixture was then placed in a vacuum chamber to gradually remove the solvents. The block copolymers with the highest PE percentage precipitated out first. The precipitated block copolymer was collected and labelled as fraction 1 to 6 in time order. Fraction 4 was chosen to be used in this research.

The GPC spectrum (see Supplementary Fig. S5) showed that the polydispersity index of the fractionated block copolymer was 1.15. From the end-group analysis using ^{1}H NMR (see Supplementary Fig. S6), the molecular weight was 1,700 g mol^{-1} and the PE block 50 wt%.

Crystallization of block copolymer on SWNTs. SWNTs (0.02 mg) were dissolved in 1.0 g DCB by means of sonication for 1 h. The SWNT/DCB solution was dropcast on the carbon-coated nickel grids and dried at ambient temperature. Block copolymer/chloroform solution was spincoated on the SWNT-loaded grids at 3,000 rpm for 30 s. The concentrations of the solutions varied from 0.001 to 0.050 wt%. The samples were stained by RuO_4 before TEM observation.

Preparation of amorphous carbon-coated SWNTs. The SWNT-loaded grids were placed in a vacuum evaporator. A layer of amorphous carbon was deposited on the SWNTs by thermally evaporated a small amount of carbon from a graphite rod.

Synthesis of thiol-terminated PE-*b*-PEO. The PEO segment of the fractionated block copolymer is terminated with a hydroxyl group. Thiol-terminated PE-*b*-PEO was synthesized by reacting the hydroxyl terminated PE-*b*-PEO with thioglycolic acid as described by Brash[30]. Briefly, a drop of sulphuric acid, 5 g of PE-*b*-PEO, and a stoichiometric amount of thioglycolic acid were added to 20 ml of toluene preheated to 80 °C. The reaction proceeded at 110 °C under nitrogen for 3 h and was driven forward by the continuous removal of the water produced. The modified polymer was purified by precipitation in isopropyl ether and subsequent dissolution in dichloromethane. This sequence was repeated three times. The reaction product was then dried under vacuum at ambient temperature for 2 days.

Preparation of 5-nm gold/pentyl acetate colloid. The detailed procedure can be found in ref. 29.

Immobilization of gold nanoparticles on a block copolymer/SWNT hybrid. Thiol-terminated PE-*b*-PEO/chloroform solution (0.005 wt%) was spincoated on a SWNT-loaded grid at 3,000 rpm for 30 s. The grid was then incubated with the 5-nm gold/pentyl acetate colloid for 1 h. The grid was rinsed with pentyl acetate and dried at ambient temperature.

Received 24 November 2008; accepted 23 March 2009; published online 26 April 2009

References

1. Dresselhaus, M. S., Dresselhaus, G. & Avouris, P. *Carbon Nanotubes: Synthesis, Structure, Properties and Applications* (Springer, 2001).
2. Baughman, R. H., Zakhidov, A. A. & de Heer, W. A. Carbon nanotubes—the route toward applications. *Science* **297,** 787–792 (2002).
3. Rao, S. G., Huang, L., Setyawan, W. & Hong, S. Large-scale assembly of carbon nanotubes. *Nature* **425,** 36–37 (2003).
4. Ahn, J. H. *et al.* Heterogeneous three-dimensional electronics by use of printed semiconductor nanomaterials. *Science* **314,** 1754–1757 (2006).
5. Kang, S. J. *et al.* High-performance electronics using dense, perfectly aligned arrays of single-walled carbon nanotubes. *Nature Nanotech.* **2,** 230–236 (2007).
6. Li, X. L. *et al.* Langmuir–Blodgett assembly of densely aligned single-walled carbon nanotubes from bulk materials. *J. Am. Chem. Soc.* **129,** 4890–4891 (2007).
7. LeMieux, M. C. *et al.* Self-sorted, aligned nanotube networks for thin-film transistors. *Science* **321,** 101–104 (2008).
8. Bachtold, A., Hadley, P., Nakanishi, T. & Dekker, C. Logic circuits with carbon nanotube transistors. *Science* **294,** 1317–1320 (2001).
9. Keren, K., Berman, R. S., Buchstab, E., Sivan, U. & Braun, E. DNA-templated carbon nanotube field-effect transistor. *Science* **302,** 1380–1382 (2003).
10. Czerw, R., Guo, Z., Ajayan, P. M., Sun, Y. P. & Carroll, D. L. Organization of polymers onto carbon nanotubes: a route to nanoscale assembly. *Nano Lett.* **1,** 423–427 (2001).
11. Zheng, M. *et al.* Structure-based carbon nanotube sorting by sequence-dependent DNA assembly. *Science* **302,** 1545–1548 (2003).

12. Richard, C., Balavoine, F., Schultz, P., Ebbesen, T. W. & Mioskowski, C. Supramolecular self-assembly of lipid derivatives on carbon nanotubes. *Science* **300,** 775–778 (2003).
13. Worsley, K. A., Moonoosawmy, K. R. & Kruse, P. Long-range periodicity in carbon nanotube sidewall functionalization. *Nano Lett.* **4,** 1541–1546 (2004).
14. Mackiewicz, N. *et al.* Supramolecular self-assembly of amphiphiles on carbon nanotubes: A versatile strategy for the construction of CNT/metal nanohybrids, application to electrocatalysis. *J. Am. Chem. Soc.* **130,** 8110–8111 (2008).
15. Star, A. *et al.* Preparation and properties of polymer-wrapped single-walled carbon nanotubes. *Angew Chem. Int. Ed.* **40,** 1721–1725 (2001).
16. Kam, N. W. S., O'Connell, M., Wisdom, J. A. & Dai, H. Carbon nanotubes as multifunctional biological transporters and near-infrared agents for selective cancer cell destruction. *Proc. Natl Acad. Sci. USA* **102,** 11600–11605 (2005).
17. Bates, F. S. & Fredrickson, G. H. Block copolymers—designer soft materials. *Phys. Today* **52,** 32–38 (1999).
18. Hawker, C. J. & Russell, T. P. Block copolymer lithography: merging 'bottom-up' with 'top-down' processes. *MRS Bull.* **30,** 952–966 (2005).
19. Cheng, J. Y., Ross, C. A., Smith, H. I. & Thomas, E. L. Templated self-assembly of block copolymers: top-down helps bottom-up. *Adv. Mater.* **18,** 2505–2521 (2006).
20. Hamley, I. W. *Block Copolymers in Solution Fundamentals and Applications* (Wiley, 2005).
21. Kang, Y. J. & Taton, T. A. Micelle-encapsulated carbon nanotubes: a route to nanotube composites. *J. Am. Chem. Soc.* **125,** 5650–5651 (2003).
22. Kim, H. C., Rettner, C. T. & Sundstrom L. Fabrication of 20 nm half-pitch gratings by corrugation-directed self-assembly. *Nanotechnology* **19,** 235301 (2008).
23. Li, C. Y., Li, L. Y., Cai, W. W., Kodjie, S. L. & Tenneti, K. K. Nanohybrid shish-kebabs: periodically functionalized carbon nanotubes. *Adv. Mater.* **17,** 1198–1202 (2005).
24. Li, L., Li, C. Y. & Ni, C. Polymer crystallization-driven, periodic patterning on carbon nanotubes. *J. Am. Chem. Soc.* **128,** 1692–1699 (2006).
25. Li, L. Y. *et al.* Patterning polyethylene oligomers on carbon nanotubes using physical vapor deposition. *Nano Lett.* **6,** 1007–1012 (2006).
26. Qiao, R. & Ke, P. C. Lipid-carbon nanotube self-assembly in aqueous solution. *J. Am. Chem. Soc.* **128,** 13656–13657 (2006).
27. Li, Z. B., Kesselman, E., Talmon, Y., Hillmyer, M. A. & Lodge, T. P. Multicompartment micelles from ABC miktoarm stars in water. *Science* **306,** 98–101 (2004).
28. Cui, H. G., Chen, Z. Y., Zhong, S., Wooley, K. L. & Pochan, D. J. Block copolymer assembly via kinetic control. *Science* **317,** 647–650 (2007).
29. Li, B. & Li, C. Y. Immobilizing Au nanoparticles with polymer single crystals, patterning and asymmetric functionalization. *J. Am. Chem. Soc.* **129,** 12–13 (2007).
30. Du, Y. J. & Brash, J. L. Synthesis and characterization of thiol-terminated poly(ethylene oxide) for chemisorption to gold surface. *J. Appl. Polym. Sci.* **90,** 594–607 (2003).

Acknowledgements

This work was supported by National Science Foundation grant no. DMR-0804838.

Author contributions

C.L. and B.L. conceived and designed the experiments. B.L. performed the experiments, with help from L.L. and B.W. B.L. and C.L. co-wrote the paper. All authors discussed the results and commented on the manuscript.

Additional information

Supplementary information accompanies this paper at www.nature.com/naturenanotechnology. Reprints and permission information is available online at http://npg.nature.com/reprintsandpermissions/. Correspondence and requests for materials should be addressed to C.Y.L.

nature nanotechnology

LETTERS

PUBLISHED ONLINE: 6 APRIL 2009 | DOI: 10.1038/NNANO.2009.71

Tunable few-electron double quantum dots and Klein tunnelling in ultraclean carbon nanotubes

G. A. Steele*, G. Gotz and L. P. Kouwenhoven

Quantum dots defined in carbon nanotubes are a platform for both basic scientific studies[1–5] and research into new device applications[6]. In particular, they have unique properties that make them attractive for studying the coherent properties of single-electron spins[7–11]. To perform such experiments it is necessary to confine a single electron in a quantum dot with highly tunable barriers[1], but disorder has prevented tunable nanotube-based quantum-dot devices from reaching the single-electron regime[2–5]. Here, we use local gate voltages applied to an ultraclean suspended nanotube to confine a single electron in both a single quantum dot and, for the first time, in a tunable double quantum dot. This tunability is limited by a novel type of tunnelling that is analogous to the tunnelling in the Klein paradox of relativistic quantum mechanics.

Single spins in carbon nanotube quantum dots are expected to be very stable against both relaxation and decoherence[11]. Nuclear spins, the principal source of spin decoherence[7,8] in GaAs, can be completely eliminated and, furthermore, a strong spin–orbit interaction recently discovered in carbon nanotubes[9] allows all-electrical spin manipulation[10,11], while preserving long spin-relaxation and decoherence times[11]. Electron spins in carbon nanotube quantum dots are therefore attractive for implementation of a quantum bit (qubit) based on spin for applications in quantum-information processing[6]. In double quantum dot systems, precise control of the tunnel coupling between the two quantum dots, and between the quantum dots and the leads attached to them, is critically important for spin readout schemes[1,12,13], and also to prevent loss of spin and phase information through exchange of an electron with the leads.

Double quantum dots can also be used to explore novel quantum tunnelling phenomena. In Klein tunnelling[14–16], for example, an electron tunnels with a high probability through a potential energy barrier it would not normally tunnel through, when the height of the barrier is made comparable to twice the rest mass of the electron. It is not feasible to create such a barrier for free electrons due to the enormous electric fields required, but the low effective rest mass of the electrons in small-bandgap nanotubes makes the observation of such Klein tunnelling in nanotube devices possible[16].

By depositing metallic gates isolated by a dielectric layer on top of a nanotube, several groups have demonstrated tunable double quantum dots in nanotubes lying on a substrate[2–5]. These are tunable in the sense that the height and width of energy barriers between dots can be controlled by the gate. A disadvantage of this technique is that nanotubes in these devices suffer from significant disorder induced by the substrate and by the chemical processing required to fabricate the device. As the electron density is reduced, this random potential dominates and breaks the nanotube segment into multiple disorder-induced 'intrinsic' quantum dots before reaching the few-electron regime.

Wet etching of the device after fabrication to remove the substrate-induced disorder has been used previously to obtain single-electron quantum dots in carbon nanotubes[17,18], although experience has shown that the yield of such devices is quite low. Recently, a new fabrication method has been developed for producing ultraclean quantum dots in suspended carbon nanotubes with a high yield in which all chemical processing is done before nanotube growth[19]. Studying single quantum dots in these devices has uncovered new carbon nanotube physics, including a strong spin–orbit interaction due to the nanotube curvature[9] and evidence of Wigner crystallization of electrons at low density[20]. Although devices fabricated in this way are extremely clean, they have some significant limitations. In particular, the confinement is produced only by Schottky barriers, which cannot be easily tuned *in situ*. Furthermore it has not been possible to create a tunable double quantum dot in these ultraclean devices due to an insufficient number of local gates.

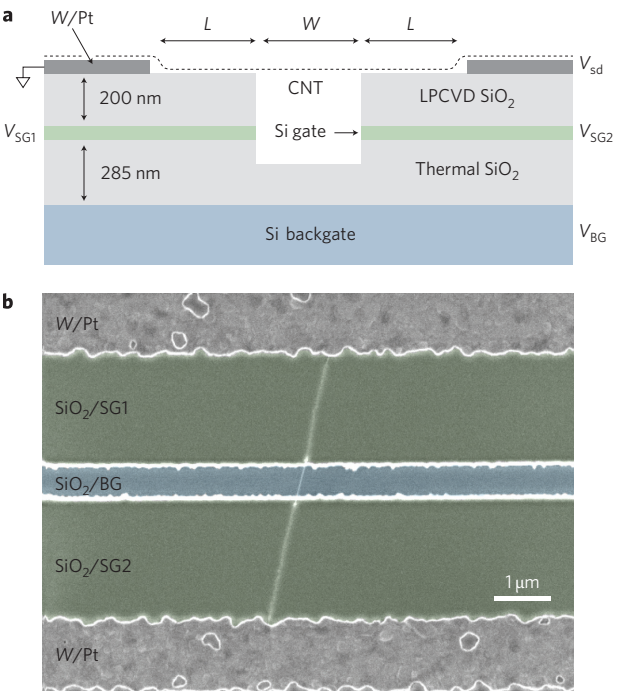

Figure 1 | Integrating local gates with ultraclean carbon nanotubes. **a**, Schematic of the device. A predefined trench is etched to create two splitgates from a 50-nm-thick n^{++} polysilicon gate layer (green) between two silicon oxide layers (grey). A platinum metal layer is deposited to act as source and drain contacts, and a nanotube is then grown from a patterned catalyst. Device D1 has dimensions $L = 1.5$ μm and $W = 300$ nm, and D2 has $L = 300$ nm and $W = 500$ nm. **b**, In a subset of devices, a single nanotube bridges the trench, contacting the metal source and drain electrodes (SEM image coloured for clarity). The micrograph shows an example of a device with the same dimensions as device D1.

Kavli Institute of NanoScience, Delft University of Technology, PO Box 5046, 2600 GA, Delft, The Netherlands. *e-mail: G.A.Steele@tudelft.nl

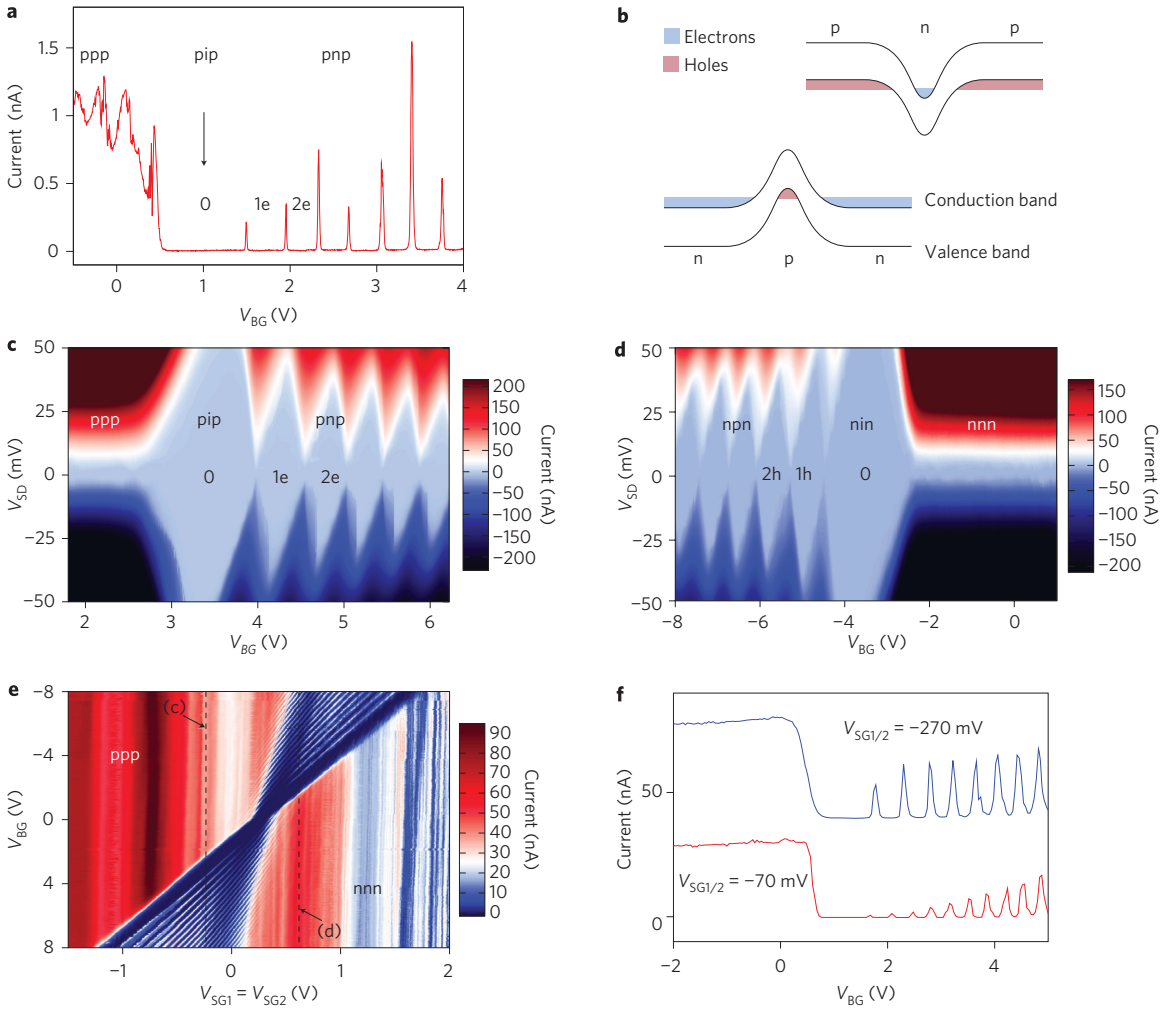

Figure 2 | Gate defined single-electron and single-hole quantum dots. a, Coulomb peaks of a pnp quantum dot in device D1 taken at $V_{SG1} = V_{SG2} = -50$ mV and $V_{SD} = 1$ mV. The splitgates are used to dope the nanotube source and drain leads with holes. As V_{BG} is swept from negative to positive voltages, the suspended segment is depleted giving a pip configuration, followed by a pnp configuration as single electrons are filled in an n-type quantum dot. **b**, Energy diagrams showing pnp and npn quantum dots formed by p-n junction confinement. **c**, Stability diagram of the pnp dot: the charging energy of the first electron $E_c^{1e} \approx 40$ meV is remarkably large due to the weak capacitive coupling of the suspended segment to the gates and the metal source drain layers. **d**, The potential landscape in the device can be completely controlled by the gate voltages: by reversing the gate voltages, single holes are confined in a npn configuration. **e**, A two-dimensional plot showing backgate sweeps at different splitgate voltages and $V_{SD} = 10$ mV. The two splitgates are set to the same voltage. The stability diagrams in **c** and **d** are taken at $V_{SG1/2}$ values indicated by the dashed lines. (Resonances from residual disorder in the long nanotube leads can be seen as oscillations as a function of $V_{SG1/2}$ in the ppp and nnn configurations.) **f**, Using the splitgates, we can tune the width of the p-n junction depletion region, and hence the tunnel barriers: at $V_{SG1} = V_{SG2} = -70$ mV, the potential from the splitgates is shallow, giving a wide depletion region and a current of 0.5 nA for the first electron Coulomb peak at $V_{SD} = 10$ mV. At $V_{SG1} = V_{SG2} = -270$ mV, the potential across the p-n junction is steeper, now giving a narrower depletion region and a current of 13 nA for the first electron. (The $V_{SG1/2} = -270$ mV trace has been offset in V_{BG} and in current.).

To overcome these limitations, we have developed a new method of integrating multiple local gates with ultraclean fabrication. A schematic of the device is shown in Fig. 1. As described in the Methods, we grew a carbon nanotube over gates that were patterned in a thin doped silicon layer. Our current design provides three independent gates, although fabrication can easily be modified to include a scalable number of gates inside the trench (see Supplementary Information). In this Letter, we use these three gates in two different ways. In device D1, with $L = 1.5$ μm, the gates are used to define a single-electron and single-hole quantum dot where electrons and holes are confined by tunable p–n junctions instead of Schottky contacts. In device D2, with $L = 300$ nm, we rely on tunnel barriers from the Schottky contacts, but now use the three gates to create a tunable single-electron and single-hole double quantum dot.

In all previous measurements of quantum dots in carbon nanotubes containing a single electron, carriers were confined by Schottky barriers formed at the metal contacts[9,17], or by potentials defined from trapped oxide charges[18]. In Fig. 2 we demonstrate a single-electron quantum dot defined only by gate voltages. We begin by applying a negative voltage to the splitgates, creating a p-type nanotube source and drain on top of the oxide. Sweeping the backgate voltage V_{BG}, shown in Fig. 2a, the current initially shows weak modulations from resonances in the leads when the suspended segment is p-type (ppp configuration), and is then completely suppressed as the suspended segment is depleted (pip configuration). As we sweep further, we form a pnp quantum dot showing clean Coulomb blockade, where single electrons in the suspended segment are confined by p–n junctions to the leads. Figure 2c shows a stability diagram as a function of both backgate and bias voltage, demonstrating that we have reached the single-electron regime. As the confinement potential and doping profile are determined by our local gates, we can also confine single holes

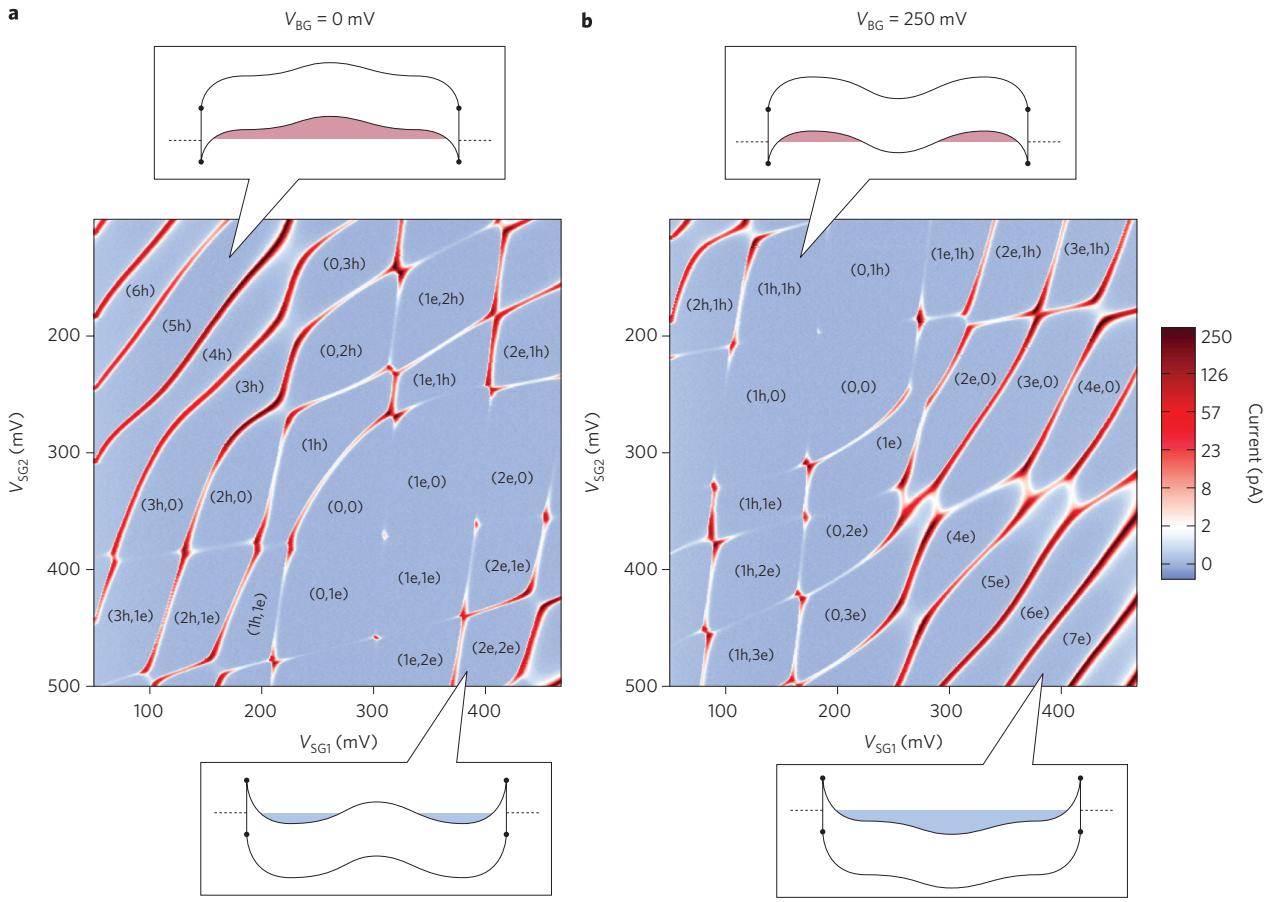

Figure 3 | A tunable double quantum dot in the few-electron and few-hole regime. Current as a function of the two splitgate voltages at $V_{SD} = 0.5$ mV for device D2. In device D2, electrons are confined in the nanotube by Schottky barriers at the metal contacts, with a potential that is tunable using the three gates. Electron and hole occupation numbers are determined from the transition to a pn double quantum dot, as described in the Supplementary Information. **a**, $V_{BG} = 0$. At this voltage, a barrier for electrons is induced in the middle of the device. Electrons are added to a weakly coupled double dot potential, and holes are added to a single dot potential. **b**, $V_{BG} = 250$ mV. A more positive V_{BG} creates a double dot potential for holes and a single dot potential for electrons. The interdot coupling for both the electron and the hole double dot can be tuned continuously using the backgate voltage.

in an npn configuration in the same device simply by inverting the gate voltages, shown in Fig. 2d. In Fig. 2e we show the current as a function of the backgate voltage and the voltage on the splitgates. In the left of the plot, the leads are doped p-type, and a positive backgate induces a single-electron pnp quantum dot. In the right of the plot, the leads are doped n-type and a negative backgate induces a single hole npn quantum dot. By adjusting the splitgate voltages, the p–n junction width, and thus the tunnel barriers, can be tuned while keeping the electron number fixed (see Fig. 2f).

In device D2, we use the gates in our design for a different purpose. We rely on less transparent Schottky contacts as incoming and outgoing tunnelling barriers, and now use the backgate and the two splitgates as three independent local gates to create a double quantum dot potential in the nanotube with a tunable interdot coupling. Figure 3 shows the current through the device as a function of the two splitgate voltages. In the lower left and upper right regions of the plots, the two splitgates dope the two segments of the nanotube with carriers of opposite sign, resulting in a pn double quantum dot with an interdot barrier formed from a p–n junction. In the upper left (bottom right) corner, the two splitgates dope both sides of the nanotube p-type (n-type). In Fig. 3a, V_{BG} is set to ground, which gives a potential in the middle of the nanotube that is attractive for holes but repulsive for electrons. We consequently observe single dot behaviour for the first hole and weakly coupled double dot behaviour for the first electron. In Fig. 3b, we apply a positive backgate voltage, $V_{BG} = 250$ mV. The potential in the middle of the nanotube is now repulsive for holes; the first hole enters a weakly coupled double dot, and electrons fill a mostly single dot potential. (At some gate voltages, the presence of the oxide creates a non-uniform potential that results in strongly coupled double dot instead of purely single dot behaviour. See Supplementary Section S1.) By changing V_{BG}, we can continuously tune the interdot coupling in the few-electron and few-hole regime from weakly coupled double dot to single dot behaviour.

In Fig. 4, we investigate the tunable inderdot coupling in our double quantum dot in more detail by studying current at the (0,1e)↔(1e,0) triple point transition of a weakly coupled double quantum dot. In a weakly coupled double quantum dot, current can only flow at specific values of the gate voltages, known as triple points, where the levels in the two dots are aligned, allowing an electron to tunnel from one dot to the other[21]. In Fig 4a to c, V_{BG} is made more negative, creating a larger barrier for electron tunnelling between the dots, suppressing the current at the triple point. However, as we sweep V_{BG} further, (Fig. 4d, e), the current increases again, despite creating an even larger barrier for electron tunnelling.

The explanation of this curious increase of the current is a novel tunnelling process analogous to the tunnelling paradox in high-energy physics proposed by Klein[14–16]. Specifically, we will define Klein tunnelling as any enhancement of the tunnelling of an electron through a barrier due to the so-called negative energy solutions

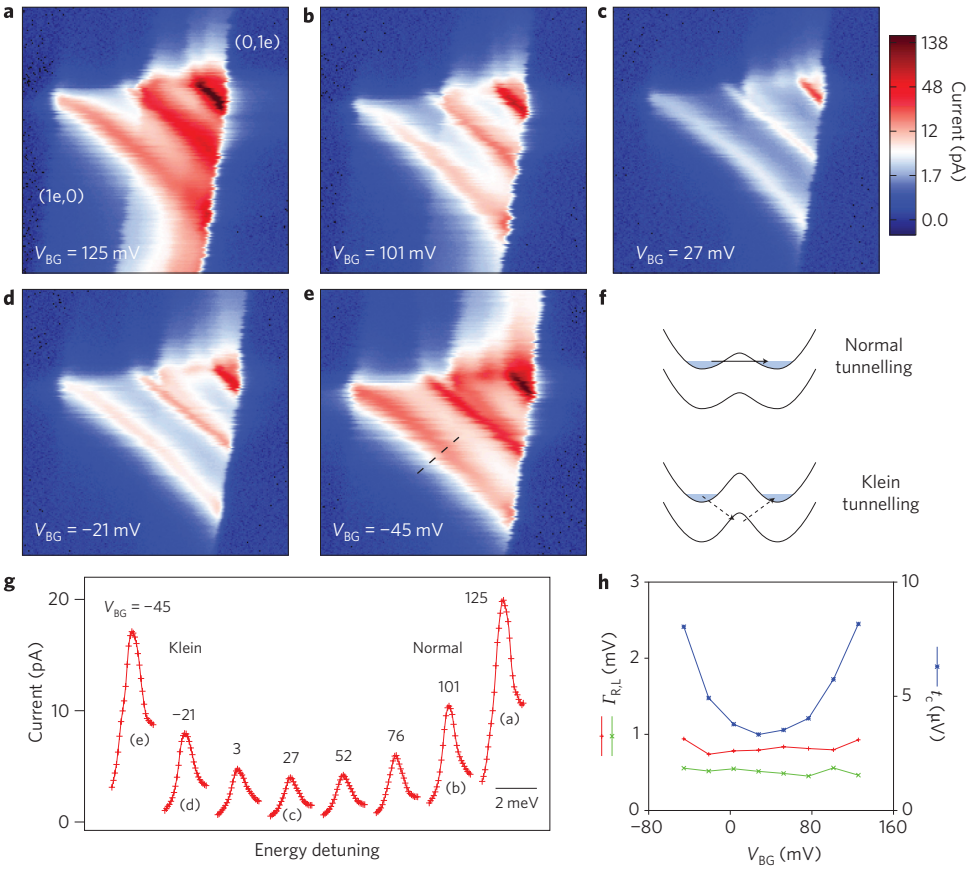

Figure 4 | Klein tunnelling in a single-electron double quantum dot. Current at the (0,1e) ↔ (1e,0) triple point for a single electron double quantum dot at $V_{SD} = 5$ mV. (Note that the interdot capacitance $E_c^{inter} \approx 0.2$ mV is much smaller than the bias, and thus the triple point bias triangles for the electron and hole cycle[21] strongly overlap.) Transitions to the excited state of the outgoing dot are visible as lines in the triangle running parallel to the baseline and give a quantized level spacing of 3 mV, consistent with a dot length of ~500 nm. **a–c**, The backgate is made more negative, creating a larger barrier for electron tunnelling. As a result, the current through the double dot is decreased. **d, e**, The current begins to increase again despite a larger barrier for electron tunnelling. **f**, This increase in current results from tunnelling of an electron below the barrier through a virtual state in the valence band, analogous to Klein tunnelling in high-energy physics. **g**, Line cuts of the triple point data in **a–e** showing the current for the ground-state baseline transition at different backgate voltages. The line cuts are taken along the dashed line in **e**. The *x* axis shows the distance along this line converted into the energy detuning between the left and right dot ground-state levels. For the rightmost traces, interdot tunnel coupling is mediated by normal electron tunnelling, and for the leftmost traces, Klein processes provide the interdot tunnel coupling. **h**, Parameters from a fit to the Stoof–Nazarov equation. The interdot tunnel coupling initially decreases as the barrier height increases ($V_{BG} = 125$ to 27 mV), and then increases due to the onset of Klein tunnelling as the barrier height becomes comparable to the bandgap ($V_{BG} = 27$ to −45 mV).

(positron states) that arise in relativistic quantum mechanics (see Supplementary Information for further discussion). In Fig. 4, the enhancement of the interdot coupling we observe at large tunnel barrier heights is an example of Klein tunnelling in a carbon nanotube, where the valence band of the nanotube now plays the role of the negative energy solutions in relativistic quantum mechanics. What is unique about the data in Fig. 4 is that we have created a direct implementation of Klein's gedanken experiment in our double quantum dot device, where we are able to tune continuously from the normal tunnelling regime to the Klein tunnelling regime simply by changing the barrier height with a gate voltage. We have also observed Klein tunnelling for holes (see Supplementary Information). In Fig. 4, what we observe is a kind of 'virtual' Klein tunnelling, where the electron virtually occupies a state in the empty valence band in order to tunnel from the left to the right dot, similar to a cotunnelling process[22]. In addition to our observations in a double quantum dot, the npn data in Fig. 2 can be thought of as a type of Klein tunnelling in a different regime, where the valence band is now occupied with holes, and where Klein tunnelling occurs by the electron sequentially tunnelling across the two p–n junctions. This also emphasizes the close relation between Klein tunnelling in high-energy physics and interband tunnelling phenomena in semiconductor physics, such as Zener tunnelling in insulators[23] and direct interband tunnelling in an Esaki diode[24].

Analysing the current at the (0,1e) ↔ (1e,0) transition quantitatively using the result from Stoof and Nazarov[25,26], we calculate the tunnel rates Γ_L and Γ_R of the barriers to the leads, and the interdot tunnel coupling t_c, shown in Fig. 4h. At these gate voltages, we are in the limit of weak interdot coupling: $t_c \approx 5\ \mu V \ll \Gamma_L, \Gamma_R \approx 0.6$ mV. The interdot coupling t_c is decreased from an initial value of 9 μV to a minimum of 3 μV as a function of backgate voltage, before the onset of Klein tunnelling results in an increase up to 9 μV as we approach gate voltages where an npn triple dot is formed. Γ_L and Γ_R are found to be independent of the backgate voltage, indicating that the backgate is not influencing the Schottky barrier transparency.

Finally, note that although we are in the appropriate double quantum dot coupling regime, we have not found evidence of spin blockade at any of the expected transitions[27]. (A parallel magnetic field of 1.5 T was applied to ensure that the nanotube valley degeneracy was lifted). One possible explanation for this is a singlet–triplet

splitting in the (0,2e) state that is much smaller than the 3 mV single particle spacing we observe in the single-electron quantum dot. This could be an indication of the formation of a Wigner crystal[20], in which the electron wavefunction overlap is very small, and consequently the single–triplet splitting is strongly suppressed. This possibility will be investigated further using devices with more gates, which could allow us to probe the Wigner crystallization transition by tuning the quantum dot confinement potential.

We have presented a new technique for confining single electrons and single holes in ultraclean carbon nanotubes. By eliminating disorder and incorporating local gates, a new level of control over single-electron confinement has been achieved, allowing us to observe a novel type of tunnelling in a single-electron carbon nanotube device. Although our motivation for such a device comes from the spin physics of carbon nanotubes[28], the fabrication itself could have a much broader use. This may include electrically doped p–n junctions for carbon nanotube optical emission[29], where low disorder and multiple gates for electrical control of p–n junctions could allow the development of new types of optically active devices.

Methods

Fabrication began with a p^{++} silicon wafer with 285 nm of thermal silicon oxide. On top of this, a 50-nm-thick n^{++} polysilicon gate layer was deposited, followed by a 200-nm LPCVD–TEOS oxide layer. Using electron-beam lithography and dry etching, a trench ~300 nm deep was etched, forming the two splitgates from the n^{++} silicon gate layer. A 5/25 nm W/Pt layer was deposited to serve as source and drain contacts, and nanotubes were then grown from patterned Mo/Fe catalyst[30]. In about half of the devices, a single carbon nanotube was suspended across the trench making electrical contact to the source and drain. Transport through the devices was characterized at room temperature, and selected devices were cooled to <300 mK for low temperature transport measurements. In total, we measured 11 devices at low temperatures, of which 4 reached the single electron regime. Here we present data from two small bandgap devices: D1 with $L = 1.5$ μm, $W = 300$ nm and bandgap $E_g = 60$ mV, and D2 with $L = 300$ nm, $W = 500$ nm and $E_g = 25$ mV, where bandgaps were determined by subtracting the charging energy from the size of the empty dot Coulomb diamond.

Received 29 September 2008; accepted 23 February 2009; published online 6 April 2009

References

1. Hanson, R., Kouwenhoven, L. P., Petta, J. R., Tarucha, S. & Vandersypen, L. M. K. Spins in few-electron quantum dots. *Rev. Mod. Phys.* **79,** 1217–1266 (2007).
2. Mason, N., Biercuk, M. J. & Marcus, C. M. Local gate control of a carbon nanotube double quantum dot. *Science* **303,** 655–658 (2004).
3. Sapmaz, S., Meyer, C., Beliczynski, P., Jarillo-Herrero, P. & Kouwenhoven, L. P. Excited state spectroscopy in carbon nanotube double quantum dots. *Nano Lett.* **6,** 1350–1355 (2006).
4. Jørgensen, H. I., Rasmussen, G. K., Hauptmann, J. R. & Lindelof, P. E. Single wall carbon nanotube double quantum dot. *Appl. Phys. Lett.* **89,** 232113 (2006).
5. Gräber, M. R. *et al.* Molecular states in carbon nanotube double quantum dots. *Phys. Rev. B* **74,** 075427 (2006).
6. Loss, D. & Divincenzo, D. P. Quantum computation with quantum dots. *Phys. Rev. A* **57,** 120–126 (1998).
7. Petta, J. R. *et al.* Coherent manipulation of coupled electron spins in semiconductor quantum dots. *Science* **309,** 2180–2184 (2005).
8. Koppens, F. H. L. *et al.* Universal phase shift and nonexponential decay of driven single-spin oscillations. *Phys. Rev. Lett.* **99,** 106803 (2007).
9. Kuemmeth, F., Ilani, S., Ralph, D. C. & McEuen, P. L. Coupling of spin and orbital motion of electrons in carbon nanotubes. *Nature* **452,** 448–452 (2008).
10. Nowack, K. C., Koppens, F. H. L., Nazarov, Y. & Vandersypen, L. M. K. Coherent control of a single electron spin with electric fields. *Science* **318,** 1430–1433 (2007).
11. Bulaev, D. V., Trauzettel, B. & Loss, D. Spin-orbit interaction and anomalous spin relaxation in carbon nanotube quantum dots. *Phys. Rev. B* **77,** 235301 (2008).
12. Fujisawa, T., Austing, D. G., Tokura, Y., Hirayama, Y. & Tarucha, S. Allowed and forbidden transitions in artificial hydrogen and helium atoms. *Nature* **419,** 278–281 (2002).
13. Elzerman, J. M. *et al.* Single-shot read-out of an individual-electron spin in a quantum dot. *Nature* **430,** 431–435 (2004).
14. Klein, O. Die Reflexion von Elektronen an einem Potentialsprung nach der relativistischen Dynamik von Dirac. *Z. Phys.* **53,** 157–165 (1929).
15. Katsnelson, M. I., Novoselov, K. S. & Geim, A. K. Chiral tunnelling and the Klein paradox in graphene. *Nature Phys.* **2,** 620–625 (2006).
16. Trauzettel, B., Bulaev, D. V., Loss, D. & Burkard, G. Spin qubits in graphene quantum dots. *Nature Phys.* **3,** 192–196 (2007).
17. Jarillo-Herrero, P., Sapmaz, S., Dekker, C., Kouwenhoven, L. P. & van der Zant, H. S. Electron–hole symmetry in a semiconducting carbon nanotube quantum dot. *Nature* **429,** 389–392 (2004).
18. Minot, E. D., Yaish, Y., Sazonova, V. & Mceuen, P. L. Determination of electron orbital magnetic moments in carbon nanotubes. *Nature* **428,** 536–539 (2004).
19. Cao, J., Wang, Q. & Dai, H. Electron transport in very clean, as-grown suspended carbon nanotubes. *Nature Mater.* **4,** 745–749 (2005).
20. Deshpande, V. V. & Bockrath, M. The one-dimensional Wigner crystal in carbon nanotubes. *Nature Phys.* **4,** 314–318 (2008).
21. van der Wiel, W. G. *et al.* Electron transport through double quantum dots. *Rev. Mod. Phys.* **75,** 1–22 (2002).
22. De Franceschi, S. *et al.* Electron cotunneling in a semiconductor quantum dot. *Phys. Rev. Lett.* **86,** 878–881 (2001).
23. Zener, C. A theory of the electrical breakdown of solid dielectrics. *Roy. Soc. Proc.* **145,** 523–529 (1934).
24. Esaki, L. New phenomenon in narrow germanium p–n junctions. *Phys. Rev.* **109,** 603–604 (1958).
25. Stoof, T. H. & Nazarov, Y. Time-dependent resonant tunneling via two discrete states. *Phys. Rev. B* **53,** 1050–1053 (1996).
26. Fujisawa, T. *et al.* Spontaneous emission spectrum in double quantum dot devices. *Science* **282,** 932–935 (1998).
27. Ono, K., Austing, D. G., Tokura, Y. & Tarucha, S. Current rectification by Pauli exclusion in a weakly coupled double quantum dot system. *Science* **297,** 1313–1317 (2002).
28. Churchill, H. O. H. *et al.* Electron–nuclear interaction in ^{13}C nanotube double quantum dots. Preprint at <http://arxiv.org/abs/0811.3236>.
29. Misewich, J. A. *et al.* Electrically induced optical emission from a carbon nanotube FET. *Science* **300,** 783–786 (2003).
30. Kong, J., Soh, H. T., Cassell, A. M., Quate, C. F. & Dai, H. Synthesis of individual single-walled carbon nanotubes on patterned silicon wafers. *Nature* **395,** 878–881 (1998).

Acknowledgements

It is a pleasure to acknowledge P.L. McEuen for the suggestion of using p–n junctions as tunable barriers, as well as D. Loss, T. Balder, I.T. Vink, R.N. Schouten, L.M.K. Vandersypen, and M.H.M. van Weert for useful discussions and suggestions. This research was supported by the Dutch Organization for Fundamental Research on Matter (FOM), the Netherlands Organization for Scientific Research (NWO), and the Japan Science and Technology Agency International Cooperative Research Project (JST-ICORP).

Author contributions

G.A.S. was responsible for the experimental work. All authors discussed the results and commented on the manuscript.

Additional information

Supplementary information accompanies this paper at www.nature.com/naturenanotechnology. Reprints and permission information is available online at http://npg.nature.com/reprintsandpermissions/. Correspondence and requests for materials should be addressed to G.A.S.

nature nanotechnology

LETTERS

PUBLISHED ONLINE: 19 APRIL 2009 | DOI: 10.1038/NNANO.2009.81

The crossover from two dimensions to one dimension in granular electronic materials

Ke Xu†, Lidong Qin† and James R. Heath*

Granular conductors[1] are solids comprising densely packed nanoparticles, and have electrical properties that are determined by the size, composition and packing of the composite nanoparticles. The ability to control these properties in two- and three-dimensional granular conductors has made such systems appropriate for use as prototypes for investigating new physics[1–4]. However, the fabrication of strictly one-dimensional granular conductors remains challenging. Here, we describe a method for the assembly of nanoparticles into granular solids that can be tuned continuously from two to one dimension, and establish how electron transport evolves between these limits. We find that the energy barriers to transport increase in the one-dimensional limit, in both the variable-range-hopping (low-voltage) and sequential-tunnelling (high-voltage) regimes. Furthermore, in the sequential-tunnelling regime we find an unexpected relationship between the temperature and the voltage at which the conductance becomes appreciable — a relationship that appears peculiar to one-dimensional systems. These results are explained by extrapolating existing granular conductor theories to one dimension.

A particularly rich area of nanoscale science is the investigation of low-dimensional systems, such as two-dimensional thin films, one-dimensional nanowires and zero-dimensional quantum dots[2,5–7]. In such systems, the electronic structure of the material and the statistical distribution of charge transport pathways are strongly influenced by dimensionality. An equally rich area, but one that is more difficult to investigate, is the physics associated with dimensional crossover. Granular conductors[1], in principle, provide the flexibility for investigating such crossovers. This is because the constituent nanoparticle properties[8] are independent of how they are assembled. Indeed, granular materials self-assembled from monodisperse, chemically synthesized colloidal quantum dots (QDs)[2,5,6] into highly ordered three- and two-dimensional architectures[2–4] have provided a laboratory for investigating new physics, including, for instance, the long-range resonance transfer of electronic excitations in three-dimensional QD solids[2] and the metal-to-insulator transition in two-dimensional QD superlattices[3]. In contrast, attempts to assemble nanoparticles into ordered one-dimensional (single-file nanoparticle arrays/chains) or quasi-one-dimensional granular structures have only achieved limited success[9–14], largely due to the difficulty in obtaining continuously connected one-dimensional superstructures.

We used a template-directed approach to align QDs into densely packed one-dimensional superstructures, using surface interactions between nanopatterned substrates and QD solutions. Similar methods have been used to fabricate ordered nano/microsphere assemblies over particle sizes ranging from micrometres to 50 nm (refs 15–17). In this study, ordered QD one-dimensional assemblies were achieved by precisely controlling the widths of nanopatterned one-dimensional trenches (the templates) to within ~1 nm, using QDs characterized by a narrow size distribution and controlling the QD/trench chemical interface.

Arrays of SiO_2 nanotrenches were fabricated using superlattice nanowire pattern transfer[18], which translates atomic control over the film thicknesses within a $GaAs/Al_xGa_{1-x}As$ superlattice into control over the width and spacing of nanotrenches. The nanotrench surfaces were chemically functionalized with hexamethyldisilazane. The resultant hydrophobic substrate was dip-coated in a toluene solution of QDs (Fig. 1a, b). A wetting meniscus was formed in the process.

Closest-packed QDs fill the nanotrenches (Fig. 1c–f). Figure 1c shows the fidelity of this technique: well-ordered, 3-QD-wide, closest-packed structures are observed in each of the nanotrenches, with lengths of up to 1 mm. The QD solution coats the entire wafer during dip-coating, but only leaves a single layer of QDs deposited within the trenches—a result that likely arises from the increased QD/surface interactions within the trenches. The packing pattern can be fine-tuned by either adjusting the trench width (Fig. 1c–f) or the size or shape of the QD (see Supplementary Information). For each of the arrays reported here, the dipping rate was also an important and separately optimized parameter. The technique works well for trench widths of $\geq$5 nm (see Supplementary Fig. S1).

The assembly method typically generates >100 identically packed parallel QD arrays. This enabled us to sample a statistically relevant number of QD arrays for each of the transport measurements reported here. The insulating SiO_2 trench walls prevent electrical crosstalk between adjacent QD arrays. Magnetite QDs, used as our model system, are half-metallic, and strong magnetoresistance effects have been reported[19].

To characterize how the two-dimensional → one-dimensional crossover influences the electrical properties of granular electronic systems, we investigated a single QD size (15 nm) and varied the trench widths to control the number of QDs across the width of each array. Quasi-one-dimensional arrays with 3 (Fig. 1c), 2 (Fig. 1e) and 1.5 (zigzag structure, Fig. 1f) QDs across the width, as well as one-dimensional linear arrays (Fig. 1d) were studied and compared with a close-packed QD monolayer film. Other research groups have found that quasi-one-dimensional QD arrays as narrow as four-QD wide are electronically similar to full two-dimensional arrays[11].

We fabricated about 50 devices, each contacting 50 to 400 parallel, identically packed one-dimensional or quasi-one-dimensional arrays (Fig. 2a), and plotted the measured resistance per array as a function of array length (see Supplementary Information). A linear dependence is observed, indicating that the device transport properties are dominated by the QD arrays, with negligible contribution from contacts. Owing to the large number of parallel channels, defects such as missing particles are not expected to affect the measurements at the array lengths reported here. Large negative magnetoresistance were found for all devices, verifying that the

Kavli Nanoscience Institute and Division of Chemistry and Chemical Engineering, California Institute of Technology, MC 127-72, Pasadena, California 91125, USA; †These authors contributed equally to this work. *e-mail: heath@caltech.edu

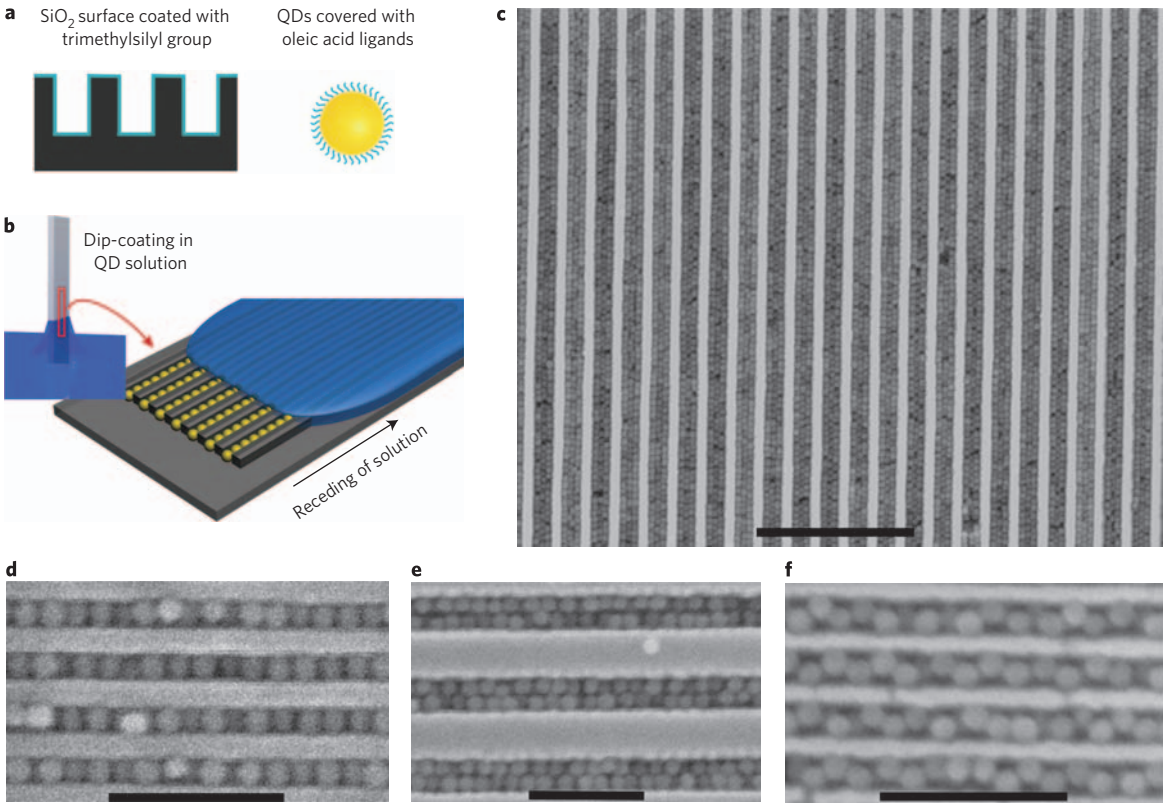

Figure 1 | Assembling QDs into one-dimensional and quasi-one-dimensional arrays. a, Surface functionalization of silica nanowire/nanotrench arrays (left) and a schematic of a QD and its surface ligands (right). **b**, Dip-coating method to fabricate QD arrays: one-dimensional QD arrays are formed as the QD solution recedes along the nanotrench substrate. **c–f**, SEM images of 3-line (**c**), 1-line (**d**), 2-line (**e**) and 1.5-line (**f**) (zigzag) QD arrays of 15 nm magnetite QDs. Scale bars, 400 nm (**c**), 100 nm (**d–f**).

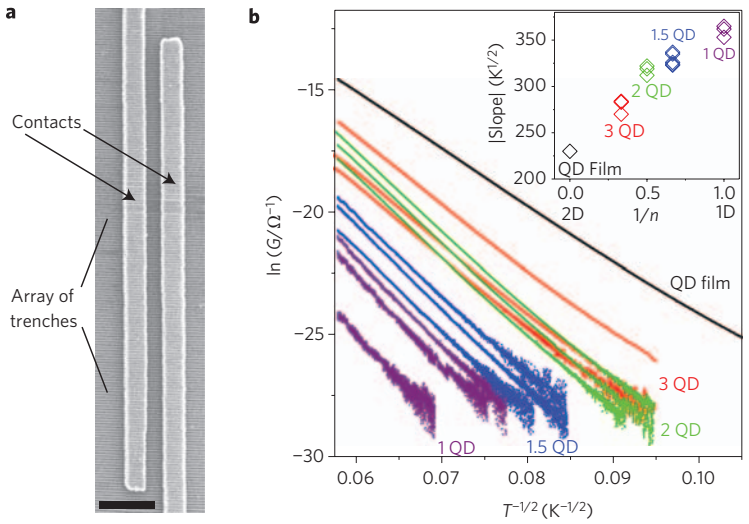

Figure 2 | Conductance measurement of the QD arrays. a, SEM image of a typical device used for the electrical measurements, which contacts 160 parallel one-dimensional QD arrays. Scale bar, 1 μm. **b**, Temperature-dependent conductance at low voltage bias. The number of QDs across the width of each array is indicated. One-dimensional zigzag arrays are labelled as 1.5 QD. Inset: $\ln(G)$–$T^{-1/2}$ slopes of the QD arrays plotted as a function of the dimensionality of the system, where n is the number of QDs across the width of each array.

measured electrical properties arise from the magnetite QD arrays (see Supplementary Information).

The conductance G of the QD arrays was studied at low (<100 mV) applied voltage bias as a function of temperature T (Fig. 2b). A linear dependence was found for all arrays when G was plotted on a logarithmic scale against $T^{-1/2}$, in agreement with previous studies on two- and three-dimensional QD assemblies[19–23]. Such behaviour is commonly ascribed[20–23] to the Efros–Shklovskii variable-range hopping (ES-VRH)[24] (or super-exchange[25]) transport mechanisms, although recent studies have also suggested alternative

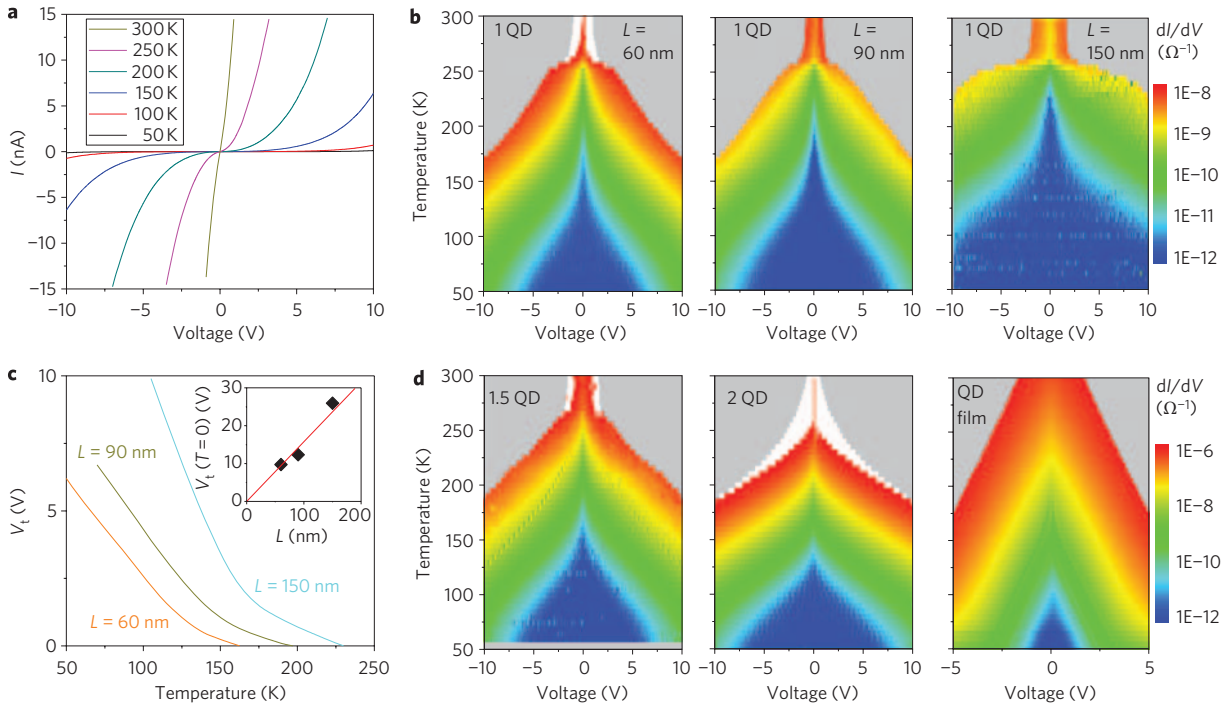

Figure 3 | Electrical properties of the QD arrays at high voltage. a, *I–V* curves of a QD one-dimensional linear array device at various temperatures. **b**, Differential conductance (d*I*/d*V*) as a function of voltage and temperature for one-dimensional linear arrays with various lengths. White areas indicate regions in which the differential conductance is higher than the upper limit of the colour scale. Grey areas indicate unmeasured regions in which the current level would be higher than the upper compliance of current (~20 nA) set to protect the devices. **c**, Threshold voltage as a function of temperature for the three devices in **b**. Inset: extrapolated threshold voltage at 0 K as a function of length. **d**, Differential conductance as a function of voltage and temperature for a one-dimensional zigzag QD array device, a quasi-one-dimensional device with two QDs across the width of each array, and a two-dimensional QD monolayer film. The colour scale shown in **b** applies to the one-dimensional zigzag and quasi-one-dimensional devices, whereas the expanded scale in **d** applies for the QD film device. Grey areas indicate unmeasured regions.

mechanisms[1,23] such as elastic and inelastic co-tunnelling[1]. We use the ES-VRH model to explain our data because that model has been the most widely used and permits the broadest comparison of our results against the literature.

Precisely controlled assembly helps to reveal trends in our G–T data: similar $\ln(G)$–$T^{-1/2}$ slopes were found for devices with the same designed numbers of QDs across the width of each array (see Supplementary Information for the consistent slopes obtained on five different one-dimensional zigzag array devices), whereas notably (up to ~60%) steeper slopes were observed as the QD assemblies cross over from two to one dimension (Fig. 2b, inset).

The results presented in Fig. 2 indicate an increasing energy barrier for charge transport accompanies the two- to one-dimensional crossover. According to VRH, charge transport efficiency is determined by the optimal hopping network, which in turn is determined by competition between the hopping distance and the number of available energy levels at a given distance. ES-VRH predicts a linear $\ln(G)$–$T^{-1/2}$ relationship[24]:

$$G(T) \sim \exp[-(T_0/T)^{1/2}],\ T_0 = \beta_D e^2/\kappa a \qquad (1)$$

where e is the electron charge, κ is the dielectric constant, and a is the localization length, which characterizes the decay length of electronic wavefunctions and in QD arrays is approximately the size of each QD (refs 21,22). The coefficient β_D depends on the system dimensionality D, and should increase as D is reduced; establishing a (percolating) hopping network becomes increasingly difficult with reducing dimensions, and so the energy barrier for conductance is higher. For three- and two-dimensional cases, theory and simulations indicate[26,27] that $\beta_3 \approx 2.8$ and $\beta_2 \approx 6.5$. No theoretical investigation of β_1 has been reported. Our data allow for an experimental determination of β_1. The consistent trend of the $\ln(G)$–$T^{-1/2}$ slopes suggests that β_D increases progressively as the array evolves from two to one dimension. For one-dimensional linear arrays, the absolute value of the $\ln(G)$–$T^{-1/2}$ slope increases to 360 $K^{1/2}$ from 230 $K^{1/2}$ in two dimensions. Consequently, assuming similar localization lengths for one- and two-dimensional arrays, this suggests $\beta_1/\beta_2 \approx (360/230)^2 = 2.45$ and $\beta_1 \approx 16$. This result is plausible, considering that a 2.3-fold (6.5/2.8) increase in β_D is found for two-dimensional systems when compared to three-dimensional systems.

At low temperatures, conductance due to the thermally activated hopping processes falls below the detection limit at low bias voltages. On the other hand, high bias voltages can overcome the Coulomb blockade and result in measurable conductance through sequential tunnelling between nearest-neighbour particles. This different mechanism of conductivity should yield different dimensional/geometric effects.

Figure 3a presents the *I–V* curves measured on a one-dimensional linear QD array device at different temperatures. As the temperature is lowered from room temperature, a gap of low current opens up at low voltages[10,23,28,29], and a finite threshold voltage V_t is required for the onset of appreciable ($>5 \times 10^{-12}\ \Omega^{-1}$) conductance. To further characterize how the electrical properties evolve for all temperatures, we present in Fig. 3b the differential conductance dI/dV measured on three one-dimensional linear array devices as a function of both V and T, from which the V_t–T relationship can be readily identified (Fig. 3c).

V_t is found to be directly proportional to the length of the assembly, L, both for one-dimensional linear arrays (Fig. 3c) and zigzag arrays (see Supplementary Information). This result was predicted[30,31]: V_t, the overall energy barrier for charge transport, is proportional to the

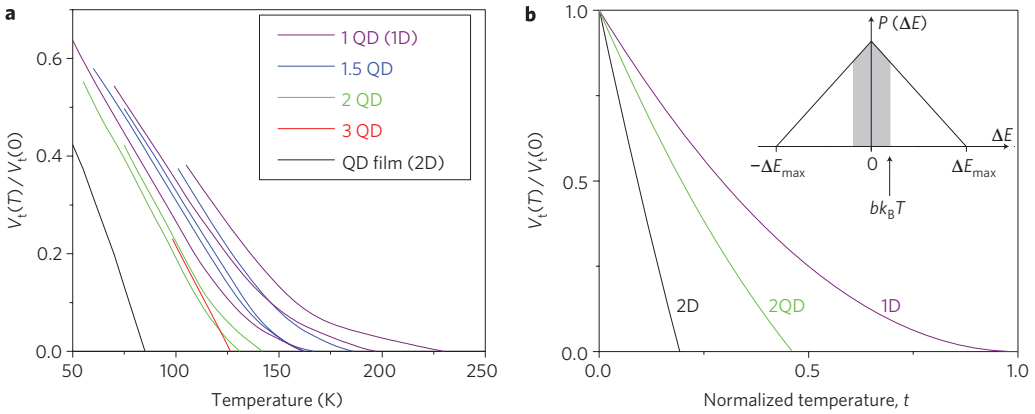

Figure 4 | Temperature dependence of the threshold voltage. a, Experimental threshold voltage–temperature dependence measured on different QD array devices. The threshold voltages are normalized to the extrapolated values at 0 K. The number of QDs across the width of each array is indicated in the graph. One-dimensional zigzag arrays are labelled as 1.5 QD. **b**, Theoretical threshold voltage–temperature dependence. Black and purple lines represent the two- and one-dimensional cases, respectively. The green line represents an intermediate case with $p_c = 0.71$, corresponding to 2-QD-wide quasi-one-dimensional arrays (see Supplementary Information). t is the normalized temperature, where $t = bk_BT/\Delta E_{max}$. Inset: probability distribution for ΔE in tunnelling events.

number of tunnelling barriers in the conduction path, which is in turn proportional to L. This contrasts with the low-voltage VRH conductance, in which the relevant energy barrier for charge transport (T_0) only depends on the localization length and the dimensionality of the system (equation (1)). As a result, similar $\ln(G)$–$T^{-1/2}$ slopes are found for different devices with the same numbers of QDs across the width of each array, regardless of L (Fig. 2b).

For the one-dimensional arrays, a linear V_t–T relationship is observed at low T, but at high T and low V, a pronounced sublinear V_t–T relationship is found (Fig. 3b,c). This indicates that more thermal energy is required to overcome the remaining energy barriers for charge transport. Linear V_t–T relationships have been observed previously up to the temperature where V_t drops to zero in two-dimensional QD assemblies[28,29] and quasi-one-dimensional chains of irregular nanoparticles[10], and has been explained by theory[31,32]. The sublinear V_t–T relationship we find has neither been predicted nor observed previously. Our results (Figs 3b–d,4a) indicate that this phenomenon is peculiar to one-dimensional QD arrays: the sublinearity is pronounced in both the one-dimensional linear and zigzag arrays, barely seen in 2-QD-wide quasi-one-dimensional arrays, and not observed at all in wider quasi-one-dimensional QD arrays or two-dimensional QD films.

This novel sublinear V_t–T relationship can be explained by extrapolating the theoretical discussions of Jaeger and colleagues[29,31]. Consider the case when the coupling capacitance between QDs is negligible compared to C_0, the capacitance of an individual QD. When an electron tunnels from a QD to its nearest neighbour, the energy change for the system, ΔE, falls into the range $[-\Delta E_{max}, \Delta E_{max}]$, where $\Delta E_{max} = e^2/C_0$, and a triangle-shaped distribution of the probability density, $P(\Delta E)$, is expected (Fig. 4b, inset)[29]. A finite temperature broadens the energy levels of the QDs, and conduction barriers are removed for neighbouring QDs satisfying $|\Delta E| < bk_BT$, where $b \approx 2.4$ characterizes the extent of thermal broadening of the Fermi–Dirac distributions in QDs (ref. 31). When the fraction of conduction barriers being removed, $p(T)$, reaches the bond percolation threshold of the lattice, p_c, a continuous path with all barriers removed emerges, and $V_t(T)$ drops to zero. The V_t–T relationship is thus modelled as[31] $V_t(T)/V_t(0) = 1 - p(T)/p_c$.

Previous studies[29,31] have considered the two-dimensional case, where $p_c \approx 0.347$ is small due to the existence of multiple possible pathways. Only 34% of all the conduction barriers need to be overcome for $V_t(T)$ to drop to 0 (the shaded area in Fig. 4b inset). In this region, $P(\Delta E)$ is effectively constant, so the same increment of temperature results in the removal of the same number of conductance barriers. As a result, a linear V_t–T relationship is observed.

By contrast, one-dimensional lattices have only a single pathway available for tunnelling conductance ($p_c = 1$), and so every tunnel barrier must be overcome for current to flow. Because $P(\Delta E)$ is considerably smaller for larger $|\Delta E|$, smaller numbers of barriers are removed for an equal temperature increase at higher T. In particular, because $P(\Delta E)$ drops towards zero when $|\Delta E|$ approaches ΔE_{max}, the last small fraction of barriers that keep V_t from dropping to zero are especially difficult to overcome. This explains the sublinear dependence of V_t on T we find at high temperature and low bias.

By integrating $P(\Delta E)$ from $-bk_BT$ to bk_BT, we have plotted the theoretical V_t–T relationship (Fig. 4b). The results satisfactorily capture our experimental data (Fig. 4a) for the two- and one-dimensional cases, and support our observation that the sublinearity is peculiar to truly one-dimensional QD arrays: p_c drops rapidly below 1 for quasi-one-dimensional arrays; for 2-QD-wide arrays, $p_c \approx 0.71$, and the sublinearity becomes much less noticeable (Fig. 4b).

Similar V_t–T behaviours were observed for one-dimensional linear and zigzag arrays, because they are topologically equivalent for percolation in the tunnelling regime; that is, each QD has two nearest neighbours for charge tunnelling. In contrast, in the VRH regime, the zigzag arrangement allows for an increase in the density of hopping pathways, and therefore appreciably smaller β_D and $\ln(G)$–$T^{-1/2}$ slopes are found relative to the linear arrangement (Fig. 2b, inset).

The described approach for assembling arrays of monodisperse QDs permits the electron transport properties of granular systems to be characterized across the two- to one-dimensional crossover. The electrical properties of one-dimensional granular systems are significantly different from two-dimensional systems, due to the single available transport pathway in one dimension. Harnessing related approaches to characterize other, equally rich transport phenomena such as thermal conductance represents an exciting future challenge.

Methods

SiO_2 superlattice nanowire pattern transfer nanotrench array preparation. An array of platinum superlattice nanowire pattern transfer (SNAP) nanowires was obtained by electron-beam evaporation onto the raised edges of a differentially etched edge of a epitaxially grown GaAs/$Al_xGa_{(1-x)}As$ superlattice wafer (IQE) (ref. 18). In this way, atomic control over the epilayer thicknesses of the superlattice stack was translated into control over the width and spacing of nanowires. The array of platinum SNAP nanowires was then transferred as an ink onto a 300-nm-thick, thermally grown SiO_2 layer on top of a silicon substrate. A thin (~10 nm) layer of heat-curable epoxy (EpoxyBond 110, Allied High Tech) was used to securely bond the platinum nanowire array to the surface. The superlattice/nanowire

array/epoxy/SiO_2 substrate assembly was baked on a hot plate at 150 °C for 15 min, and the superlattice was then released by a wet etch in a $H_3PO_4/H_2O_2/H_2O$ (5:1:50 v/v, 4.5 h) solution, leaving a highly aligned array of platinum nanowires on the surface of the SiO_2 substrate. The platinum nanowire array served as the protective mask for a reactive ion etch (RIE) process to produce a highly ordered SiO_2 nanowire/nanotrench array. A highly directional, 40 MHz Unaxis SLR parallel-plate RIE system was implemented to produce 50-nm-deep trenches in SiO_2 using CF_4/He (20/30 s.c.c.m., 5 mtorr, 40 W). The platinum nanowires were then dissolved in aqua regia (3:1 HCl:HNO_3) at boiling temperature for 30 min. The wafer was then rinsed with water and dried with a nitrogen blow, and heated in PRX-127 (Rohm & Haas LLC) to remove residual epoxy and other possible organic contaminants. Eventually, a highly ordered, ultrahigh-density array of SiO_2 nanowires/nanotrenches was obtained with a clean surface. The width of each nanowire is controlled by the thickness of the $Al_xGa_{(1-x)}As$ epilayers in the starting superlattice wafer, while the width of each nanotrench is controlled by the thickness of the GaAs epilayers. The number of nanowires/nanotrenches in the array is controlled by the number of epilayers in the superlattice wafer.

Superlattice nanowire pattern transfer nanotrench array surface functionalization. The as-prepared nanotrench array wafer was heated in a piranha solution (3:1 H_2SO_4:H_2O_2) at 120 °C for ~10 min, rinsed with water, and dried on a hot plate at 160 °C. The wafer was then surface-functionalized by exposure to a hexamethyldisilazane (Sigma-Aldrich) vapour within a sealed chamber. The resulting hydrophobic substrates formed a wetting meniscus contact with a toluene solution of QDs.

Quantum dot solution preparation. QDs covered with oleic acid ligands were used in this study. All the magnetite QD solutions were purchased from Ocean Nanotech. For the 15-nm QDs, the as-purchased chloroform solution (48 mg ml^{-1}) was diluted 40 times with toluene for a final concentration of 1.2 mg ml^{-1}. The diluted QD solution appeared dark grey and QDs were completely dispersed without any precipitates. The 25 and 40 nm magnetite QD solutions were prepared with the same protocol to a concentration of 1.5 and 2.0 mg ml^{-1}, respectively. Gold QDs (5 nm, from Xingchen Ye in the Christopher Murray Lab at the University of Pennsylvania), were dissolved in toluene to a final concentration of 5.0 mg ml^{-1}.

Assembling quantum dots into nanotrench arrays. The QD assembly step was performed by dip-coating a surface-functionalized SiO_2 nanotrench array wafer in a toluene solution of QDs. The wafer, clamped by a pair of tweezers and fixed onto a syringe pump (NE-1000 programmable syringe pump, New Era Pump Systems), was slowly withdrawn from the QD solution at a finely controlled speed (~0.5 mm min^{-1}) set to the gears of the pump. The speed was optimized for the formation of a close-packed monolayer inside each nanotrench (see Supplementary Information).

Annealing of magnetite quantum dot arrays. All assembled magnetite QD arrays were annealed to form a conductive phase[19]. The wafer with QD arrays was heated to 400 °C and annealed at this temperature for 60 min under the protection of ultrahigh-purity argon in a tube furnace (Linderberg, Model 54233), then cooled to room temperature overnight. The annealed QD arrays kept their original shape and arrangement as confirmed by scanning electron microscopy (SEM).

Fabricating electrodes to contact the quantum dot arrays. Metallic contact electrodes were patterned across the annealed QD arrays using electron-beam lithography. Two parallel electrodes (30-nm-thick titanium and 150-nm-thick gold), separated by a designed distance (from 50 to 500 nm), were precisely positioned across QD arrays according to alignment markers that were patterned on the wafer in an earlier step. The two electrodes were then connected to two large (150×150 μm^2) gold pads from opposite directions (Fig. 2a), so the measured current was transmitted through a well-defined number of QD arrays. The pads were then wire-bonded to a chip carrier.

Temperature- and magnetic-field-dependent electrical measurements. All electrical measurements were carried out in a Magnetic Property Measurement System (MPMS-XL, Quantum Design) with standard d.c. techniques using a Keithley 6430 sub-femtoamp remote sourcemeter.

Received 20 January 2009; accepted 17 March 2009; published online 19 April 2009

References

1. Beloborodov, I. S., Lopatin, A. V., Vinokur, V. M. & Efetov, K. B. Granular electronic systems. *Rev. Mod. Phys.* **79,** 469–518 (2007).
2. Murray, C. B., Kagan, C. R. & Bawendi, M. G. Synthesis and characterization of monodisperse nanocrystals and close-packed nanocrystal assemblies. *Ann. Rev. Mater. Sci.* **30,** 545–610 (2000).
3. Markovich, G. *et al.* Architectonic quantum dot solids. *Acc. Chem. Res.* **32,** 415–423 (1999).
4. Fan, H. Y. *et al.* Self-assembly of ordered, robust, three-dimensional gold nanocrystal/silica arrays. *Science* **304,** 567–571 (2004).
5. Bawendi, M. G., Steigerwald, M. L. & Brus, L. E. The quantum mechanics of larger semiconductor clusters (quantum dots). *Ann. Rev. Phys. Chem.* **41,** 477–496 (1990).
6. Alivisatos, A. P. Semiconductor clusters, nanocrystals and quantum dots. *Science* **271,** 933–937 (1996).
7. Xia, Y. N. *et al.* One-dimensional nanostructures: Synthesis, characterization and applications. *Adv. Mater.* **15,** 353–389 (2003).
8. Remacle, F. & Levine, R. D. Quantum dots as chemical building blocks: Elementary theoretical considerations. *ChemPhysChem* **2,** 20–36 (2001).
9. Chung, S. W., Markovich, G. & Heath, J. R. Fabrication and alignment of wires in two dimensions. *J. Phys. Chem. B* **102,** 6685–6687 (1998).
10. Bezryadin, A., Westervelt, R. M. & Tinkham, M. Self-assembled chains of graphitized carbon nanoparticles. *Appl. Phys. Lett.* **74,** 2699–2701 (1999).
11. Elteto, K., Lin, X. M. & Jaeger, H. M. Electronic transport in quasi-one-dimensional arrays of gold nanocrystals. *Phys. Rev. B* **71,** 205412 (2005).
12. Tang, Z. Y. & Kotov, N. A. One-dimensional assemblies of nanoparticles: Preparation, properties, and promise. *Adv. Mater.* **17,** 951–962 (2005).
13. Huang, J. X., Tao, A. R., Connor, S., He, R. R. & Yang, P. D. A general method for assembling single colloidal particle lines. *Nano Lett.* **6,** 524–529 (2006).
14. DeVries, G. A. *et al.* Divalent metal nanoparticles. *Science* **315,** 358–361 (2007).
15. Xia, Y. N., Yin, Y. D., Lu, Y. & McLellan, J. Template-assisted self-assembly of spherical colloids into complex and controllable structures. *Adv. Funct. Mater.* **13,** 907–918 (2003).
16. Cui, Y. *et al.* Integration of colloidal nanocrystals into lithographically patterned devices. *Nano Lett.* **4,** 1093–1098 (2004).
17. Kraus, T. *et al.* Nanoparticle printing with single-particle resolution. *Nature Nanotech.* **2,** 570–576 (2007).
18. Melosh, N. A. *et al.* Ultrahigh-density nanowire lattices and circuits. *Science* **300,** 112–115 (2003).
19. Zeng, H. *et al.* Magnetotransport of magnetite nanoparticle arrays. *Phys. Rev. B* **73,** 020402 (2006).
20. Yakimov, A. I. *et al.* Long-range Coulomb interaction in arrays of self-assembled quantum dots. *Phys. Rev. B* **61,** 10868–10876 (2000).
21. Beverly, K. C., Sampaio, J. F. & Heath, J. R. Effects of size dispersion disorder on the charge transport in self-assembled 2-D Ag nanoparticle arrays. *J. Phys. Chem. B* **106,** 2131–2135 (2002).
22. Yu, D., Wang, C. J., Wehrenberg, B. L. & Guyot-Sionnest, P. Variable range hopping conduction in semiconductor nanocrystal solids. *Phys. Rev. Lett.* **92,** 216802 (2004).
23. Zabet-Khosousi, A. & Dhirani, A. A. Charge transport in nanoparticle assemblies. *Chem. Rev.* **108,** 4072–4124 (2008).
24. Shklovskii, B. I. & Efros, A. L. in *Electronic Properties of Doped Semiconductors* (Springer, 1984).
25. Remacle, F., Beverly, K. C., Heath, J. R. & Levine, R. D. Conductivity of 2-D Ag quantum dot arrays: Computational study of the role of size and packing disorder at low temperatures. *J. Phys. Chem. B* **106,** 4116–4126 (2002).
26. Levin, E. I., Nguen, V. L., Shklovskii, B. I. & Efros, A. L. Coulomb gap and hopping electric conduction. Computer simulation. *Sov. Phys. JETP* **65,** 842–848 (1987).
27. Nguyen, V. D., Nguyen, V. L. & Dang, D. T. Variable range hopping in the Coulomb gap and gate screening in two dimensions. *Phys. Lett. A* **349,** 404–410 (2006).
28. Ancona, M. G. *et al.* Coulomb blockade in single-layer Au nanocluster films. *Phys. Rev. B* **64,** 033408 (2001).
29. Parthasarathy, R., Lin, X. M., Elteto, K., Rosenbaum, T. F. & Jaeger, H. M. Percolating through networks of random thresholds: Finite temperature electron tunneling in metal nanocrystal arrays. *Phys. Rev. Lett.* **92,** 076801 (2004).
30. Middleton, A. A. & Wingreen, N. S. Collective transport in arrays of small metallic dots. *Phys. Rev. Lett.* **71,** 3198–3201 (1993).
31. Elteto, K., Antonyan, E. G., Nguyen, T. T. & Jaeger, H. M. Model for the onset of transport in systems with distributed thresholds for conduction. *Phys. Rev. B* **71,** 064206 (2005).
32. Reichhardt, C. & Reichhardt, C. J. O. Temperature and a.c. effects on charge transport in arrays of metallic dots. *Phys. Rev. B* **68,** 165305 (2003).

Acknowledgements

The authors would like to thank Peigen Cao and Yue Zou (Caltech) for helpful discussions and Xingchen Ye and C. B. Murray (University of Pennsylvania) for providing the gold quantum dots. This work was supported by the Department of Energy, the National Science Foundation, and the MARCO Center for Advanced Materials and Devices.

Additional information

Supplementary information accompanies this paper at www.nature.com/naturenanotechnology. Reprints and permission information is available online at http://npg.nature.com/reprintsandpermissions/. Correspondence and requests for materials should be addressed to J.R.H.

nature nanotechnology

LETTERS

PUBLISHED ONLINE: 19 APRIL 2009 | DOI: 10.1038/NNANO.2009.82

Direct measurement of electrical conductance through a self-assembled molecular layer

F. Song[1,2], J. W. Wells[1,3], K. Handrup[1], Z. S. Li[4], S. N. Bao[2], K. Schulte[5†], M. Ahola-Tuomi[6], L. C. Mayor[5], J. C. Swarbrick[5†], E. W. Perkins[1,5], L. Gammelgaard[7] and Ph. Hofmann[1†*]

The self-assembly of organic molecules on surfaces is a promising approach for the development of nanoelectronic devices[1,2]. Although a variety of strategies have been used to establish stable links between molecules[2–11], little is known about the electrical conductance of these links. Extended electronic states, a prerequisite for good conductance, have been observed for molecules adsorbed on metal surfaces[12–16]. However, direct conductance measurements through a single layer of molecules are only possible if the molecules are adsorbed on a poorly conducting substrate. Here we use a nanoscale four-point probe[17] to measure the conductivity of a self-assembled layer of cobalt phthalocyanine on a silver-terminated silicon surface as a function of thickness. For low thicknesses, the cobalt phthalocyanine molecules lie flat on the substrate, and their main effect is to reduce the conductivity of the substrate. At higher thicknesses, the cobalt phthalocyanine molecules stand up to form stacks and begin to conduct. These results connect the electronic structure and orientation of molecular monolayer and few-layer systems to their transport properties, and should aid in the rational design of future devices.

Using a good metal as the substrate when studying the electric conductivity of molecular layers on surfaces is problematic because charge will flow through the metal rather than the molecules. A promising substrate for conductance measurements is the silver-terminated silicon surface (Ag/Si(111)–($\sqrt{3} \times \sqrt{3}$); hereafter referred to as Ag/Si), on which the ordered growth of molecular layers can be achieved[5,18–20] and where the substrate consists of a semimetallic surface on a semiconducting bulk. This approach has been chosen in the present paper. Figure 1a shows the measured conductance of the self-assembled layer of cobalt phthalocyanine (CoPc) thickness on the Ag/Si surface. To achieve surface sensitivity, the conductance was measured with a TiW-coated four-point probe with a contact spacing of only 500 nm (refs. 17, 21). Also presented are a model of the geometric structure of the film (Fig. 1c) and an image of the type of probe used in the conductance measurements (Fig. 1a, inset).

Two regions of different behaviour can be distinguished. Initially the conductance drops below that of the clean surface (shown in pink). Once the thickness is of the order of one monolayer, the conductance increases again and is eventually even higher than for the clean surface. We interpret this behaviour as the sum of the conductance through two channels: one through the Ag/Si layer and the other as direct conductance through the molecules.

The filled blue circle indicates a situation in which the surface is covered by one layer of flat-lying molecules, defining one monolayer, prepared by evaporating the CoPc molecules on an Ag/Si substrate held at elevated temperature (see preparation details). To facilitate a comparison with the main dataset it is necessary to assign a film thickness to this measurement; here we estimate that one monolayer is equal to 0.3 nm. The conductance for one monolayer prepared in this way agrees well with the main data series for which CoPc was deposited at room temperature, and corresponds to the minimum in the conductance.

There are two factors contributing to the lower conductance when CoPc is adsorbed on Ag/Si. The first is the introduction of disorder, which leads to a higher scattering rate for the carriers. The second, which we propose to be more significant, is related to an electron transfer from the surface to the CoPc molecules. Figure 2a shows X-ray photoelectron spectroscopy data from the cobalt 2*p* core level, for increasing thicknesses of CoPc on Ag/Si. For very small thicknesses, a low binding energy component dominates, whereas at higher thickness, the bulk component dominates. As a comparison, the cobalt 2*p* core level of lithium-doped (that is electron-doped) bulk CoPc is shown in Fig. 2b. Again, two contributions to each peak can be readily identified. For highly doped CoPc, the lower binding energy component dominates whereas for undoped and weakly doped samples, the higher (bulk) component dominates. Thus, by comparing these measurements with those of CoPc on Ag/Si, we propose that the first monolayer of CoPc on Ag/Si is strongly electron-doped.

Also from Fig. 2a, it is clear that the lower binding energy component does not vanish for thicknesses greater than one monolayer. Rather, the higher binding energy component appears in addition. This indicates that the interfacial monolayer of CoPc does not undergo any re-organization. Thus, for thicker films (in which the molecules form in the bulk α geometry), we understand that we still have a strongly electron-doped and flat-lying first monolayer, as shown schematically in Fig. 1c. We later show that the initially confined electron-doping of the first layer is then able to propagate freely through the entire film, leading to increased conductivity.

The photoemission measurements in Fig. 2c show the evolution of the valence band with increasing CoPc deposition. For very thin films (<1 monolayer), there is an increase of intensity close to the Fermi level, but no signature of a peak derived from the highest occupied molecular orbital (HOMO). This, combined with the observed lower conductivity in this thickness range, points towards a strong and localized bonding of the first-layer molecules to the substrate. For thicker films (>1 monolayer), the HOMO begins to appear in the spectra, and from its position and work function measurements (not shown), the

[1]Institute for Storage Ring Facilities (ISA) and Interdisciplinary Nanoscience Center (iNANO), University of Aarhus, 8000 Aarhus C, Denmark, [2]Department of Physics, Zhejiang University, Hangzhou, 310027 China, [3]Norwegian University of Science and Technology (NTNU), Trondheim, Norway, [4]Institute for Storage Ring Facilities (ISA), University of Aarhus, 8000 Aarhus C, Denmark, [5]School of Physics and Astronomy, University of Nottingham, Nottingham NG7 2RD, UK, [6]Department of Physics and Astronomy, University of Turku, 20014 Turku, Finland, [7]Capres A/S, 2800 Kgs. Lyngby, Denmark; †Present address: MAX-lab, Lund University, P.O. Box 118, 22100 Lund, Sweden (K.S.), European Synchrotron Radiation Facility, B.P. 220, 38043 Grenoble cedex 9, France (J.C.S.), Surface Science Research Centre, University of Liverpool, Liverpool L69 3BX, UK (Ph.H.). *e-mail: philip@phys.au.dk

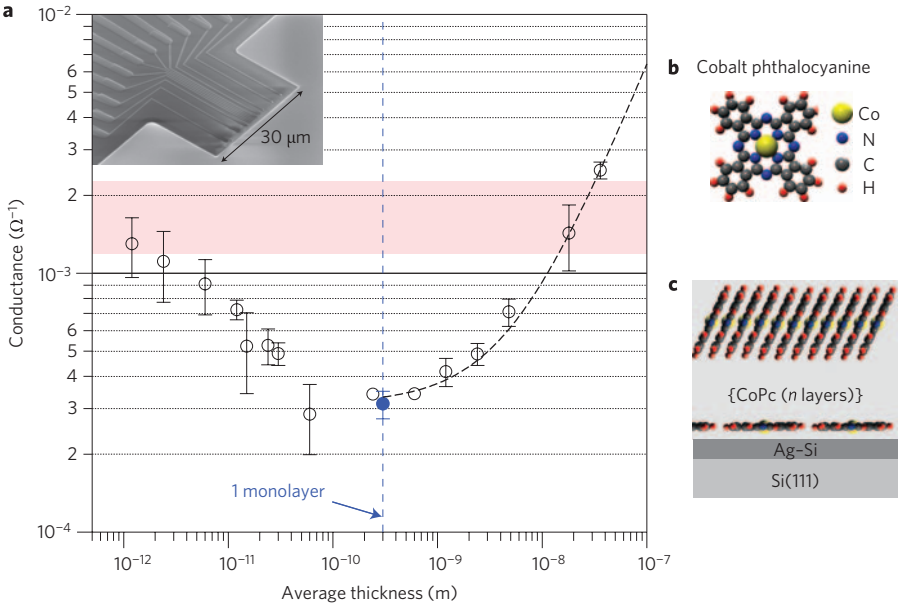

Figure 1 | Conductance, structure and model of CoPc. a, Room-temperature conductance of CoPc on ($\sqrt{3} \times \sqrt{3}$)Ag–Si(111) as a function of CoPc average film thickness. Open black circles show data for molecular deposition at room temperature, and the filled blue circle applies to a substrate temperature of 300 °C during deposition, resulting in a film thickness of exactly one monolayer[18], that is, one layer of flat-lying molecules. This thickness is marked by the dashed vertical line. The pink region indicates the conductance of the clean ($\sqrt{3} \times \sqrt{3}$)Ag–Si(111), including experimental uncertainty. The dashed line fitted to the >1 monolayer data points is the result of a conductance model for the system. The inset shows an image of the nanoscale probe used for the measurements[17]. **b**, Structure of a single CoPc molecule. **c**, Model for the geometric structure of CoPc on ($\sqrt{3} \times \sqrt{3}$)Ag–Si(111) based on NEXAFS results (see Supplementary Information). The first monolayer of molecules lies flat on the surface. In a multilayer system the molecular plane encloses an angle of 26° with the surface normal. Note that only the molecules in the first and last layer of a multilayer are shown.

band alignment at the CoPc interface can be estimated (as shown schematically for a thick film in Fig. 2d).

An electron transfer from the surface to the molecular layer can be expected to have a strong influence on the electronic structure and transport properties of the underlying Ag/Si surface termination. The electronic structure of Ag/Si is well known to be semimetallic: it is dominated by a free-electron-like surface state and the bottom of the surface state band is located precisely at the surface Fermi energy[22]. The state is thus unoccupied at zero temperature. At finite temperature it is occupied by thermally excited electrons. Electron-doping of the surface, for example by a small excess silver coverage, shifts the surface Fermi energy upwards, such that the number of free carriers on the surface[22] and the conductivity[23] are strongly enhanced. In the present case the opposite effect is observed; carriers are transferred to the CoPc layer and the surface conductivity drops, as expected.

Interestingly, the minimum conductance is reached when the surface is covered with one layer of flat-lying molecules (the blue filled circle in Fig. 1). This flat-lying structure is observed for thicknesses up to and including one monolayer using scanning tunnelling microscopy[18] and by near-edge X-ray absorption fine structure (NEXAFS) measurements (see Supplementary Information). Hence, an electron-doped but flat-lying layer does not possess a particularly high conductance.

For a higher thickness of CoPc the trend of decreasing conductance is reversed. This is interpreted as conductance through the molecular layer, induced by electron-doping combined with a structural change as more CoPc is deposited on the surface. Our NEXAFS data show that at thicknesses above one monolayer, the molecules start to stand more upright on the surface, forming a layer with stacked π-systems, with an angle of ~26° between the plane of the molecule and the surface normal (Fig. 1; see also Supplementary Information). This stacking is similar to the structure of the α phase of the phthalocyanines[24]. The assumption of an increased conductance through such a layer is consistent with the observations made for thick films of the CoPc α phase. Although bulk α CoPc is a wide-gap semiconductor, strongly increased conduction can be achieved by n-doping[25] (for a review of the electric properties of similar stacked π-systems see ref. 24).

If we assume that conductance of the thin CoPc film is proportional to its thickness x and given that x is smaller than the spacing between the contacts, we obtain

$$G_{\mathrm{CoPc}} = x\pi\sigma_{\mathrm{CoPc}}/\ln 2 \qquad (1)$$

where σ_{CoPc} is the bulk conductivity of doped CoPc (ref. 26). Because this film is deposited onto the Ag/Si surface, one can assume that the current can pass through both the silver and CoPc layers, and thus the measured conductance is approximated as the sum of the conductance of each layer. The combined conductance (G_{comb}) of the two layers is then given by

$$G_{\mathrm{comb}} = G_{\mathrm{Ag}} + x\pi\sigma_{\mathrm{CoPc}}/\ln 2 \qquad (2)$$

where G_{Ag} is the conductivity of the depleted silver monolayer (that is, the conductance of Ag/Si plus one ordered monolayer of CoPc, corresponding to the minimum in the conductance curve). From the data in Fig. 1, G_{Ag} is found to be $3.1 \pm 0.5 \times 10^{-4}\ \Omega^{-1}$, and by fitting the model parameter σ_{CoPc} to the data corresponding to $x \geq 0.3$ nm, σ_{CoPc} is found to be $1.3 \pm 0.5 \times 10^{4}\ \Omega^{-1}\ \mathrm{m}^{-1}$. The result of the model is depicted by the dashed black line in Fig. 1a and agrees very well with the data.

From the work of others[25] on potassium-doped films of ~20 nm thickness, one can also extract a value for σ_{CoPc} in an electron-doped system. This is found to be $\sim 0.3 \times 10^{4}\ \Omega^{-1}\ \mathrm{m}^{-1}$. This is in excellent agreement with our value, given the differences in the experiments and the possible role of defects such as grain boundaries in both our

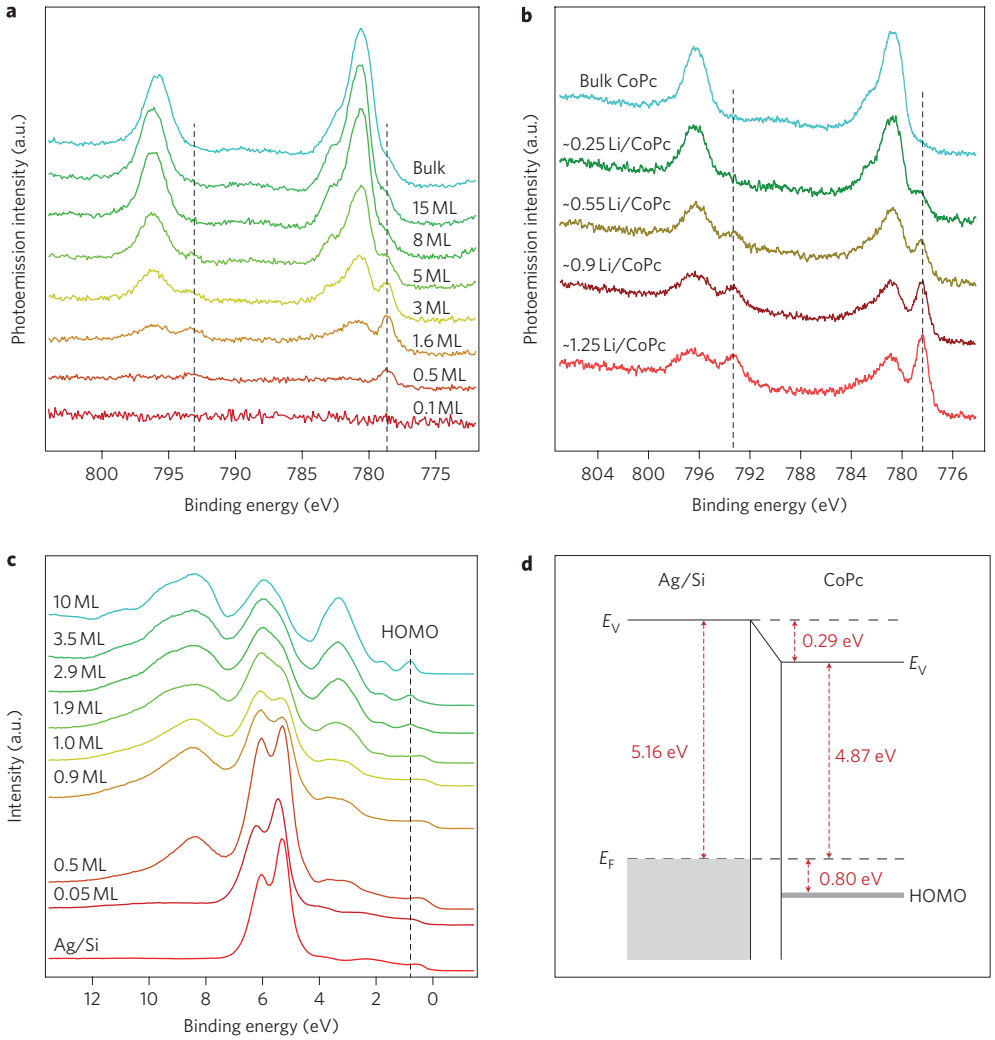

Figure 2 | Photoemission spectra from different CoPc systems. a, The cobalt 2*p* core level for CoPc on Ag/Si. The thickness is given in monolayers (ML). Both the bulk component and a smaller surface component (at lower binding energies, marked with dashed lines) are observed. **b**, The cobalt 2*p* core level for lithium-doped bulk CoPc with the number of lithium atoms per CoPc molecule indicated ($h\nu = 920$ eV). Two contributions per peak are present, and the lower binding energy components (marked by dashed lines) are stronger as the lithium doping is increased. **c**, The evolution of the valence band of CoPc on Ag/Si, with the position of the HOMO marked by a dashed vertical line. **d**, Schematic representation of the interface between Ag/Si and bulk CoPc.

work and in ref. 25. Note also that the agreement between our model and the data justifies our assumption of a thickness-independent film conductance. This is consistent with the physical picture of the doping presented above: we assume that charge transfer takes place from the substrate to the molecules in the first layer and this charge is then delocalized throughout the entire film. In thicker films the number of carriers will be smaller, but others have shown that the conductance of electron-doped CoPc is roughly constant over a wide doping range[25].

Note that the space charge layer under the surface does not play any role in the conductance. In the case of clean Ag/Si and for the same bulk doping as in the present study, it has been shown that the space charge layer contribution to the conductance is insignificant[27]. The adsorption of CoPc could, in principle, change the nature of the space charge layer such that it becomes more conductive, but the lower conduction in the initial stages of adsorption cannot be explained by the presence of the space charge layer.

In conclusion, we have shown how the electrical conductivity of self-assembled CoPc evolves as a function of thickness due to the interplay between the geometry and electronic structure of the self-assembled layer and substrate. Once the self-assembled layer reaches a certain thickness, the molecules stack, and conduction occurs mostly through the molecular layer rather than the substrate. For CoPc on Ag/Si, good conductivity is achieved only for films that exhibit π–π stacking between the molecules, and because there is no covalent chemical link between the molecules, the conduction is similar to that in a doped bulk crystal. This is encouraging for strategies that build molecular wires through π–π systems[7] and the general approach outlined here is promising for achieving similar progress for molecules lying on surfaces as for molecules placed between two electrodes[28,29].

Received 30 December 2008; accepted 17 March 2009; published online 19 April 2009

References

1. Joachim, C., Gimzewski, J. K. & Aviram, A. Electronics using hybrid-molecular and mono-molecular devices. *Nature* **408,** 541–548 (2000).
2. Barth, J. V., Costantini, G. & Kern, K. Engineering atomic and molecular nanostructures at surfaces. *Nature* **437,** 671–679 (2005).
3. Yokoyama, T., Yokoyama, S., Kamikado, T., Okuno, Y. & Mashiko, S. Selective assembly on a surface of supramolecular aggregates with controlled size and shape. *Nature* **413,** 619–621 (2001).
4. Lin, N., Dmitriev, A., Weckesser, J., Barth, J. V. & Kern, K. Real-time single-molecule imaging of the formation and dynamics of coordination compounds. *Angew Chem. Int. Ed.* **41,** 4779–4783 (2002).

5. Theobald, J. A., Oxtoby, N. S., Phillips, M. A., Champness, N. R. & Beton, P. H. Controlling molecular deposition and layer structure with supramolecular surface assemblies. *Nature* **424,** 1029–1031 (2003).
6. Barth, J. V., Weckesser, J., Lin, N., Dmitriev, A. & Kern, K. Supramolecular architectures and nanostructures at metal surfaces. *Appl. Phys. A* **76,** 645–652 (2003).
7. van Hameren, R. *et al.* Macroscopic hierarchical surface patterning of porphyrin trimers via self-assembly and dewetting. *Science* **314,** 1433–1436 (2006).
8. Grill, L. *et al.* Nano-architectures by covalent assembly of molecular building blocks. *Nature Nanotech.* **2,** 687–691 (2007).
9. Weigelt, S. *et al.* Covalent interlinking of aldehydes and amines on Au(111) under ultrahigh vacuum conditions. *Angew Chem. Int. Ed.* **46,** 9227–9230 (2007).
10. Yin, P., Choi, H. M. T., Calvert, C. R. & Pierce, N. A. Programming biomolecular self-assembly pathways. *Nature* **451,** 318–323 (2008).
11. Veld, M. I., Iavicoli, P., Haq, S., Amabilino, D. B. & Raval, R. Unique intermolecular reaction of simple porphyrins at a metal surface gives covalent nanostructures. *Chem. Commun.*, 1536–1538 (2008).
12. Netzer, F. P. Determination of structure and orientation of organic molecules on metal surfaces. *Vacuum* **41,** 49–53 (1990).
13. Graen, H. H., Neuber, M., Neumann, M., Odorfer, R. G. & Freund, H. J. Lateral interaction in ordered hydrocarbon overlayers — C–H band dispersion of adsorbed benzene. *Europhys. Lett.* **12,** 173–177 (1990).
14. Yang, W. *et al.* Band structure and Fermi surface of electron-doped C_{60} monolayers. *Science* **300,** 303–307 (2003).
15. Temirov, R., Soubatch, S., Luican, A. & Tautz, F. S. Free-electron-like dispersion in an organic monolayer film on a metal substrate. *Nature* **444,** 350–353 (2006).
16. Yamane, H. *et al.* Electronic structure at highly ordered organic/metal interfaces: Pentacene on Cu(110). *Phys. Rev. B* **76,** 165436 (2007).
17. Gammelgaard, L. *et al.* A complementary metal-oxide-semiconductor compatible monocantilever 12-point probe for conductivity measurements on the nanoscale. *Appl. Phys. Lett.* **93,** 093104 (2008).
18. Upward, M. D., Beton, P. H. & Moriarty, P. Adsorption of cobalt phthalocyanine on Ag terminated Si(111). *Surf. Sci.* **441,** 21–25 (1999).
19. Gustafsson, J. B., Zhang, H. M., Moons, E. & Johansson, L. S. O. Electron spectroscopy studies of PTCDA on Ag/Si(111)–$\sqrt{3} \times \sqrt{3}$. *Phys. Rev. B* **75,** 155413 (2007).
20. Gustafsson, J. B., Zhang, H. M. & Johansson, L. S. O. STM studies of thin PTCDA films on Ag/Si(111)–$\sqrt{3} \times \sqrt{3}$. *Phys. Rev. B* **75,** 155414 (2007).
21. Hofmann, Ph. & Wells, J. W. Surface-sensitive conductance measurements. *J. Phys. Condens. Matter* **21,** 013003 (2009).
22. Crain, J. N., Gallagher, M. C., McChesney, J. L., Bissen, M. & Himpsel, F. J. Doping of a surface band on Si(111)$\sqrt{3} \times \sqrt{3}$–Ag. *Phys. Rev. B* **72,** 045312 (2005).
23. Nakajima, Y., Uchida, G., Nagao, T. & Hasegawa, S. Two-dimensional adatom gas on the Si(111)–($\sqrt{3} \times \sqrt{3}$)–Ag surface detected through changes in electrical conduction. *Phys. Rev. B* **54,** 14134–14138 (1996).
24. Gould, R. D. Structure and electrical conduction properties of phthalocyanine thin films. *Coord. Chem. Rev.* **156,** 237–274 (1996).
25. Craciun, M. F. *et al.* Electronic transport through electron-doped metal phthalocyanine materials. *Adv. Mater.* **18,** 320–324 (2006).
26. Wells, J. W., Kallehauge, J. F. & Hofmann, Ph. Surface-sensitive conductance measurements on clean and stepped semiconductor surfaces: Numerical simulations of four point probe measurements. *Surf. Sci.* **602,** 1742–1749 (2008).
27. Wells, J. W., Kallehauge, J. F. & Hofmann, Ph. Thermal switching of the electrical conductivity of Si(111)($\sqrt{3} \times \sqrt{3}$)Ag due to a surface phase transition. *J. Phys. Condens. Matter* **19,** 176008 (2007).
28. Nitzan, A. & Ratner, M. A. Electron transport in molecular wire junctions. *Science* **300,** 1384–1389 (2003).
29. Wu, S. *et al.* Molecular junctions based on aromatic coupling. *Nature Nanotech.* **3,** 569–574 (2008).

Acknowledgements

We acknowledge useful discussions with P. Petersen, M. Balslev, J. Hansen, T. Hansen and P. Bøggild. Ph.H. thanks the Leverhulme Foundation and the Danish National Research Council for supporting a stay at the University of Liverpool. K.S. acknowledges support from an Anne McLaren Fellowship from the University of Nottingham, and support from the European Community – Research Infrastructure Action under the FP6 'Structuring the European Research Area' Programme (through the Integrated Infrastructure Initiative 'Integrating Activity on Synchrotron and Free Electron Laser Science'). M.A.-T. received funding through NANOCAGE (MEST-CT-2004-506854), a Marie Curie Early Stage Training Network, part of EC-FP6. We thank F. Bondino, E. Magnano and A. Preobrajenski for their help during synchrotron measurements.

Author contributions

F.S., J.W.W., S.N.B. and Ph.H. conceived the conductance experiments and F.S., K.H. and J.W.W. designed and performed these experiments and analysed the data. F.S., J.W.W., Z.S.L., K.S., M.A.-T., L.C.M., J.C.S. and E.W.P. performed the photoemission (PES) and NEXAFS experiments. K.S. analysed the NEXAFS and lithium-doping PES, F.S. the thickness-dependent PES. L.G. fabricated the nanoscale four-point probes. Ph.H., J.W.W. and K.S. co-wrote the initial draft of the paper. All authors discussed the results and significantly commented on the manuscript.

Additional information

Supplementary information accompanies this paper at www.nature.com/naturenanotechnology. Reprints and permission information is available online at http://npg.nature.com/reprintsandpermissions/. Correspondence and requests for materials should be addressed to Ph.H.

nature nanotechnology

LETTERS

PUBLISHED ONLINE: 26 APRIL 2009 | DOI: 10.1038/NNANO.2009.92

Broadband all-photonic transduction of nanocantilevers

Mo Li, W. H. P. Pernice and H. X. Tang*

Nanoelectromechanical systems[1,2] based on cantilevers have consistently set records for sensitivity in measurements of displacement[3], force[4] and mass[3,5,6] over the past decade. Continued progress will require the integration of efficient transduction on a chip so that nanoelectromechanical systems may be operated at higher speeds and sensitivities. Conventional electrical schemes have limited bandwidth[7,8], and although optical methods[9,10] are fast, they are subject to the diffraction limit. Here, we demonstrate the integration of nanocantilevers on a silicon photonic platform with a non-interferometric transduction scheme that avoids the diffraction limit by making use of near-field effects in optomechanical interactions[11]. The use of a non-interferometric method means that a coherent light source is not required, making the monolithic integration of optomechanical systems with on-chip light sources feasible. We further demonstrate optomechanical multiplexing of an array of ten nanocantilevers with a displacement sensitivity of 40 fm Hz$^{-1/2}$.

Nanoelectromechanical systems (NEMS) mainly use electrical methods for device transduction, but the operation bandwidth is usually limited by unavoidable parasitic coupling and the considerable readout impedance mismatch[8]. Optical methods have demonstrated superior sensitivity and can, in principle, achieve unlimited bandwidth[9,10]. However, free-space implementations of optical methods are not suitable for integration because the diffraction limit causes the transduction efficiency to decrease as the device dimensions are scaled below the optical wavelength.

A nanophotonic platform allows various optical components—waveguides[12], modulators[13], light sources[14] and detectors[15]—to be integrated at chip-scale level. The characteristic size of the modes in the waveguides matches the typical dimensions of nanomechanical devices, making it feasible to integrate nanomechanical devices into a nanophotonic platform to take advantage of both the speed and sensitivity of optical methods. As a result, the diffraction limit and the difficulties associated with optical alignment can be completely avoided. Several groups have demonstrated mechanical motion sensing using end-coupled microscale optical waveguides made of indium phosphide[16], SU-8[17] and glass[18]. A similar readout scheme has been applied to a silicon-based device[19]. However, actuation of these devices still relies on electrical methods, so the limitations imposed by conventional methods remain.

Previously, we have demonstrated efficient transduction of nanomechanical beam resonators embedded in a photonic circuit with an on-chip interferometer for displacement sensing[11]. This phase-sensitive detection scheme works well for doubly clamped beams because light can pass through without suffering significant loss. However, the same principle does not apply to cantilevers, which represent a more important class of NEMS devices for practical metrology and sensing applications. In this work, we demonstrate all-photonic transduction of nanomechanical cantilevers in a non-interferometric setting. By avoiding interferometric schemes (or optical cavities), the overall device footprint is reduced to a minimum. More importantly, the detection is inherently broadband and does not require coherent light sources.

The device configuration is shown in the optical microscope image of Fig. 1a, in which a pair of end-to-end coupled cantilevers is part of a single-mode photonic waveguide, with a nanoscale gap separating the two. Light passing through the first cantilever waveguide tunnels through the gap and is then collected by the receiving cantilever waveguide. The motion of the cantilever modulates the total transmission through the circuit and is then measured in the transmitted optical signal. The photonic circuit is realized on a silicon-on-insulator (SOI) platform. As shown in Fig. 1a, the device consists of two input/output grating couplers, two multimode interference (MMI) couplers and 500-nm-wide single-mode photonic waveguides. The cantilevers are released by wet chemical etching and separated by ~350 nm from the substrate (Fig. 1b). Both cantilevers are 3 μm long with a 200 nm gap between them. This relatively small gap (compared with the optical wavelength) causes an estimated optical loss of ~3 dB as predicted by numerical simulations[16]. The total insertion loss of the device is −24 dB, with most of the loss occurring at the input/output grating couplers (−10 ± 1 dB each).

The transmission from one cantilever to the other can be expressed by

$$T = \left| \int_{-\infty}^{\infty} \phi_i(x,y,z)\,\phi_o(x,y,z+\Delta z)\,\mathrm{d}x\,\mathrm{d}y \right|^2$$

where ϕ_i and ϕ_o are the normalized mode functions of the input and output cantilever waveguides. The out-of-plane relative motion of the two cantilevers alters the offset Δz between the waveguides and therefore modulates the total transmission T of the system. This effect is analysed using finite-difference time-domain (FDTD) simulations as presented in Fig. 1c. It is apparent that the transmission decreases when the left cantilever is offset vertically relative to the right cantilever; the transmission is maximal at zero relative displacement. The slight asymmetry in the transmission profile in Fig. 1c is due to the additional coupling of the optical fields in the waveguide towards the substrate. The linear displacement detection responsivity $R_0 = \partial T/\partial z$ is then proportional to the derivative of the transmission with respect to the relative displacement Δz. As shown in Fig. 1d, the responsivity is minimal at $\Delta z \approx 0$ and maximal at $\Delta z \approx 100$ nm. Note that, in principle, x^2 detection, which represents a best measure of the oscillator's energy state[20], can be achieved with perfectly aligned cantilevers ($\Delta z = 0$). For the linear displacement detection studied here the cantilevers have to be offset from one another. An offset of ~25 nm, due to the different residual surface stress on the two cantilevers, is present in our case, as evident from the scanning electron microscopy (SEM)

Department of Electrical Engineering, Yale University, New Haven, Connecticut 06511, USA. *e-mail: hong.tang@yale.edu

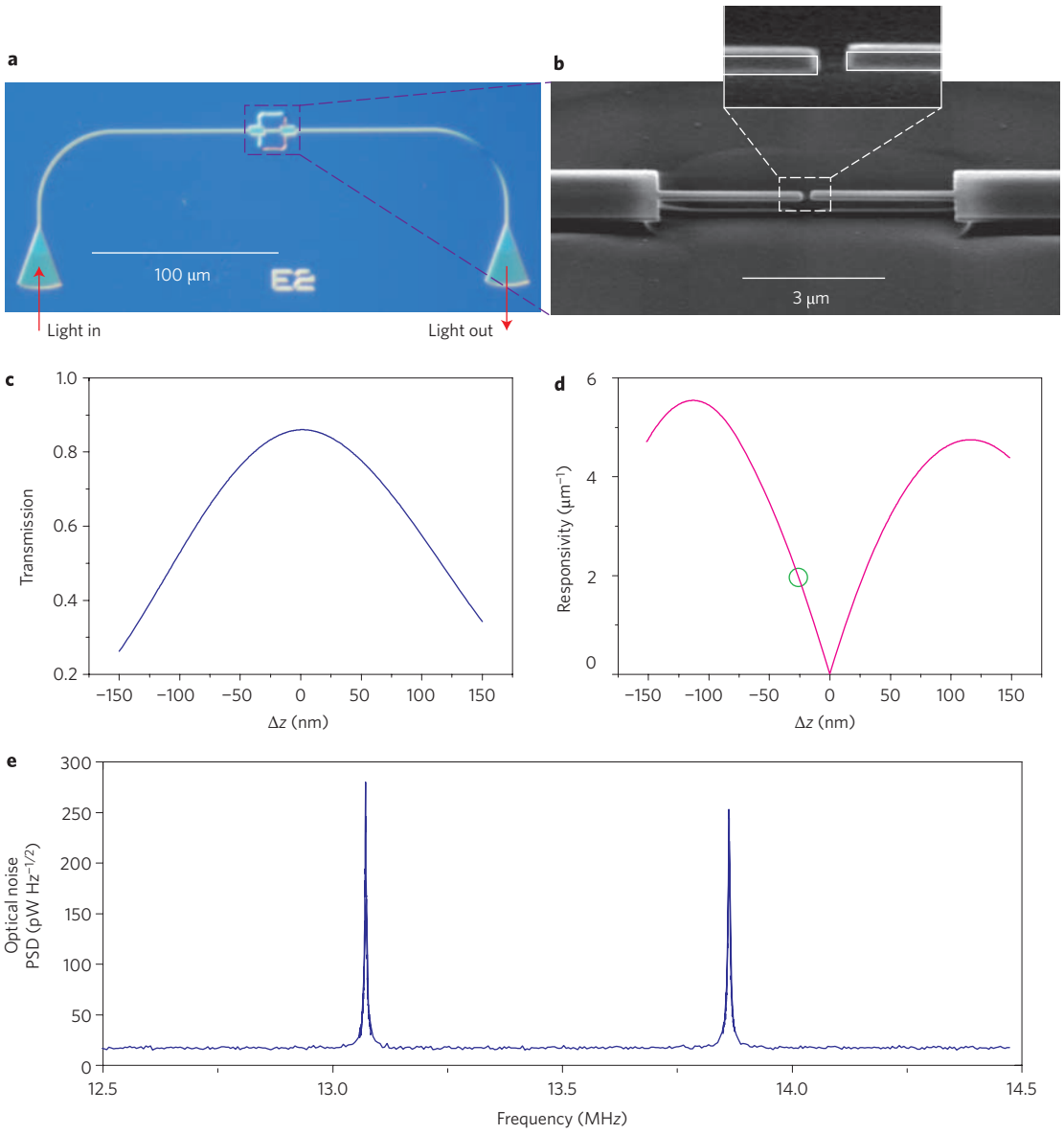

Figure 1 | End-to-end coupled waveguide nanocantilevers. a, Optical microscope image of the photonic circuitry, showing the nanomechanical cantilevers in the centre and the two grating couplers at the ends of the waveguides. **b**, SEM image of the end-to-end coupled waveguide nanocantilever devices. The inset shows how the ends of the nanocantilevers are offset by ~25 nm in the out-of-plane direction. The waveguide cross-section is 500 × 110 nm^2. **c**,**d**, Simulation results of the transmission (**c**) and responsivity (**d**) of the device versus the out-of-the-plane relative displacement of the two aligned cantilevers. The green marker shows the initial 25 nm offset between the cantilevers. **e**, Measured noise power spectral density (PSD) of the optical detection signal, showing the room-temperature thermomechanical resonance peaks of both cantilevers.

image of the devices in Fig. 1b. From the result in Fig. 1d, a detection responsivity of ~2.0 μm^{-1} is expected. The precise value of this offset is not important in our displacement measurement, as the actual value of responsivity can be calibrated independently through thermomechanical noise measurements[21]. However, this offset can be engineered to desired values, as we show later, by depositing another layer of material with low optical loss to introduce additional stress to the cantilevers.

We assessed the sensitivity of the system by measuring the thermomechanical motion of the devices. In our setup, light is coupled through the grating coupler into the device which is mounted in a vacuum chamber. A tuneable diode laser (TDL) is first used in CW mode for detection and its transmission through the circuit is measured with a high-speed photodetector. The frequency response and noise spectrum of the photodetector signal is then measured with a network/spectrum analyser. Figure 1e shows the noise power spectrum density (PSD) of the transmitted detection signal over a wide frequency range. The applied input optical power is 50 mW, and the calibrated power on the first cantilever is ~7.5 mW. After propagating through the circuit, 200 μW power is received at the photodetector. The spectrum shows two prominent peaks at 13.07 and 13.86 MHz, corresponding to the out-of-plane fundamental mechanical resonances of the two cantilevers. The difference of their resonance frequency can be attributed to the different undercut at the clamping point. The two resonances show very similar quality factors of ~4,500 in vacuum. The spectral density of the thermomechanical displacement noise at resonance frequency is $S_z^{1/2} = \sqrt{[4k_B T_0 Q/(m\omega_0^3)]}$, where k_B is the Boltzmann

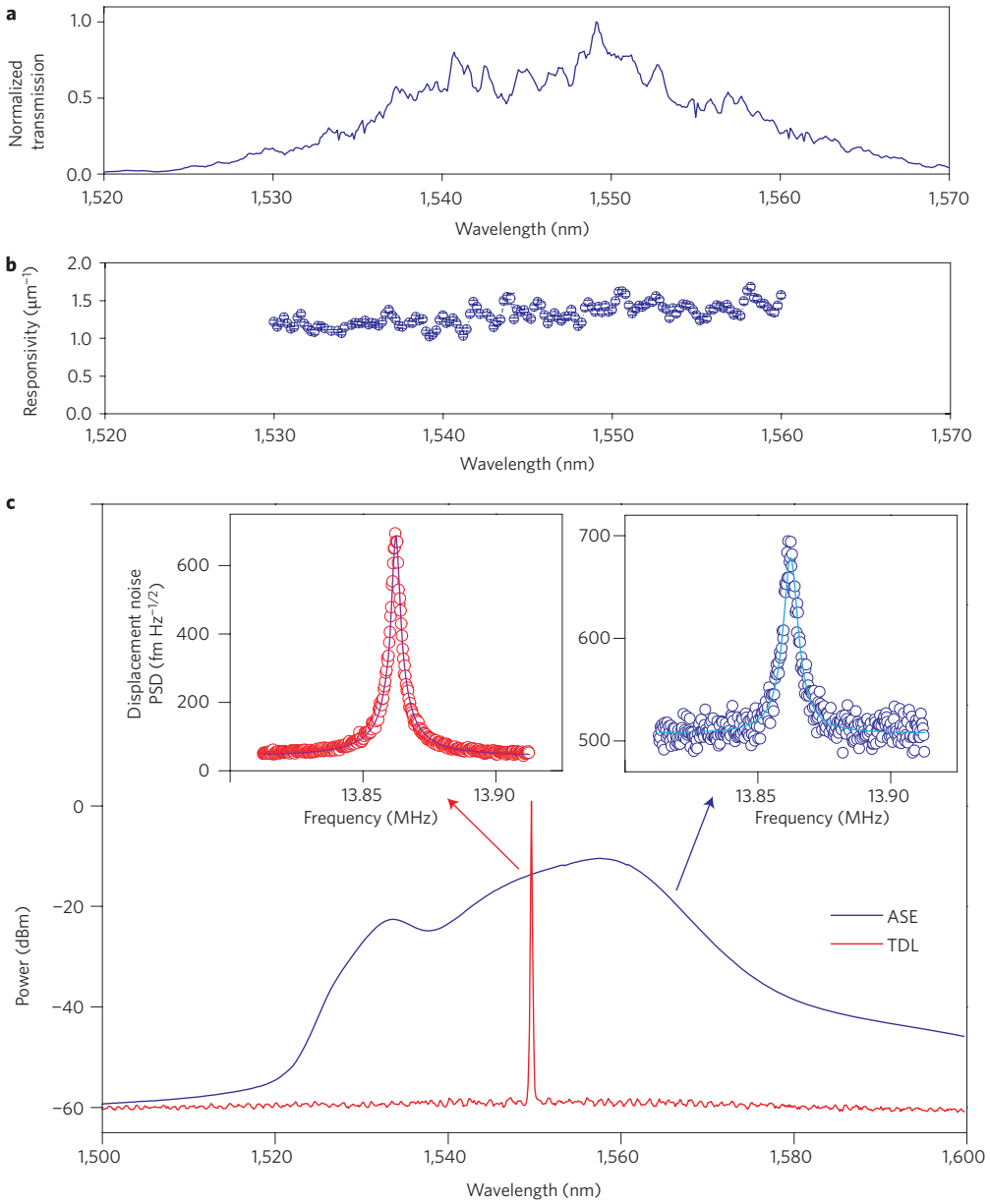

Figure 2 | Non-interferometric detection scheme. a, Transmission spectrum of the device, showing only weak interference effects. **b**, Displacement responsivity plotted against the detection wavelength. The variation of the responsivity with wavelength is much smaller than that observed with interferometric detection methods. **c**, Optical spectrum of the amplified spontaneous emission (ASE) source (blue) and a tuneable diode laser (TDL) at a wavelength of 1,550 nm (red). The ASE spectrum has a spectral width of ~30 nm, corresponding to a coherence length of 75 μm. Left inset: thermomechanical noise spectrum of the right cantilever measured using the TDL source, with a displacement sensitivity of 40 fm $Hz^{-1/2}$. Right inset: when the ASE source is used, an excess of intensity noise causes the displacement sensitivity to deteriorate to 500 fm $Hz^{-1/2}$.

constant, T_0 the absolute temperature (300 K), Q the mechanical quality factor, ω_0 the angular resonance frequency and m the modal mass of the cantilever. By comparing the expected displacement noise with the measured noise spectrum, we can determine the displacement responsivity of the system, which is found to be 1.6 μm^{-1}, close to the numerical prediction at ~25 nm offset (Fig. 1d).

It is important to stress that the end-to-end coupling detection scheme demonstrated here is fundamentally different from interferometric schemes as, for example, implemented in ref. 11. Because an interferometer measures the change of the optical phase, its sensitivity depends on the wavelength of the probing light—the responsivity reaches a maximum at the quadrature wavelengths and vanishes at the node and anti-node wavelengths. Interferometric methods are also susceptible to the phase noise of the laser source and thus require coherent laser light sources with low phase noise to achieve high sensitivity. Moreover, when applied to sensing applications, interferometric methods are vulnerable to environmental effects such as temperature changes. In contrast, the end-to-end coupling scheme directly converts the displacement to amplitude modulation. Therefore its sensitivity is independent of the probing wavelength and is less affected by the environment.

To demonstrate the non-interferometric nature of our detection scheme we determined the responsivity of the system as a function of the probing wavelength. Figure 2a presents the transmission

spectrum of the device. Unlike in devices designed for interferometric detection, only small ripples resulting from weak internal reflection between the grating couplers can be seen. Figure 2b shows the corresponding displacement responsivity R_0. In the 30-nm wavelength span only small variations are present, thus indicating the non-interferometric characteristics of the method. This is in strong contrast to interferometric schemes, where we would find distinct fringes[11].

As a proof of principle, we replaced the laser source with an amplified spontaneous emission (ASE) source generated with an erbium-doped fibre amplifier (EDFA). The typical optical spectrum of the ASE source is shown in Fig. 2c, which has a spectral width of more than 30 nm. Its coherence length is only 75 μm, much shorter than the total length of the waveguide in the device. At 50 mW ASE input power, the power on the first cantilever is estimated to be 3.8 mW, taking into account the grating coupler and polarization loss. As shown in the right inset of Fig. 2c, the thermomechanical noise PSD of the cantilever is measured with good signal-to-noise ratio. The excess noise is mostly attributed to the well-known intensity noise in the ASE source. As a result, the achieved displacement measurement sensitivity has deteriorated to 500 fm $Hz^{-1/2}$ from the 40 fm $Hz^{-1/2}$ obtained with a low-noise tuneable laser source at the same input power (Fig. 2c, right inset). This demonstration proves the feasibility of replacing the tuneable laser diode with more flexible broadband light sources in chip-scale NEMS sensing systems.

We then demonstrated the driven response of the nanomechanical cantilevers by applying another actuation laser at 1,540 nm with the detection laser at 1,550 nm. Amplitude modulation of the actuation laser intensity generates a dynamic gradient optical force on the cantilevers and sets them into motion[11]. The response of the devices in amplitude and phase is shown in Fig. 3, displaying exceptional signal quality. The two cantilevers show different resonant amplitudes. This is expected because the actuating optical powers on the two cantilevers are different due to the loss (~3 dB) occurring at the gap between them. Thus we can attribute the resonance peak at 13.07 MHz to the cantilever on the left; its amplitude is about twice that of the one at 13.87 MHz, because the light is launched into the devices from the left coupler. Using the calibrated responsivity R_0 of the system, the vibration amplitude can be determined from the measured signal. In Fig. 3b, the resonant response of the left cantilever is measured as a function of the laser modulation amplitude, showing a linear relationship.

Many sensing applications demand multiplexed integration of a large array of NEMS devices[22,23]. A photonic waveguide can be used to manipulate light in multiple paths with very low crosstalk. Therefore it is possible to integrate a multitude of NEMS devices into a single photonic circuit. For example, the input and output MMI structures in Fig. 1b can be converted into a $1 \times N$ splitter and a $N \times 1$ combiner, diverting the probing light to N independent cantilever pairs. Figure 4a shows the FDTD simulation result of such a design. The light is first split evenly by a 1×5 MMI coupler to five pairs of cantilevers and then refocused by a 5×1 MMI coupler into the output waveguide. In the optimized device, the output combiner has a different length from the input splitter in order to achieve maximum transmission. An SEM image of this device is shown in Fig. 4b. The length of the ten cantilevers varies from 2.5 to 3.5 μm. Compared to the device with a single pair of cantilevers, this multiplexed configuration adds less than 1 dB extra optical loss to the photonic circuit. To demonstrate the performance of the device, the noise PSD of the transmitted optical signal is measured with 100 mW input laser power at 1,550 nm. Ten thermomechanical peaks, corresponding to the mechanical resonance of each cantilever, can be clearly observed in Fig. 4c. The relative signal-to-noise ratio is lower than the result in Fig. 1e because the optical power on each cantilever pair is reduced by a factor of five.

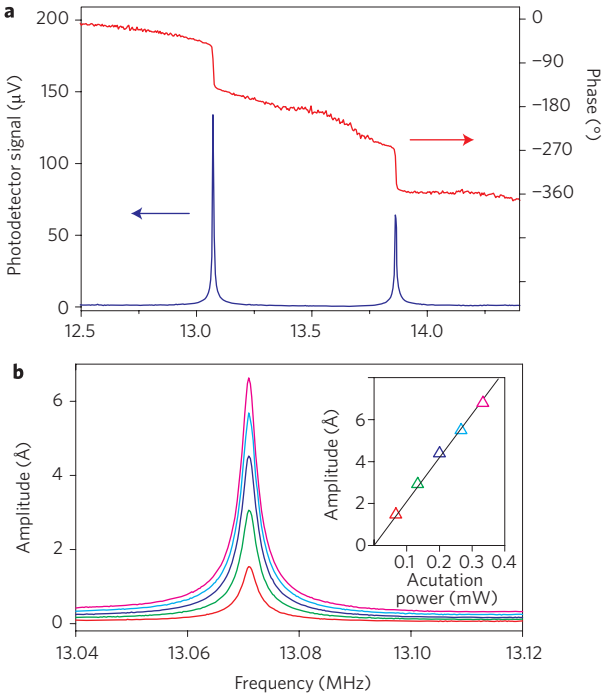

Figure 3 | All-optical operation of the nanocantilevers. a, The driven response of the two nanocantilevers actuated by the gradient optical force generated by an amplitude modulated laser. The phase response shows a clear 180° change at each resonance. **b**, The amplitude of the motion of the left cantilever as a function of frequency for five different actuation optical powers. The inset shows that the resonance amplitude increases linearly with the actuation optical power.

The mechanical resonance frequencies of the cantilevers vary from 11 to 21 MHz, showing the linear dependence on the inverse square of the cantilever lengths, as expected from simple beam theory.

The optical actuation and detection methods described above both have broad bandwidth. For practical sensing applications the demonstrated non-interferometric detection method is especially attractive because integrated low-cost light sources such as light-emitting diodes and laser diodes can be used. With the future development of other integrated photonic components such as light sources, modulators and detectors, an entire coupled nanomechanical-nanophotonic system can be envisioned on a single chip. Such a compact, robust and scalable system with high sensitivity will find a wide range of applications, including chemical and biological sensing[22,23] and optical signal processing[24].

Methods

Device details. The devices were fabricated on silicon-on-insulator wafers manufactured by Soitec with a 110-nm silicon layer and 3 μm of buried oxide. The devices were patterned by electron-beam lithography (Vistec VB-6 at Cornell Nanofabrication Facility) and a plasma dry etching process. The cantilevers were released from the substrate using a photo-lithographically patterned mask and buffered oxide etching.

A thin layer of silicon dioxide was deposited on the multiplexed cantilever arrays to induce surface stress. This process vertically offsets the cantilever pairs and optimizes the detection responsivity. Because the lengths of the cantilevers are different, the cantilevers have different spring constants. Thus, under similar stresses, the cantilevers are bent to a different extent and offset vertically from each other.

When designing the multi-port MMI splitter and combiner we optimized the total transmission of the device. As a result, the length of the input MMI splitter was different from the output combiner. The widths of the cantilever waveguides were also slightly adjusted to add a proper phase difference to evenly distribute the light in the optical paths.

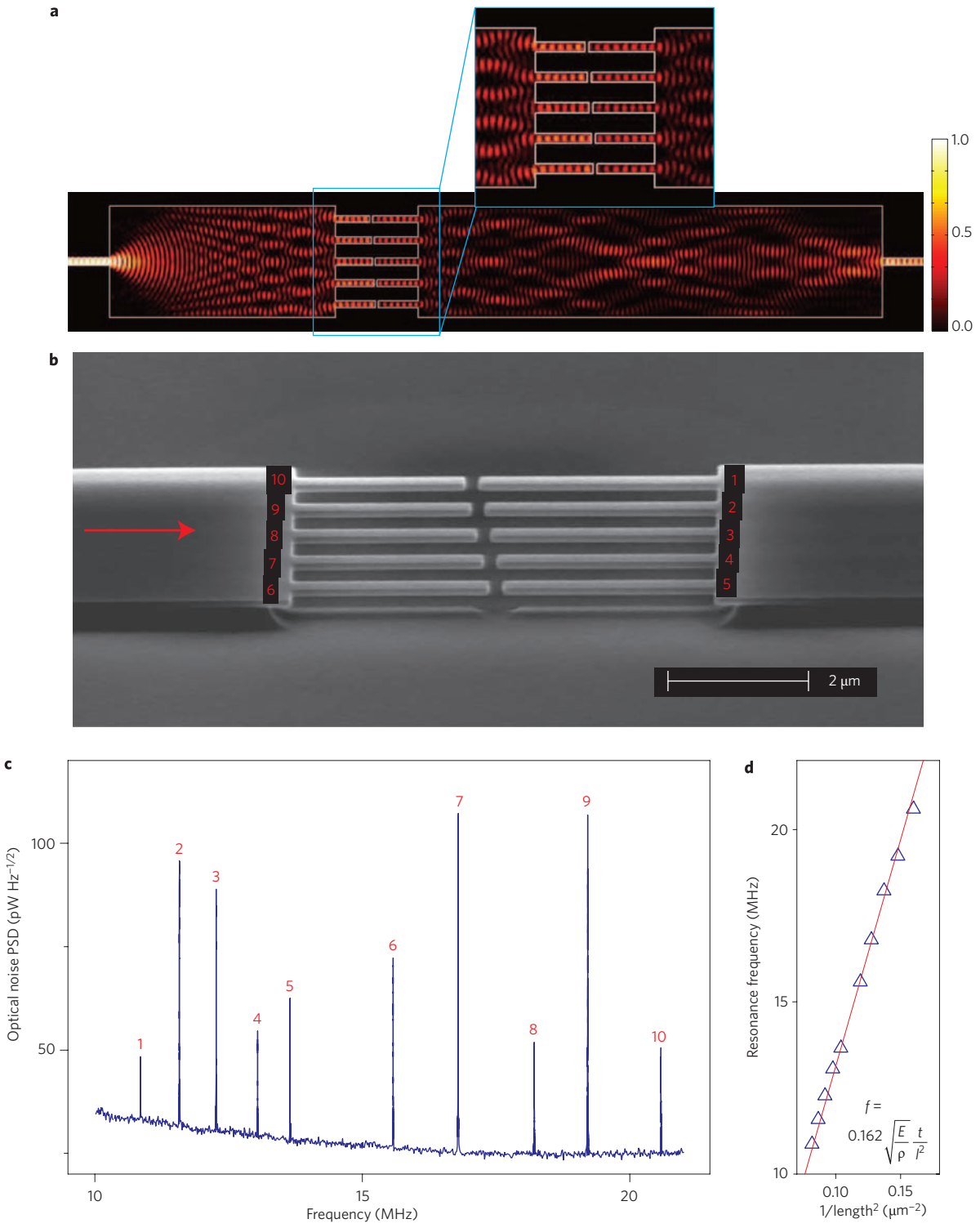

Figure 4 | Multiplexed integration of ten cantilevers in a photonic circuit. a, FDTD simulation results showing the normalized light intensity of ten cantilevers coupled between a 1 × 5 multi-mode interference (MMI) splitter and a 5 × 1 MMI combiner. **b**, A SEM of the device. The gap between the cantilevers is 200 nm. **c**, The noise power spectrum density (PSD) of the transmitted optical signal, showing the ten thermomechanical resonance noise peaks of the cantilevers. **d**, The mechanical resonance frequency is inversely proportional to the square of the cantilever length.

Measurement setup. The devices were measured in a vacuum chamber with a base pressure of 10^{-5} torr. Light was coupled into the device using an array of cleaved single-mode polarization-maintaining fibres aligned to the grating couplers. The typical coupling efficiency was 10% (or −10 dB). Two tuneable diode lasers (Santec TSL-210 and HP 8618F) were used as the actuation and detection light sources, respectively. The actuation laser was amplitude-modulated by a $LiNbO_3$ high-speed modulator (Lucent 2623NA). The noise spectrum and driven response of the device were measured with a photodetector (New Focus 1611) and analysed with a network/spectrum analyser (HP 4195A). The ASE source was generated with a cascaded four-stage EDFA (Highwave Optical Technologies), pumped at 980 nm.

The displacement sensitivity was calibrated by measuring the thermomechanical noise spectrum of the device. The measurement noise floor was limited by the

photodetector noise. At measurement frequencies away from the mechanical resonance of the cantilevers, the thermal vibration of both cantilevers was below the measurement noise level and thus could be neglected in determining the measurement sensitivity[25].

Received 15 February 2009; accepted 25 March 2009; published online 26 April 2009

References

1. Roukes, M. Nanoelectromechanical systems face the future. *Phys. World* **14,** 25–31 (February 2001).
2. Craighead, H. G. Nanoelectromechanical systems. *Science* **290,** 1532–1535 (2000).
3. Li, M., Tang, H. X. & Roukes, M. L. Ultra-sensitive NEMS-based cantilevers for sensing, scanned probe and very high-frequency applications. *Nature Nanotech.* **2,** 114–120 (2007).
4. Rugar, D., Budakian, R., Mamin, H. J. & Chui, B. W. Single spin detection by magnetic resonance force microscopy. *Nature* **430,** 329–332 (2004).
5. Ilic, B. *et al.* Attogram detection using nanoelectromechanical oscillators. *J. Appl. Phys.* **95,** 3694–3703 (2004).
6. Yang, Y. T., Callegari, C., Feng, X. L., Ekinci, K. L. & Roukes, M. L. Zeptogram-scale nanomechanical mass sensing. *Nano Lett.* **6,** 583–586 (2006).
7. Huang, X. M. H., Zorman, C. A., Mehregany, M. & Roukes, M. L. Nanodevice motion at microwave frequencies. *Nature* **421,** 496 (2003).
8. Truitt, P. A., Hertzberg, J. B., Huang, C. C., Ekinci, K. L. & Schwab, K. C. Efficient and sensitive capacitive readout of nanomechanical resonator arrays. *Nano Lett.* **7,** 120–126 (2007).
9. Carr, D. W., Evoy, S., Sekaric, L., Craighead, H. G. & Parpia, J. M. Measurement of mechanical resonance and losses in nanometer scale silicon wires. *Appl. Phys. Lett.* **75,** 920–922 (1999).
10. Azak, N. O. *et al.* Nanomechanical displacement detection using fiber-optic interferometry. *Appl. Phys. Lett.* **91,** 093112 (2007).
11. Li, M. *et al.* Harnessing optical forces in integrated photonic circuits. *Nature* **456,** 480–484 (2008).
12. Vlasov, Y. A. & McNab, S. J. Losses in single-mode silicon-on-insulator strip waveguides and bends. *Opt. Express* **12,** 1622–1631 (2004).
13. Xu, Q. F., Schmidt, B., Pradhan, S. & Lipson, M. Micrometre-scale silicon electro-optic modulator. *Nature* **435,** 325–327 (2005).
14. Rong, H. *et al.* A continuous-wave Raman silicon laser. *Nature* **433,** 725–728 (2005).
15. Kang, Y. *et al.* Monolithic germanium/silicon avalanche photodiodes with 340 GHz gain–bandwidth product. *Nature Photon.* **3,** 59–63 (2009).
16. Pruessner, M. W. *et al.* End-coupled optical waveguide MEMS devices in the indium phosphide material system. *J. Micromech. Microeng.* **16,** 832–842 (2006).
17. Maria, N., Dan, A. Z., Montserrat, C., Jorg, H. & Anja, B. Integrated optical readout for miniaturization of cantilever-based sensor system. *Appl. Phys. Lett.* **91,** 103512 (2007).
18. Zinoviev, K., Dominguez, C., Plaza, J. A., Busto, V. J. C. & Lechuga, L. M. A novel optical waveguide microcantilever sensor for the detection of nanomechanical forces. *J. Lightwave Technol.* **24,** 2132–2138 (2006).
19. De Vlaminck, I. *et al.* Detection of nanomechanical motion by evanescent light wave coupling. *Appl. Phys. Lett.* **90,** 233116 (2007).
20. Thompson, J. D. *et al.* Strong dispersive coupling of a high-finesse cavity to a micromechanical membrane. *Nature* **452,** 72–75 (2008).
21. Walters, D. A. *et al.* Short cantilevers for atomic force microscopy. *Rev. Sci. Instrum.* **67,** 3583–3590 (1996).
22. Zhang, J. *et al.* Rapid and label-free nanomechanical detection of biomarker transcripts in human RNA. *Nature Nanotech.* **1,** 214–220 (2006).
23. Ndieyira, J. W. *et al.* Nanomechanical detection of antibiotic mucopeptide binding in a model for superbug drug resistance. *Nature Nanotech.* **3,** 691–696 (2008).
24. Vlasov, Y., Green, W. M. J. & Xia, F. High-throughput silicon nanophotonic wavelength-insensitive switch for on-chip optical networks. *Nature Photon.* **2,** 242–246 (2008).
25. Rugar, D., Mamin, H. J. & Guethner, P. Improved fiber-optic interferometer for atomic force microscopy. *Appl. Phys. Lett.* **55,** 2588–2590 (1989).

Acknowledgements

H.X.T. acknowledges a career award from National Science Foundation (NSF). W.H.P.P. acknowledges support from the Alexander-von-Humboldt postdoctoral fellowship programmes. The authors thank M. Hochberg and T. Baehr-Jones for help with the design of the grating couplers. The devices were fabricated at Yale Center for Microelectronic Materials and Structures and the NSF sponsored Cornell Nanoscale Facility. Part of the funding was provided by a seed grant offered by Yale Institute for Nanoscience and Quantum Information.

Additional information

Reprints and permission information is available online at http://npg.nature.com/reprintsandpermissions/. Correspondence and requests for materials should be addressed to H.X.T.

nature nanotechnology

LETTERS

PUBLISHED ONLINE: 26 APRIL 2009 | DOI: 10.1038/NNANO.2009.89

Trilayer graphene is a semimetal with a gate-tunable band overlap

M. F. Craciun[1]*†, S. Russo[1,2]*†, M. Yamamoto[1], J. B. Oostinga[2,3], A. F. Morpurgo[3] and S. Tarucha[1,4,5]

Graphene-based materials are promising candidates for nanoelectronic devices[1–14] because very high carrier mobilities can be achieved without the use of sophisticated material preparation techniques[1]. However, the carrier mobilities reported for single-layer and bilayer graphene are still less than those reported for graphite crystals at low temperatures, and the optimum number of graphene layers for any given application is currently unclear, because the charge transport properties of samples containing three or more graphene layers have not yet been investigated systematically[1]. Here, we study charge transport through trilayer graphene as a function of carrier density, temperature, and perpendicular electric field. We find that trilayer graphene is a semimetal with a resistivity that decreases with increasing electric field, a behaviour that is markedly different from that of single-layer and bilayer graphene. We show that the phenomenon originates from an overlap between the conduction and valence bands that can be controlled by an electric field, a property that had never previously been observed in any other semimetal. We also determine the effective mass of the charge carriers, and show that it accounts for a large part of the variation in the carrier mobility as the number of layers in the sample is varied.

Electron and hole mobilities as high as 1×10^4 cm^2 V^{-1} s^{-1} are routinely observed in single and bilayer graphene on substrates[2–7,9–12], and values as high as 2×10^5 cm^2 V^{-1} s^{-1} have been reported for suspended graphene[15]. However, carrier mobilities in excess of 1×10^6 cm^2 V^{-1} s^{-1} have been measured in graphite at low temperature[16–18], and it is natural to ask if the carrier mobility can be increased by simply increasing the number of graphene layers in the material. It is also important to understand how the general electronic properties of graphene-based materials evolve from those of graphene to those of graphite as the number of layers is increased. Note that the low-energy electronic properties of samples containing three or more graphene layers depend on a large number of parameters, and theorists have been unable to agree about the details of the electronic structure (see, for example, refs 19–23). Here, as a first step to address these issues, we investigate charge transport through trilayer graphene, which is the thinnest graphene-based system with a tight-binding Hamiltonian that includes all the transfer integrals that are needed to describe the band structure of graphite[19–23].

The fabrication of trilayer-based nanoelectronic devices relies on micromechanical cleaving of graphite crystals (see ref. 1 and Methods for details), which enables the deposition of few-layer graphene on top of an oxidized silicon substrate. The layer thickness was identified by analysing the shift in green intensity under an optical microscope[10] (see Supplementary Information). Care was taken to select flakes formed by regions of different thickness, and to fabricate devices on each region (Fig. 1a), only a few micrometres apart. The spatial proximity of devices fabricated on the same flake ensures that the disorder induced by the substrate has comparable magnitude, which facilitates a direct comparison of the electrical properties of single-layer, bilayer and trilayer graphene.

The field-effect behaviour in trilayer graphene devices manifests itself in the dependence of the square resistance ($R_\square$) and the Hall coefficient (R_H) on the voltage V_{bg} applied to the silicon back-gate (these measurements were carried out in devices without a top-gate, in a four-probe configuration, using a Hall-bar geometry). Specifically, $R_\square$ shows a peak (see Fig. 1c and inset of Fig. 5a) that is broader and less pronounced than the peaks for single-layer and bilayer graphene. R_H displays a non-monotonous behaviour as a function of V_{bg}, with a characteristic sign reversal at the position of the maximum resistance, V_{bg}^{max} (see Fig. 1d). In trilayer graphene the range of V_{bg} over which R_H decreases and changes sign is much wider ($\Delta V_{bg} \approx 8$ V) than in single-layer and bilayer graphene, which are zero-gap semiconductors ($\Delta V_{bg} \approx 1$ V for single-layer and bilayer graphene present on the same flake of the trilayer). Such a large ΔV_{bg}, as well as the broader and shallower peak in resistivity, should be expected if trilayer graphene is a semimetal, due to the finite overlap ($\delta\varepsilon$) of the conduction and valence bands. Indeed, under the assumption that trilayer graphenes are semimetals, we can satisfactorily fit R_H over the whole range of V_{bg} with a $\delta\varepsilon \approx 28$ mV (see Methods for details).

Our experiments on trilayer graphene heavily rely on the application of a tunable, static electric field perpendicular to the layer, which provides a unique tool to investigate the electronic properties of graphene-based materials[10–12,24,25]. To generate such a perpendicular field we use double-gated devices (see Fig. 1b) that also provide independent control of the carrier density in the material (that is, the position of the Fermi level). Figure 2a, b shows $R_\square$ for a double-gated trilayer graphene device measured at $T = 50$ mK as a function of the voltage applied to one of the gates, while the other gate is kept at a constant potential. These measurements on double-gated devices were mainly carried out in a two-terminal configuration, which allowed the fabrication and comparison of a larger number of devices on flakes containing layers of different thickness. Measurements in a four-terminal configuration were also performed on several devices to ensure that the effect of the contact resistance—present in two-terminal measurements—did not influence significantly the results (see Methods and Supplementary Information for details; we have also measured the precise value of contact resistance and found that contact effects can be neglected).

Irrespective of which gate voltage is being swept, we always observe a maximum in the resistance $R_\square^{max}$, which is attained at the charge

[1]Department of Applied Physics and Quantum-Phase Electronics Center, The University of Tokyo, 7-3-1 Hongo, Bunkyo-ku, Tokyo 113-8656, Japan, [2]Kavli Institute of Nanoscience, Delft University of Technology, Lorentzweg 1, 2628 CJ Delft, The Netherlands, [3]Department of Condensed Matter Physics and Group of Applied Physics, University of Geneva, quai Ernest-Ansermet 24, CH-1211 Geneva 4, Switzerland, [4]Quantum Spin Information Project, International Cooperative Research Project, Japan Science and Technology Agency, Atsugi-shi, 243-0198, Japan, [5]Institute for Nano Quantum Information Electronics, The University of Tokyo, 4-6-1 Komaba, Meguro-ku, Tokyo 153-8505, Japan; †These authors contributed equally to this work.
*e-mail: monica@meso.t.u-tokyo.ac.jp; saverio@meso.t.u-tokyo.ac.jp

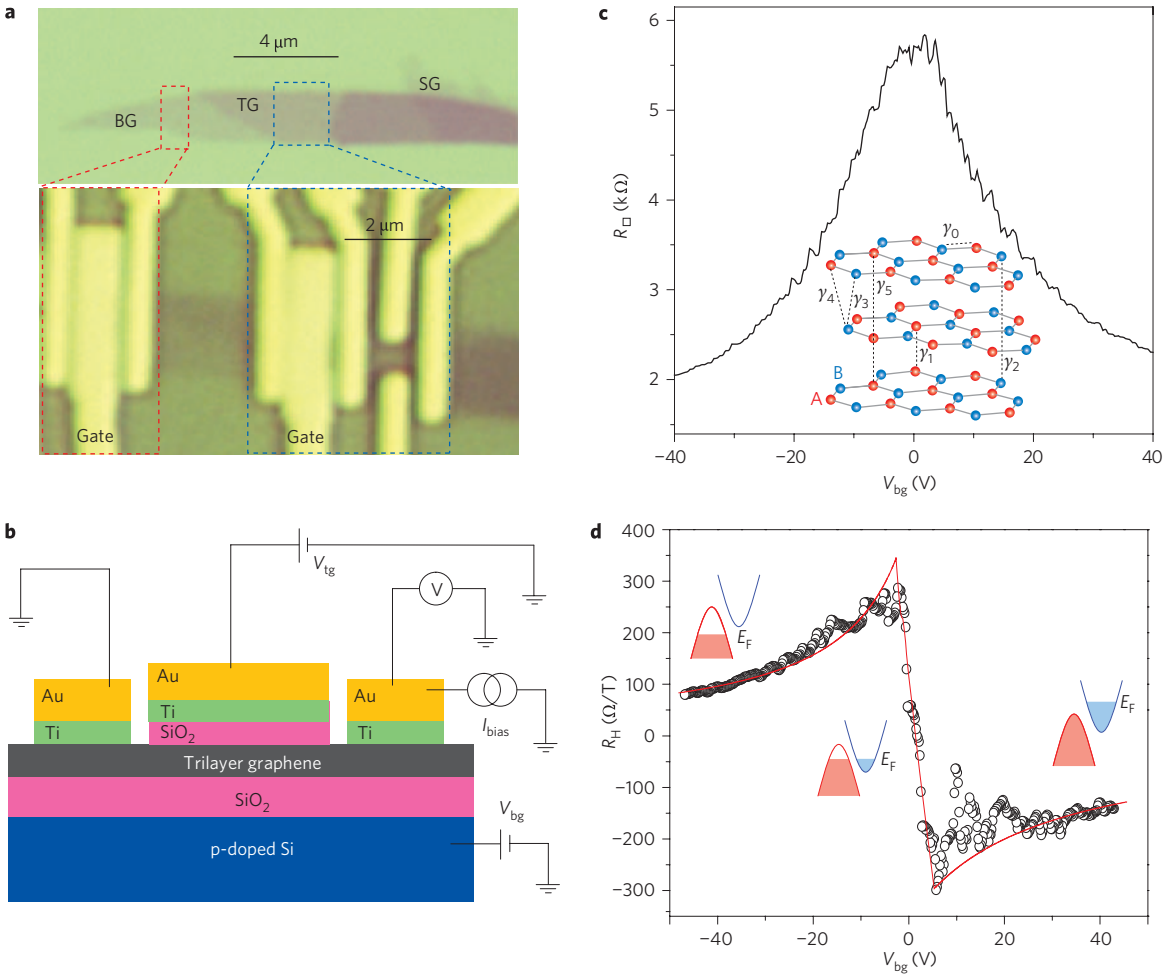

Figure 1 | Characterization of trilayer graphene. a, Optical microscope images of an exfoliated graphite flake (top) containing single-layer graphene (SG), bilayer graphene (BG) and trilayer graphene (TG), and of the devices (bottom) fabricated on the bilayer and trilayer parts of the same flake. **b**, Schematic of a double-gated device. The position of the Fermi level in trilayer graphene and the applied perpendicular electric field are controlled by the voltages applied to the back-gate (V_{bg}) and the top-gate (V_{tg}). We study the resistance of the layers as a function of these gate voltages by applying an a.c. ($f = 13$ Hz) current bias I and measuring the resulting voltage V across the device with a lock-in amplifier. **c**, Square resistance as a function of V_{bg} at 50 mK. The inset shows the crystal structure of a trilayer graphene. The parameters γ_0 to γ_5 label the tight-binding transfers integral between the different pairs of atoms. **d**, Measured Hall coefficient as a function of V_{bg} (open circles) for a fixed perpendicular magnetic field of 9 T at 50 mK. The red curve is a fit (see Methods). The three insets schematically depict the position of the Fermi level (E_F) at different values of V_{bg}.

neutrality point where the electron and hole density in the system are the same. As expected, the position of $R_\square^{max}$ that is observed when sweeping one gate shifts as a function of the voltage applied to the other gate, reflecting the change in charge density induced by the two gates. More importantly, we observe that the maximum resistance value at the charge neutrality point depends on the configuration of the gate voltages, (Fig. 2a, b). In particular, the height of $R_\square^{max}$ decreases as the top- and back-gates are biased with voltages of opposite polarity and of increasing magnitude (that is, $R_\square^{max}$ decreases when the applied perpendicular electric field increases).

The electric field response of $R_\square^{max}$ measured at 50 mK for trilayer graphene is summarized in the colour plot of $R_\square$ in Fig. 2c. The systematic decrease of $R_\square^{max}$ as a function of electric field, which is observed in all the measured devices (see Supplementary Information), is different from the behaviour of other few-layer graphenes studied in the past and appears to be unique to trilayer graphene. Specifically, it has been shown that a perpendicular electric field applied on single-layer graphene does not affect the value of the resistance maximum $R_\square^{max}$ (see also Supplementary Fig. S3a), and that on double-gated bilayer graphene $R_\square^{max}$ increases when increasing the electric field, consistent with the opening of a gap in the density of states[10–12,24,25] (see also Fig. 2d). We therefore conclude that the observed decrease of $R_\square^{max}$ with external electric field is a characteristic fingerprint of trilayer graphene. Note that, for trilayer graphene, the same electric field dependence of $R_\square^{max}$ is preserved over the entire experimentally investigated temperature range (up to 200 K). This is clearly summarized in Fig. 3a, which shows $R_\square^{max}$ measured as a function of V_{tg} (with V_{bg} chosen correspondingly at each point, to maintain the device charge neutral), for different temperatures. The temperature-dependent measurements also show that $R_\square^{max}$ decreases when raising the temperature.

As we will now show, all our experimental observations can be consistently interpreted quantitatively in terms of the semimetallic behaviour of trilayer graphene, if the overlap between the valence and conduction bands progressively increases with increasing applied perpendicular electric field. To understand the details of our analysis, it is important to recall the basic aspects of the electronic structure of trilayer graphene. At low energy, Bernal-stacked trilayer graphene (see inset of Fig. 1c), which is the thermodynamically stable form, has two valence and two conduction bands. Within a tight-binding scheme analogous to the Slonczewski–Weiss–McClure model used to describe graphite[26,27],

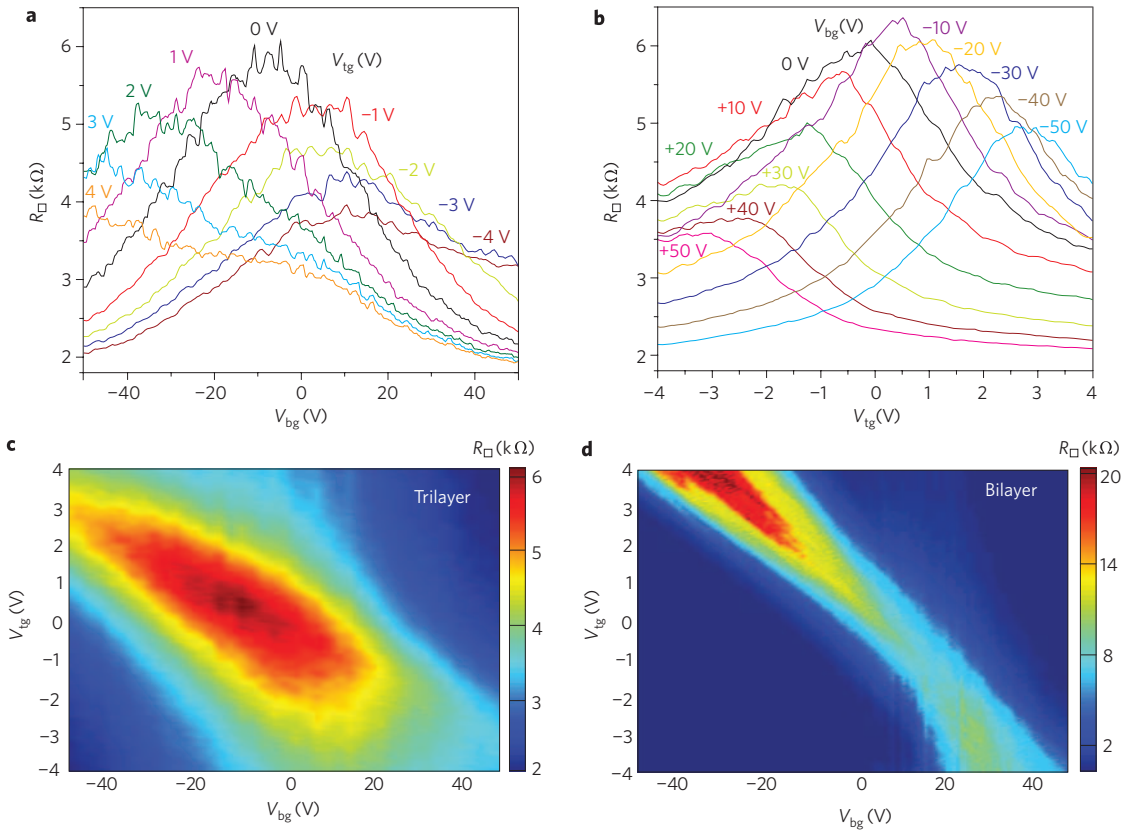

Figure 2 | Transport in the presence of a perpendicular electric field. a, Square resistance of a trilayer device versus back-gate voltage V_{bg} for different values of the top-gate voltage V_{tg} at 50 mK. V_{bg} is an order of magnitude larger than V_{tg} because the bottom-gate insulator is an order of magnitude thicker than the top-gate insulator. The value of $R_\square^{max}$ systematically decreases when the perpendicular electric field applied is increased. **b**, Square resistance of a trilayer device versus V_{tg} for different values of V_{bg} at 50 mK. Again, the value of $R_\square^{max}$ systematically decreases as the electric field is increased. **c**,**d**, Colour plots of the square resistance of trilayer graphene at 50 mK (**c**) and bilayer graphene at 300 mK (**d**) as a function of both V_{bg} and V_{tg}. Whereas the applied electric field enhances the overlap between valence and conduction bands in trilayer graphene (leading to an increase in conductance), it opens up a gap in bilayer graphene (leading to an increase in resistance).

the precise details of these bands depend on the values of all the transfer integrals introduced. However, if in a first approximation these details are disregarded, for both valence and conduction bands, one band disperses linearly and the other quadratically. Because the density of states of linearly dispersing bands goes to zero at zero energy, the bands that are relevant to understand the low-energy transport properties are the ones dispersing quadratically, which give the dominant contribution to the total density of states. In interpreting our data, therefore, we will consider only the low-energy valence and conduction bands with quadratic dispersion relation, and we will assume the presence of a finite band overlap $\delta\varepsilon$ (see also the last section of the Supplementary Information). In addition, as is predicted theoretically by the simplest tight-binding models for trilayer graphene[28], we will take the effective mass in the valence and conduction (quadratically dispersing) bands to be equal ($m_e^\star = m_h^\star = m^\star$).

We first analyse the temperature dependence of $R_\square^{max}$, which allows the direct determination of the band overlap $\delta\varepsilon$ for all values of the applied perpendicular electric field. Within the scenario introduced above (and along the lines of the discussion of Ref. 1), $R_\square^{max}$ is related to the total carrier density (that is, electron plus hole density) in the mixed state through the relation $n = 2/[e(\mu_e + \mu_h)R_\square^{max}]$ (note that $n_e = n_h = n/2$). The decrease in $R_\square^{max}$ with increasing temperature originates from the increase in the number of thermally excited carriers around the Fermi energy, which, for a semimetal, can be written as $n(T) = (16\pi m^*/h^2 c)k_B T \ln[1 + e^{\delta\varepsilon/2k_B T}]$ (with c equal to twice the layer spacing)[29]. By normalizing $n(T)$ to the value at $T = 4.2$ K, $n(T)/n(4.2\,\mathrm{K}) = (T/4.2)\ln(1 + e^{\delta\varepsilon/2k_B T})/\ln(1 + e^{\delta\varepsilon/2k_B 4.2})$, the band overlap $\delta\varepsilon$ can be directly obtained through a one-parameter fit to the experimental data. Figure 3b shows that an excellent quality of the fit is obtained for all values of the applied perpendicular electric field E_{ext} ($E_{ext} = (V_{tg} - V_{bg}^m)/(d_{tg} + d_{bg})$, where V_{bg}^m is the value of V_{bg} for which the resistance is maximum and $d_{bg,tg}$ are the thicknesses of the dielectrics for the back- and top-gates). The values of the band overlap obtained in this way are plotted in Fig. 4a as a function of field: it is apparent that the band overlap changes as a function of the external electric field, and $\delta\varepsilon$ increases with increasing E_{ext} from ~30 to 60 meV, independent of the electric field polarity.

The band overlap and its electric field dependence can also be extracted by looking only at the low-temperature (50 mK) measurements. In fact, at such a low temperature, $\delta\varepsilon = n/D$, with $D = 2m^*/\pi\hbar^2$ the total low-energy two-dimensional density of states. Because $\delta\varepsilon$ and $n = 2/[e(\mu_e + \mu_h)R_\square^{max}]$ are experimentally known, we can use this relation to extract the effective mass of the charge carriers: $m^* = \pi\hbar^2/[e(\mu_e + \mu_h)R_\square^{max}\delta\varepsilon]$. We find that at $E_{ext} = 0$ the estimated effective mass is $m^* = (0.054 \pm 0.005)m_0$, and that m^* remains constant when E_{ext} is increased (see Fig. 4b; m_0 is the free electron mass). This value of the effective mass is consistent with theoretical predictions based on tight-binding calculations, which give $m^* = (2\sqrt{2}/3)\hbar^2\gamma_1/(a^2\gamma_0^2) = 0.052\,m_0$ (ref. 28) ($a = 0.246$ nm, the monolayer lattice constant, $\gamma_0 = 3.16$ eV (ref. 17), $\gamma_1 = 0.44$ eV (ref. 30)). Having determined the effective

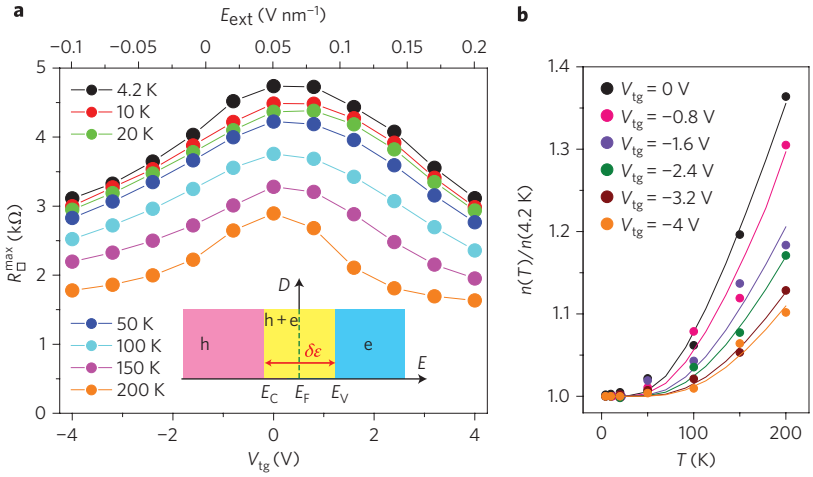

Figure 3 | Temperature-dependent transport through trilayer graphene. a, Maximum square resistance $R_{\square}^{max}$ versus top-gate voltage V_{tg} at different temperatures. For each value of V_{tg}, the back-gate voltage V_{bg} is chosen so that the device is at the charge neutrality point; different values of V_{bg} correspond to different values of the applied electric field E_{ext}. The inset shows a schematic view of the density of states of the quadratic bands that are responsible for the semimetallic behaviour of trilayer graphene. At the charge neutrality point, where the resistance reaches its maximum, the Fermi level E_F lies between the bottom of conduction band E_c and the top of the valence band E_v. **b**, Temperature dependence of the carrier concentration n in the mixed state determined from the value of $R_{\square}^{max}$ measured at different values of V_{tg} (or E_{ext}). The solid curves represent the fitted dependence using the expression $n(T)/n(4.2\ K) = (T/4.2)\ln(1+e^{\delta\varepsilon/2k_BT})/\ln(1+e^{\delta\varepsilon/2k_B4.2})$, from which we extract the band overlap $\delta\varepsilon$. (See Supplementary Fig. S9, for similar plots for $V_{tg} > 0$.)

mass, and with the carrier density and the conductivity known, we can use the Drude formula for conductivity to extract the scattering time τ. As shown in Fig. 4c, we find that τ decreases with increasing applied electric field. These observations confirm that the overall electric field dependence of the resistance with increasing electric field is due to a relative shift of valence and conduction band, leading to an increase in band overlap, and not to changes in effective mass (which are negligible) or in scattering time (which would tend to increase, rather than to decrease, the resistance; see Fig. 4c). This electric field tunable band overlap is a unique property of trilayer graphene, which has never been previously found in other semimetallic systems.

An alternative—but fully equivalent—way to look at our data, which better illustrates the comparison between experiment and theory as a function of perpendicular electric field, is to take the theoretical value for the effective mass $m^* = 0.052m_0$ and plot together the values obtained for $\delta\varepsilon$ in the two different ways (that is, by looking at the temperature dependence of the maximum resistance, or by simply looking at its value at 50 mK). The result of this comparison as a function of E_{ext} is presented in Fig. 4a, which shows a remarkable agreement throughout the entire E_{ext} range. Note that, at $E_{ext} = 0$ we obtain $\delta\varepsilon = 32$ meV from the temperature dependence and $\delta\varepsilon = 34$ meV from the data at 50 mK, close to the value $\delta\varepsilon \approx 28$ meV already obtained earlier by analysing the gate voltage dependence of the Hall resistance (Fig. 1d; the error on the values for $\delta\varepsilon$ obtained with the different methods is between 10 and 20%).

Finding that three different methods used to estimate the band overlap result in values that are in quantitative agreement with each other provides a clear indication of the validity of our analysis, and confirms that the experiments are probing the intrinsic electronic properties of trilayer graphene. This conclusively demonstrates that the low-energy band structure of trilayer graphene can be tuned by a large amount through the application of an external perpendicular electric field, achieving a 100% change in band overlap. A similar electric-field-tunable $\delta\varepsilon$ was experimentally observed in all devices investigated, albeit with a spread (about 30%) in the value of external field needed to induce a same shift of the band overlap in different devices (see Supplementary Information). We attribute these differences in the precise electric field value to screening due to unwanted adsorbed

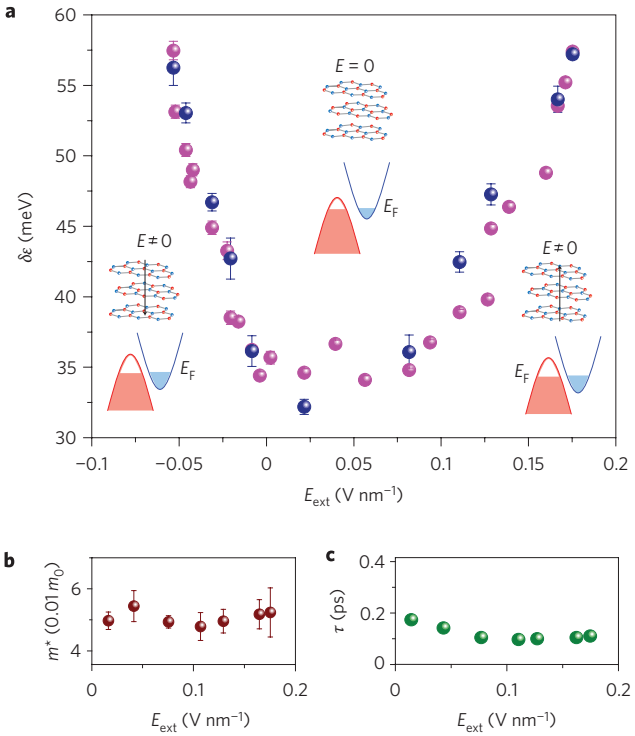

Figure 4 | Electric field dependence of the band overlap in trilayer graphene. a, Band overlap $\delta\varepsilon$ versus applied electric field E_{ext}. The dark blue dots represent the values estimated from the temperature dependence of the charge density in the mixed state (see Fig. 3b). The purple dots are the values estimated from the maximum resistivity measured at 50 mK, using the theoretical value of the effective mass for the quadratic bands ($m^* = 0.052m_0$). The inset shows a schematic view of the band structure, showing that the band overlap increases when E_{ext} is nonzero. **b**, Effective mass (derived from experimental data; see main text) versus E_{ext}. **c**, The scattering time τ extracted from the measured conductivity and effective electron mass using the Drude formula together with the experimentally determined m^*.

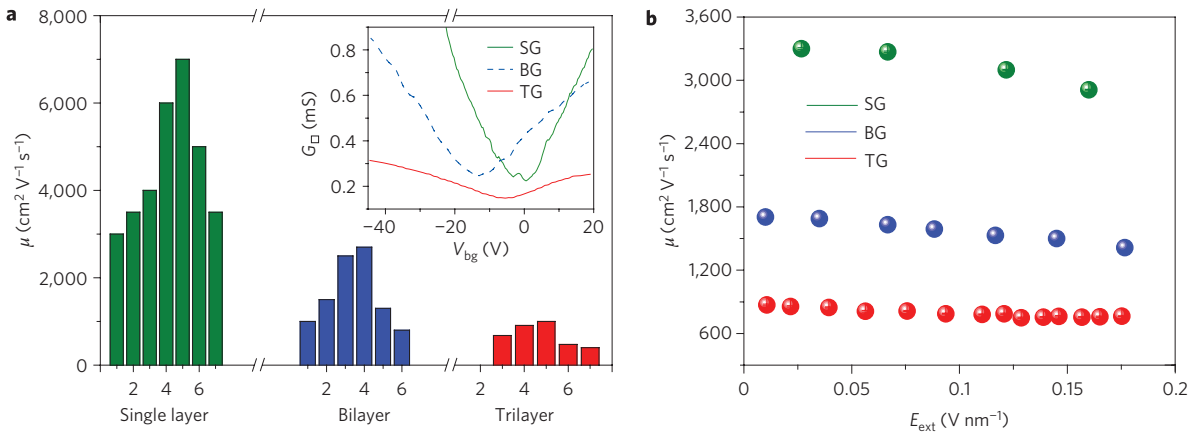

Figure 5 | Comparison of carrier mobility in few-layer graphene. a, Statistics of mobility values in single-layer, bilayer and trilayer graphene, estimated from the dependence of the conductivity σ on the back-gate voltage V_{bg}. Trilayers systematically exhibit lower mobility, and the ratio between the average mobility in bilayer and trilayer graphene is approximately consistent with the ratio of the effective mass of the charge carriers in the two materials. The inset shows the conductivity versus V_{bg}: the finite band overlap in trilayer graphene results in a lower minimum conductivity compared with bilayer and trilayer graphene. **b**, Mobility versus applied electric field E_{ext}, also showing a different behaviour for different layer thickness. In particular, the decrease in the mobility with increasing E_{ext} becomes less pronounced as the number of layers increases.

layers present at the SiO_2/graphene interfaces (for example, water or hydrocarbons).

Having established that the band structure of trilayer graphene differs significantly from that of single and double layers due to the presence of an overlap between valence and conduction band, it is also interesting to look at the evolution of the carrier mobility in these materials. A comparison of the mobility values measured in graphene layers of different thickness is shown in Fig. 5a. It is apparent that trilayer graphene systematically exhibits lower mobility (typically $\sim$800 cm^2 V^{-1} s^{-1} at 4.2 K) than single-layer and bilayer graphene. The trend originates in large part from the difference in the effective mass in the different materials, which increases with increasing layer thickness ($m^*_{SG} = 0$, $m^*_{BG} = 0.037m_0$, and $m^*_{TG} = 0.052\,m_0$) (ref. 28). The observation of this trend, together with the different response to a perpendicular electric field and the differences in the low-energy band structure discussed above, show that every individual graphene multilayer sequence is a new material in its own right. Regarding the low-energy electronic properties it is unclear whether a 'smooth' evolution from graphene to graphite can be expected as the number of layers is increased. Our results suggest that for systems consisting of only a few layers, this evolution with thickness may be dominated by unique aspects specific to each layer thickness. In trilayer graphene, one such unique property is the possibility to tune the band overlap electrostatically, over a large range. Note added in proof: After this manuscript was accepted, the theoretical results concerning the band structure modulation of trilayer graphene by external electric field, in agreement with our data, have been published[31].

Methods

Fabrication details. Few-layer graphene was obtained by means of mechanical exfoliation of bulk graphite and transferred onto the surface of a highly doped silicon substrate covered by a 285-nm thick layer of thermally grown SiO_2. The highly doped silicon substrate was used as the back-gate, and the top-gate was defined by means of electron-beam lithography and lift-off of electron-beam-evaporated SiO_2 and of a titanium/gold bilayer (the thicknesses of the SiO_2, titanium, and gold were 15, 10 and 100 nm, respectively). To maximize the contribution of the gated regions to the total resistance measured in a two-probe configuration, two ohmic contacts (made of titanium and gold, of thicknesses 10 and 100 nm) were fabricated (again by electron-beam evaporation and lift-off) within 50 nm from the edge of the 1-μm-wide top-gate. Less than 5% of the overall resistivity was therefore due to the non-gated region.

Gate voltage dependence of the Hall coefficient. As mentioned in the text, the dependence of the Hall coefficient R_H on the back-gate voltage V_{bg} indicates the semimetallic nature of trilayer graphene, and can be used to extract an estimate of the band overlap. To fit the data in Fig. 1d we used the fact that, when the Fermi level is located deep in the conduction or valence bands (so that only electrons or holes are present, $V_{bg} \gg 6$ V and $V_{bg} \ll -2$ V), $R_H = 1/en_{e,h}$, with $n_{e,h}$ being the electron/hole carrier concentration. In the mixed charge carrier regime, when both electrons and holes are present simultaneously, R_H is a function of both carrier charge densities and mobility $\mu_{e,h}$: $R_H = (n_h\mu_h^2 - n_e\mu_e^2)/e(n_e\mu_e + n_h\mu_h)^2$. Using these formulae, we can fit $R_H(V_{bg})$ over the entire V_{bg} range. In doing this, the total charge density of carriers is calculated from the known capacitance to the gate ($n = \varepsilon_0\varepsilon V_{bg}/d_{bg}e$) and $\mu_{e,h}$ are taken to be constant (that is, V_{bg}-independent) and equal to the values obtained from the gate voltage dependence of the conductivity at high V_{bg} values (that is, far outside the mixed charge carrier regime). The only fitting parameter is the band overlap $\delta\varepsilon$, which is related to the V_{bg} width of the mixed state through the density of states of the quadratically dispersing electron and hole bands. Note that the Hall effect measurements were carried out on samples with back-gate only (that is, no top-gate) and so only the value of $\delta\varepsilon$ at zero perpendicular electric field can be obtained in this way.

Contact resistance. Longitudinal and transverse magnetoresistance were measured in a Hall-bar geometry, in devices containing only a back-gate and no top-gate. In this case measurements could be performed in a four-terminal configuration, where the contact resistance between metal electrodes and trilayer graphene plays no role. On the contrary, in double-gated devices, the introduction of voltage probes under the top-gate proved to be technically very difficult (due to the failure of the SiO_2 layer insulating the trilayer graphene from the top-gate). Therefore, although we also investigated devices where measurements were carried out in a four-terminal configuration, we opted to investigate the dependence of $R_\square$ on the perpendicular electric field mostly by means of two-terminal measurements. In such a two-terminal geometry the influence of the contact resistance needs to be considered. We have successfully measured the contact resistance in different ways (by comparing the results of two terminal measurements performed on devices fabricated on the same flake, by comparing two- and four-terminal measurements and by scaling experiments as a function of the contact separation; see Supplementary Information). We found that the contact resistance is always weakly gate-voltage-dependent and in all cases less than 20% than the total resistance measured at high gate voltage. Close to the charge neutrality point, where $R_\square$ is larger, the relative effect of the contact resistance is even smaller (typically less than 10%). We conclude that the presence of a contact resistance does not significantly affect our results and their interpretation. Note, finally, that in the samples where we performed four-terminal measurements, the results for $\delta\varepsilon$ were fully consistent with those obtained from two-terminal measurements.

Received 2 February 2009; accepted 20 March 2009; published online 26 April 2009

References

1. Novoselov, K. S. *et al.* Electric field effect in atomically thin carbon films. *Science* **306,** 666–669 (2004).
2. Novoselov, K. S. *et al.* Two-dimensional gas of massless Dirac fermions in graphene. *Nature* **438,** 197–200 (2005).

3. Zhang, Y. B. *et al.* Experimental observation of the quantum Hall effect and Berry's phase in graphene. *Nature* **438,** 201–204 (2005).
4. Geim, A. K. & Novoselov, K. S. The rise of graphene. *Nature Mater.* **6,** 183–191 (2007).
5. Tombros, N. *et al.* Electronic spin transport and spin precession in single graphene layers at room temperature. *Nature* **448,** 571–574 (2007).
6. Williams, J. R., DiCarlo, L. & Marcus, C. M. Quantum Hall effect in a gate-controlled p–n junction of graphene. *Science* **317,** 638–641 (2007).
7. Ponomarenko, L. A. *et al.* Chaotic Dirac billiard in graphene quantum dots. *Science* **320,** 356–358 (2008).
8. Meric, I. *et al.* Current saturation in zero-bandgap, top-gated graphene field-effect transistors. *Nature Nanotech.* **3,** 654–659 (2008).
9. Novoselov, K. S. *et al.* Unconventional quantum Hall effect and Berry's phase of 2π in bilayer graphene. *Nature Phys.* **2,** 177–180 (2006).
10. Oostinga, J. B. *et al.* Gate-induced insulating state in bilayer graphene devices. *Nature Mater.* **7,** 151–157 (2008).
11. Castro, E. V. *et al.* Biased bilayer graphene: Semiconductor with a gap tunable by the electric field effect. *Phys. Rev. Lett.* **99,** 216802 (2007).
12. Ohta, T., Bostwick, A., Seyller, T., Horn, K. & Rotenberg, E. Controlling the electronic structure of bilayer graphene. *Science* **313,** 951–954 (2006).
13. Guettinger, J. *et al.* Coulomb oscillations in three-layer graphene nanostructures. *New J. Phys.* **10,** 125029 (2008).
14. Schedin, F. *et al.* Detection of individual gas molecules adsorbed on graphene. *Nature Mater.* **6,** 652–655 (2007).
15. Bolotin, K. I. *et al.* Ultrahigh electron mobility in suspended graphene. *Solid State Commun.* **146,** 351–355 (2008).
16. Sugihara, K., Kawamura, K. & Tsuzuku, T. Temperature dependence of the average mobility in graphite. *J. Phys. Soc. Jpn* **47,** 1210–1215 (1979).
17. Dreselhaus, M. S. & Dresselhaus, G. Intercalation compounds of graphite. *Adv. Phys.* **30,** 139–326 (1981).
18. Chen, J. H., Jang, C., Xiao, S., Ishigami, M. & Fuhrer, M. S. Intrinsic and extrinsic performance limits of graphene devices on SiO_2. *Nature Nanotech.* **3,** 206–209 (2008).
19. Guinea, F., Castro Neto, A. H. & Peres, N. M. R. Electronic states and Landau levels in graphene stacks. *Phys. Rev. B* **73,** 245426 (2006).
20. Latil, S. & Henrard, L. Charge carriers in few-layer graphene films. *Phys. Rev. Lett.* **97,** 036803 (2006).
21. Partoens, B. & Peeters, F. M. From graphene to graphite: Electronic structure around the K point. *Phys. Rev. B* **74,** 075404 (2006).
22. Lu, C. L. *et al.* Influence of an electric field on the optical properties of few-layer graphene with AB stacking. *Phys. Rev. B* **73,** 144427 (2006).
23. Aoki, M. & Amawashi, H. Dependence of band structures on stacking and field in layered graphene. *Solid State Commun.* **142,** 123–127 (2007).
24. McCann, E. Asymmetry gap in the electronic band structure of bilayer graphene. *Phys. Rev. B* **74,** 161403 (2006).
25. Min, H., Sahu, B. R., Banerjee, S. K. & MacDonald, A. H. Ab initio theory of gate induced gaps in graphene bilayers. *Phys. Rev. B* **75,** 155115 (2007).
26. McClure, J. W. Band structure of graphite and de Haas–van Alphen effect. *Phys. Rev.* **108,** 612–618 (1957).
27. Slonczewski, J. C. & Weiss, P. R. Band structure of graphite. *Phys. Rev.* **109,** 272–279 (1958).
28. Koshino, M. & Ando, T. Orbital diamagnetism in multilayer graphenes: Systematic study with the effective mass approximation. *Phys. Rev. B* **76,** 085425 (2007).
29. Klein, C. A. STB model and transport properties of pyrolytic graphite. *J. Appl. Phys.* **35,** 2947–2957 (1964).
30. Ohta, T. *et al.* Interlayer interaction and electronic screening in multilayer graphene investigated with angle-resolved photoemission spectroscopy. *Phys. Rev. Lett.* **98,** 206802 (2007).
31. Koshino, M. & McCann, E. Gate-induced interlayer asymmetry in ABA-stacked trilayer graphene. *Phys. Rev. B* **79,** 125443 (2009).

Acknowledgements

We gratefully acknowledge E. McCann, M. Koshino and T. Ando for illuminating discussions and for sharing their preliminary theoretical results concerning the band structure modulation of trilayer graphene. We acknowledge financial support from the Japan Society for the Promotion of Science, grant P07372 (M.F.C.), Foundation for Fundamental Research on Matter (S.R.), Grant-in-Aid for Young Scientists A (no. 20684011) and Exploratory Research for Advanced Technology—Japan Science and Technology Agency (080300000477) (M.Y.). A.F.M. gratefully acknowledges financial support from The Netherlands Organization for Scientific Research (NWO) VICI and Foundation for Fundamental Research on Matter in the Netherlands and from the Swiss National Science Foundation (grant 200021-121569). S.T. acknowledges financial support from the Grant-in-Aid for Scientific Research S (no. 19104007), B (no. 18340081) and Japan Science and Technology Agency—Core Research for Evolutional Science and Technology.

Author contributions

M.F.C. and S.R. contributed equally to this work: they conceived and performed the experiments, analysed the data, and wrote the manuscript. A.F.M. contributed to the interpretation of the data and to writing the manuscript. J.B.O. contributed to the device fabrication. M.Y. contributed to the realization of the measurement setups. S.T. directed the research. All authors discussed the results extensively and commented on the manuscript.

Additional information

Supplementary information accompanies this paper at www.nature.com/naturenanotechnology. Reprints and permission information is available online at http://npg.nature.com/reprintsandpermissions/. Correspondence and requests for materials should be addressed to M.F.C. and S.R.

nature nanotechnology

LETTERS

PUBLISHED ONLINE: 12 APRIL 2009 | DOI: 10.1038/NNANO.2009.77

Atomic force microscopy detects differences in the surface brush of normal and cancerous cells

S. Iyer[1†], R. M. Gaikwad[1], V. Subba-Rao[1†], C. D. Woodworth[2,3] and Igor Sokolov[1,3*]

The atomic force microscope is broadly used to study the morphology of cells[1–5], but it can also probe the mechanics of cells. It is now known that cancerous cells may have different mechanical properties to those of normal cells[6–8], but the reasons for these differences are poorly understood[9]. Here, we report quantitatively the differences between normal and cancerous human cervical epithelial cells by considering the brush layer on the cell surface. These brush layers, which consist mainly of microvilli, microridges and cilia, are important for interactions with the environment. Deformation force curves obtained from cells *in vitro* were processed according to the 'brush on soft cell model'[10]. We found that normal cells have brushes of one length, whereas cancerous cells have mostly two brush lengths of significantly different densities. The observed differences suggest that brush layers should be taken into account when characterizing the cell surface by mechanical means.

Cancerous cells differ from normal cells in terms of cell growth, morphology, cell–cell interaction, organization of the cytoskeleton and interactions with the extracellular matrix[11–13]. The atomic force microscope (AFM) can be used to detect most of these changes[9,14], but one of the main challenges in understanding these differences is the lack of statistically sound quantitative data. To quantify the mechanical properties of cells, AFM probes with a well-defined geometry are needed. They should not be too sharp in order to avoid nonlinear cell responses[15,16]. For example, micrometre-sized silica spheres have been used successfully to study the mechanics of cells[4,5] (see Supplementary Information for the advantages of these probes). In addition, it is also important to consider the presence of brush-type structures on the cell surface, such as molecules that are grafted on the cell membrane and membrane corrugations like microvilli and microridges. Here, we show quantitatively the differences between the brush layers on the surfaces of normal and cancerous human cervical epithelial cells.

Although differences between the surfaces of cancerous and normal cells are expected, there are still many unknowns. For example, a difference in the cilia on the surfaces of cancerous and normal cells has been found recently[17]. Cilia that protrude from the apical/lumenal surface of polarized cells act as sensors of environmental cues. Similarly, microvilli are important to the ability of cells to interact with the environment. Molecular entropic brushes are known to surround neurofilaments to maintain interfilament spacing[2,18]. Furthermore, molecular brushes on living cells, composed of a glycocalyx layer and a pericellular molecular coating[19,20], are known to be responsible for cell–cell interaction, cell migration, differentiation and proliferation[21,22]. The size of the pericellular coating has been shown[20,23] to correlate with the degree of invasiveness of cancer (although it is still not clear whether the brush size or molecular composition, or maybe both, has the major role). Therefore, our reported difference in the brush layers may have a large biological significance.

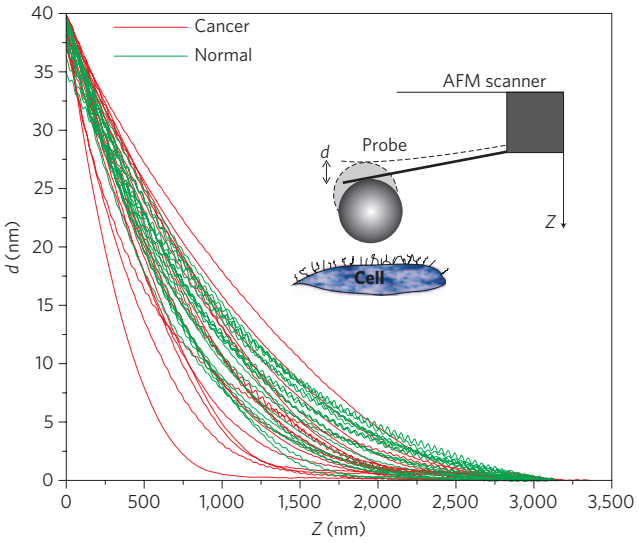

Figure 1 | Raw force curves of normal and cancerous cells. The plot shows the deflection of the cantilever *d* versus the vertical position of the scanner *Z*. Curves were collected from 35 to 40 normal and cancerous cells. Each curve represents an average of 30 to 50 individual curves measured over relatively flat regions of each cell (with an incline of less than 10–15°, which could be the top and/or side of the cell). Data from two cells were discarded because they deviated too far from the others. This is not unusual because some cells may be dead, damaged or in mitosis, which can change the mechanical characteristics of the cell[9,30].

Curves of the displacement of the AFM cantilever versus vertical position of the scanner (raw force data) are shown in Fig. 1. As expected[14], cancerous cells show higher variability of force behaviour. However, no clear difference between the curves collected on normal and cancerous cells can be seen.

As we observed with confocal and electron microscopy (see below), both cancerous and normal cells do show the clear presence of a brush. Thus, we should use a brush-on-soft-surface model as described in ref. 10 to process the collected force curves. Having processed the data shown in Fig. 1 (see Supplementary Information for detail), both the Young's modulus of the cell body (Fig. 2a, b) and the long-range repulsive force associated with the brush (Fig. 2c) are obtained. Interestingly, the difference in rigidity between normal and cancerous cells is not statistically significant. In contrast

[1]Department of Physics, Clarkson University, Potsdam, New York 13699, USA, [2]Department of Biology, Clarkson University, Potsdam, NewYork 13699, USA, [3]Nanoengineering and Biotechnology Laboratories Center (NABLAB), Clarkson University, New York 13699, USA; [†]Present address: School of Biomedical, Biomolecular and Chemical Sciences, The University of Western Australia, Australia (S.I.); Department of Physics, Wayne State University, Detroit, Michigan 48202, USA (V.S.-R.). *e-mail: isokolov@clarkson.edu

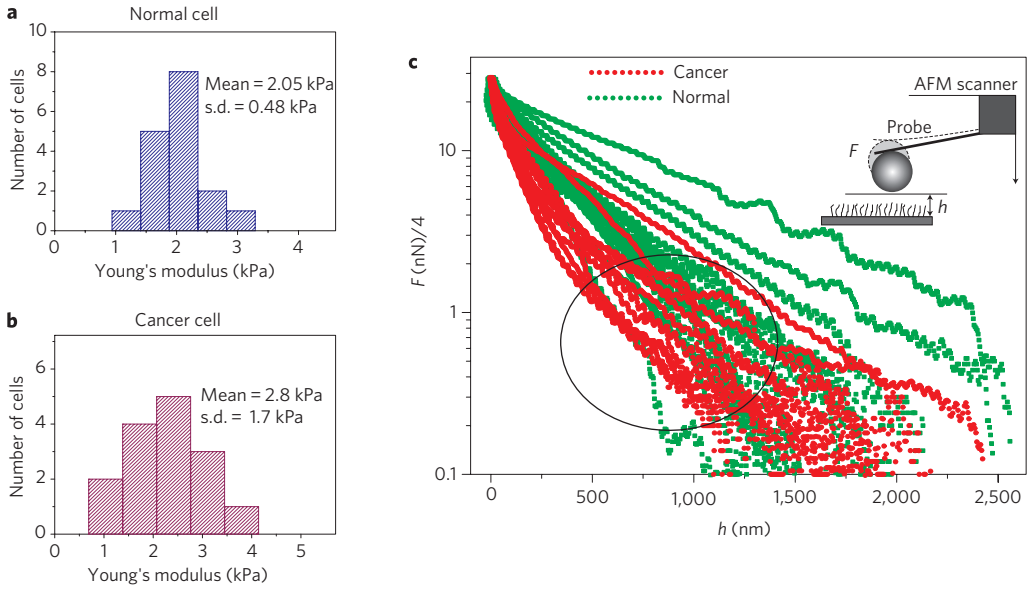

Figure 2 | Processed raw force data from Fig. 1. a,**b**, Derived distributions of the Young's moduli of normal (**a**) and cancerous (**b**) cell bodies. **c**, Forces between the AFM probe and cell brush (see Supplementary Materials for details). Force is shown in a logarithmic scale and is plotted against the distance between the probe and cell body *h*. The slower force decay at large distances in cancerous cells is highlighted by the circle. Force curves for cancerous and normal cells are clearly different. Only one force curve for a normal cell is in the region of the cancerous cells and approximately two cancerous force curves overlap with normal cells.

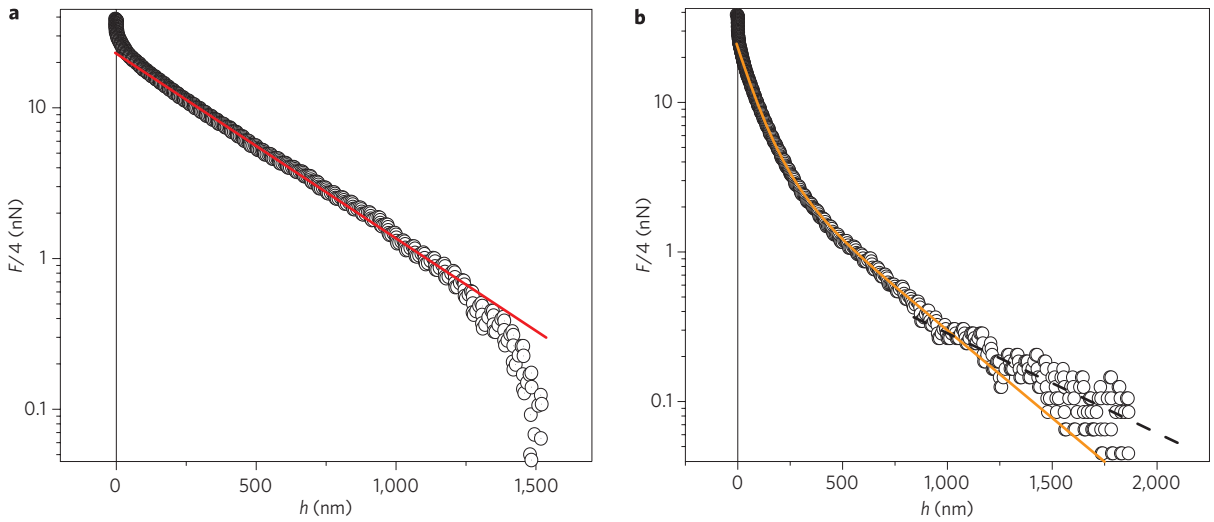

Figure 3 | Representative force curves. a,**b**, Curves due to brush on normal (**a**) and cancerous (**b**) cells. Solid lines represent the model, equation (1) the curves for normal cells, and equation (2) those for cancerous cells. The double-brush behaviour of cancerous cells may be seen. An additional dashed line shown for larger *h* in **b** demonstrates the presence of a weak third brush on cancerous cells.

with the raw force curves in Fig. 1, the forces associated with the brush show a clear difference between cancerous and normal cells. It is quite intriguing to note that the variability of the force curves corresponding to the brush layer is rather small and about the same for both cancerous and normal cells. The cancer variability seen in the raw force curves seems to be entirely accumulated in the values of the Young's moduli of the cell body.

A rather explicit exponential behaviour of the force dependence of the brush can easily be recognized[10,24] (seen as a straight line in the logarithmic scale used in Fig. 2c). Another intriguing feature can also be seen in Fig. 2c. Almost all cancerous force dependences present straight lines having two slopes (highlighted by a circle in Fig. 2c).

For the case of the one-slope force dependence of normal cells, the force between a spherical AFM probe of radius R and the brush can be described by the equation[25]

$$F_{\text{steric}} \approx 50 k_{\text{B}} T R N^{3/2} \exp(-2\pi h/L) L \qquad (1)$$

where L is the equilibrium thickness of the brush layer, N the effective surface density of the brush constituents (grafting density) and T the temperature of the medium. Equation (1) is a good description of a brush for $0.1 < h/L < 0.8$.

To describe the force dependences of cancerous cells, in particular the feature circled in Fig. 2c, we assume that the probe–cell force

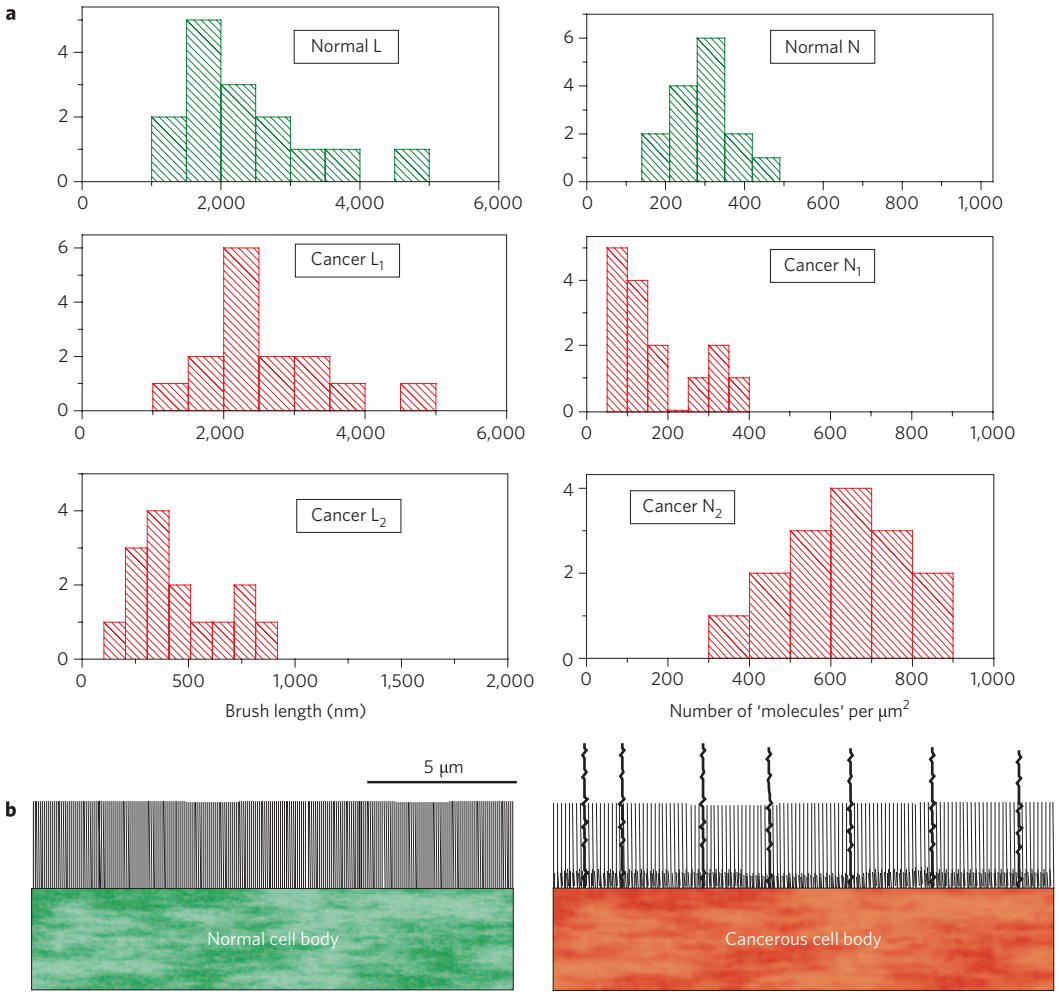

Figure 4 | Brush parameters for cells derived from the force curves of Fig. 2. a, Distribution histograms of brush lengths and grafting density (number of 'molecules' per μm^2). Normal cells have a single-length brush of ~2.4 μm with a grafting density of ~300 'molecules' per μm^2, whereas cancerous cells have a brush with two characteristic lengths of 0.45 and 2.6 μm with grafting densities of ~640 and 180 'molecules' per μm^2, respectively. **b**, Schematic of cells with brushes drawn to scale using the derived brush parameters shown in **a** for normal (left) and cancerous (right) cells. A rare long third brush is also shown for cancerous cells.

arises from two brushes having different lengths described as

$$F_{\text{steric}} \approx 50 k_B T R \times \left[N_1^{3/2} \exp\left(-\frac{2\pi}{L_1} h\right) L_1 + N_2^{3/2} \exp\left(-\frac{2\pi}{L_2} h\right) L_2 \right] \quad (2)$$

Here, the indexes 1 and 2 of N and L correspond to the first and second brushes, respectively. Equation (2) is definitely an approximation. It is out of applicability if the distance h is between the lengths L_1 and L_2, or greater than the larger L. However, the exponential functions vanish quickly, leaving rather small corrections, and a similar approximation has been used previously[26]. Also, the forces we are fitting are the values averaged over the surface of each cell. Therefore, the grafting densities N_1 and N_2 should be treated as a sort of average density.

Figure 3 shows representative examples of fitting normal and cancerous force curves using equations (1) and (2), respectively. One can see a rather good fit. For normal cells (Fig. 3a), the force drops to zero more rapidly than predicted by equation (1) for $h > L$, which is expected for a brush. In contrast, the cancerous cell forces lie above the fitting line for large h. This indicates that cancerous cells have a weak third brush (which can be seen in scanning electron microscopy (SEM) images; see Supplementary Fig. S7). However, the results are too close to the limit of AFM sensitivity to derive quantitative conclusions.

The results of processing the force data for both normal and cancerous cells using equations (1) and (2) are compiled in Supplementary Tables S1 and S2, and are presented as histograms in Fig. 4a. One can see a clear difference between normal and cancerous cell brushes. Normal cells have a single-length brush, but cancerous cells have a double-length brush. The longer of the two lengths is about the size of the normal cell brush (there is no statistically significant difference), but the shorter length is approximately five times smaller (the difference is statistically significant). The grafting density of the long brush is almost one-half that of normal cells, but the short brush is twice as dense as the brush of normal cells. All graphing densities are statistically different. For illustration, Fig. 4b shows a graphical sketch of the brushes with the derived parameters.

To understand the nature of the detected brushes, optical (fluorescent confocal) and electron (SEM and transmission electron microscopy (TEM)) were used (Fig. 5). The sizes of the observed surface corrugations, microvilli and microridges are comparable with the large brush lengths derived from the AFM data. SEM images (Fig. 5a), show higher variability of brush sizes and a longer brush for cancerous cells when compared to normal cells. The longer brush of normal cells appears quite dense on the SEM images, and can be seen as a brush of appropriate size only in confocal and

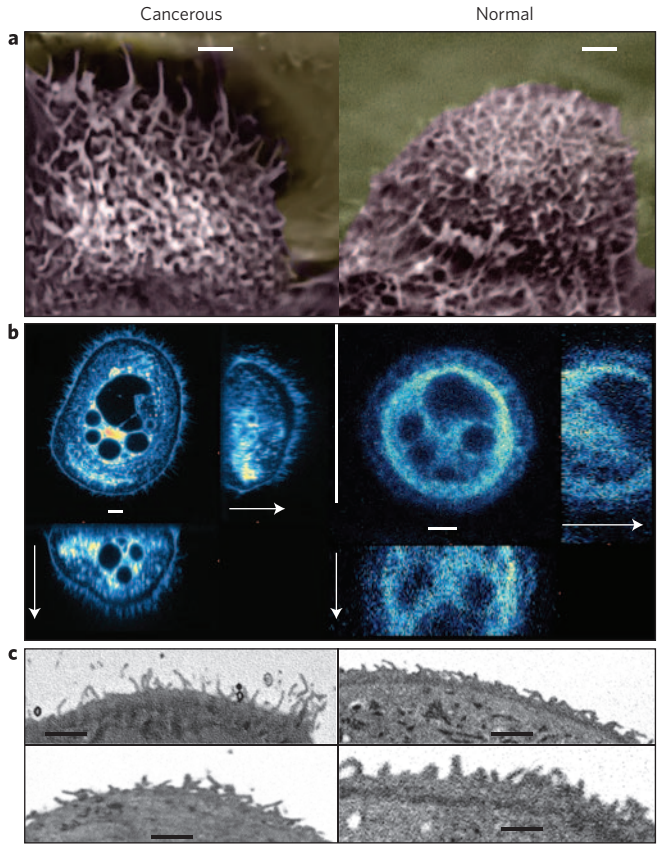

Figure 5 | Visualization of the brushes. a, Side view SEM images of cancerous and normal cells. Colours are artificial and have been used to highlight the cells. Scale bars, 5 μm. **b**, Confocal images of the cells showing the brush associated with membrane corrugations. To distinguish the cell surface brush and filopodia developed on the cell culture dish surface, we also show three-dimensional cross-sections of the cells. The arrows indicate the vertical direction pointing out of the petri dish. Scale bars, 5 μm. **c**, TEM-type images of thin cross-sections of the cell edges. Scale bars, 2 μm.

TEM-type images (Fig. 5b,c). The smaller dense brush derived from the AFM data is seen on the TEM-type images (Fig. 5c). It consists of shorter microvilli and microridges (see also Supplementary Figs S5 and S6).

Comparing Fig. 5 with the graphical sketch of Fig. 4b, one should remember that Fig. 4 shows average brush parameters. Therefore, the graphics are smoother than the actual cell. Second, the graphing density of the 'molecules', being an effective parameter, is not necessarily directly related to the number of membrane protrusions per unit area. To find such a relation, a new model will be developed. This also illustrates the difference in the type of data collected by the AFM microscopy when compared with other microscopy.

Our study shows a quantitative difference between cancerous and normal human cervical epithelial cells found *in vitro* with an AFM method. The standard AFM procedure of processing the collected force data (treating cells as a homogeneous medium) did not show a noticeable difference between the two kinds of cells. However, when processing with a more realistic brush-on-soft-surface model, one can see an unambiguous difference. Although some difference between cancerous and normal cells can be seen using other microscopy techniques (see Supplementary Information for representative sets of SEM- and TEM-type images), it is rather difficult to describe this difference unambiguously and quantitatively. To obtain the same amount of data about the brush as achieved here with the AFM, it would be necessary to carry out TEM tomography of each cell and calculate the brush length. Even that would not be directly comparable to the AFM data because AFM measures mechanical response, not just geometry. Together with the fact that AFM works with viable cells, which decreases the amount of work needed for sample preparation and eliminates artifacts, one can conclude that AFM is a unique technique for the study of cell surfaces. Thus, the observed difference described here may suggest a new approach to the consideration of cancerous cells, and their characterization by means of forces and mechanical parameters. This may lead to a new way of looking at cancer, and its possible detection.

Methods

Cell cultures. We used primary cultures of human cervical epithelial cells prepared from tissues collected from the transformation zone of the cervix of three cancer patients and three healthy individuals. Cell isolation was performed with a two-stage enzymatic digestion process using dispase to remove the epithelium and then trypsin to disperse the individual epithelial cells[27]. Normal and cancerous cell cultures were maintained in keratinocyte serum free medium (KSFM, Invitrogen) under the same experimental conditions. KSFM is a well-defined and widely used medium for growing epithelial cells. The epithelial cells adhered tightly to the bottom of the plastic dish, and the 60-mm cell culture dishes were mounted on the chuck of the AFM with double sticky tape. Cells were grown to ~10% of confluency before using them for scanning (to avoid induction of squamous differentiation of normal cells). All scanning and measurements related to rigidity were performed on proliferating viable cells maintained to room temperature in Hank's balanced salt solution (HBSS) within 2–3 h after removal of growth medium.

Atomic force microscopy. A Nanoscope Dimension 3100 (Digital Instruments/Veeco) AFM was used in the present study. A standard cantilever holder for operation in liquids was used. To collect sufficient statistics, the force–volume mode of operation was used. For details, see the Supplementary Methods.

Dye staining of glycoconjugates of the pericellular brushes. We used the cationic dye Alcian blue (Sigma-Aldrich) to study glycoconjugates of the pericellular brushes of normal and cancerous cells. Using the critical electrolyte concentration method[28], it is also possible to distinguish weakly and strongly charged proteoglycan groups in the cell glycocalix[29]. For details, see the Supplementary Methods.

Confocal microscopy. A confocal microscope (Nikon C1, 10 mW, 488 and 514 nm argon laser, ×100 1.4 NA CFI VC oil-immersed objective) was used. The cells were attached to a LabTek slide (cell suspension in growth medium was placed to the slide for a couple of days). To visualize the cell and cytoplasmic membrane corrugations, 20 μl of 5% ethanol aqueous solution of Nile Red fluorescent dye was added to 1 ml of buffer. Within 15 min after placing the cells in this buffer, viable cells were imaged directly in that buffer.

Electron microscopy. Cells were fixed with Karnovsky's fixative at 4 °C for 2 days, post-stained with 1% osmium tetroxide, further stained with 0.67% aqueous ruthenium tetroxide. SEM imaging was done on freeze-dried samples. For TEM-type of imaging, cells were further dehydrated with absolute ethanol and embedded in Spurr epoxy (firm formulation). Thin sections (20–50 nm) were viewed using electron back-scattering SEM mode. FEI Phenom SEM was used in this study.

Data analysis. The data were fitted to the analytical expression using the Levenberg–Marquardt and Simplex algorithms. The error of the fit was one standard deviation. When calculating error bars for average values, individual standard deviations were discarded as small, and r.m.s. value of mean values was calculated. So, the error bars for average values should be called 'variability bars'. Statistically significant difference was defined using t-test statistics at the $P < 0.05$ level.

Received 15 January 2009; accepted 10 March 2009; published online 12 April 2009

References

1. Habelitz, S. *et al.* Peritubular dentin lacks piezoelectricity. *J. Dental Res.* **86,** 908–911 (2007).
2. Kumar, S. & Hoh, J. H. Modulation of repulsive forces between neurofilaments by sidearm phosphorylation. *Biochem. Biophys. Res. Commun.* **324,** 489–496 (2004).
3. Sokolov, I., Subba-Rao, V. & Luck, L. A. Change in rigidity in the activated form of the glucose/galactose receptor from *E. coli*: A phenomenon that will be key to the development of biosensors. *Biophys. J.* **90,** 1055–1063 (2006).
4. Sokolov, I., Iyer, S. & Woodworth, C. D. Recover of elasticity of aged human epithelial cells *in-vitro*. *Nanomedicine: NBM* **2,** 31–36 (2006).
5. Berdyyeva, T. K., Woodworth, C. D. & Sokolov, I. Human epithelial cells increase their rigidity with ageing *in vitro*: Direct measurements. *Phys. Med. Biol.* **50,** 81–92 (2005).

6. Cross, S. E., Jin, Y.-S., Rao, J. & Gimzewski, J. K. Nanomechanical analysis of cells from cancer patients. *Nature Nanotech.* **2,** 780–783 (2007).
7. Goldmann, W. H. *et al.* Differences in elasticity of vinculin-deficient F9 cells measured by magnetometry and atomic force microscopy. *Exp. Cell Res.* **239,** 235–242 (1998).
8. Lekka, M. *et al.* Elasticity of normal and cancerous human bladder cells studied by scanning force microscopy. *Eur. Biophys. J. Biophys.* **28,** 312–316 (1999).
9. Sokolov, I. in *Cancer Nanotechnology—Nanomaterials for Cancer Diagnosis and Therapy* (eds Nalwa, H. S. and Webster, T.) 43–59 (APS, 2007).
10. Sokolov, I., Iyer, S., Subba-Rao, V., Gaikwad, R. M. & Woodworth, C. D. Detection of surface brush on biological cells *in vitro* with atomic force microscopy. *Appl. Phys. Lett.* **91,** 023902 (2007).
11. Han, J. D. & Rubin, C. S. Regulation of cytoskeleton organization and paxillin dephosphorylation by cAMP. Studies on murine Y1 adrenal cells. *J. Biol. Chem.* **271,** 29211–29215 (1996).
12. Yang, I. H., Co, C. C. & Ho, C. C. Alteration of human neuroblastoma cell morphology and neurite extension with micropatterns. *Biomaterials* **26,** 6599–6609 (2005).
13. Berdyyeva, T., Woodworth, C. D. & Sokolov, I. Visualization of cytoskeletal elements by the atomic force microscope. *Ultramicroscopy* **102,** 189–198 (2005).
14. Suresh, S. Biomechanics and biophysics of cancer cells. *Acta Biomater.* **3,** 413–438 (2007).
15. Shoelson, B., Dimitriadis, E. K., Cai, H., Kachar, B. & Chadwick, R. S. Evidence and implications of inhomogeneity in tectorial membrane elasticity. *Biophys. J.* **87,** 2768–2777 (2004).
16. Dimitriadis, E. K., Horkay, F., Bechara, K. & Chadwick, R. S. Issues concerning the measurement of elastic properties at microscopic scales with the AFM. *Biophys. J.* **82,** 56A (2002).
17. Pugacheva, E. N., Jablonski, S. A., Hartman, T. R., Henske, E. P. & Golemis, E. A. HEF1-dependent Aurora A activation induces disassembly of the primary cilium. *Cell* **129,** 1351–1363 (2007).
18. Brown, H. G. & Hoh, J. H. Entropic exclusion by neurofilament sidearms: a mechanism for maintaining interfilament spacing. *Biochemistry* **36,** 15035–15040 (1997).
19. Cohen, M., Klein, E., Geiger, B. & Addadi, L. Organization and adhesive properties of the hyaluronan pericellular coat of chondrocytes and epithelial cells. *Biophys. J.* **85,** 1996–2005 (2003).
20. Jones, L. M., Gardner, M. J., Catterall, J. B. & Turner, G. A. Hyaluronic acid secreted by mesothelial cells: A natural barrier to ovarian cancer cell adhesion. *Clin. Exp. Metastasis* **13,** 373–380 (1995).
21. Toole, B. in *Cell Biology of the Extracellular Matrix* (ed. Hay, E.) 259–294 (Plenum Press, 1982).
22. Zimmerman, E., Geiger, B. & Addadi, L. Initial stages of cell-matrix adhesion can be mediated and modulated by cell-surface hyaluronan. *Biophys. J.* **82,** 1848–1857 (2002).
23. Zhang, L., Underhill, C. B. & Chen, L. Hyaluronan on the surface of tumor cells is correlated with metastatic behavior. *Cancer Res.* **55,** 428–433 (1995).
24. Israelachivili, J. in *Intermolecular and Surface Forces* 2nd edn (Academic Press, 1992).
25. Butt, H. J. *et al.* Steric forces measured with the atomic force microscope at various temperatures. *Langmuir* **15,** 2559–2565 (1999).
26. Emerson, R. J. T. & Camesano, T. A. Nanoscale investigation of pathogenic microbial adhesion to a biomaterial. *Appl. Environ. Microbiol.* **70,** 6012–6022 (2004).
27. Woodworth, C. D., Doniger, J. & Dipaolo, J. A. Immortalization of human foreskin keratinocytes by various human papillomavirus DNAs corresponds to their association with cervical carcinoma. *J. Virol.* **63,** 159–164 (1989).
28. Tsuprun, V. & Santi, P. Crystalline arrays of proteoglycan and collagen in the tectorial membrane. *Matrix Biol.* **15,** 31–38 (1996).
29. Lim, D. J. & Rueda, J. Distribution of glycoconjugates during cochlea development. A histochemical study. *Acta Otolaryngol.* **110,** 224–233 (1990).
30. Matzke, R., Jacobson, K. & Radmacher, M. Direct, high-resolution measurement of furrow stiffening during division of adherent cells. *Nature Cell Biol.* **3,** 607–610 (2001).

Acknowledgements

We gratefully acknowledge funding for this work from grants by the National Science Foundation no. 0304143 (I.S.), National Cancer Institute no. 1R15CA126855-01 (C.D.W.), and operational funds of Nanoengineering and Biotechnology Laboratories Center (NABLAB). Tissue was obtained from the Cooperative Human Tissue Network. We are thankful to S. Minko, V. Privman and E. Katz for useful discussions.

Author contributions

I.S. conceived and designed the experiments. S.I., R.M.G., V.S.R. and I.S. performed AFM and confocal measurements. C.D.W. and I.S. performed EM measurements. R.M.G. performed the critical electrolyte study. R.M.G., V.S.R. and I.S. analysed the data. S.I., C.D.W. and I.S. co-wrote the paper.

Additional information

Supplementary information accompanies this paper at www.nature.com/naturenanotechnology. Reprints and permission information is available online at http://npg.nature.com/reprintsandpermissions/. Correspondence and requests for materials should be addressed to I.S.